



**HAL**  
open science

# Experimental and numerical analysis of U-values of supply-air double windows

Yujian Huang

► **To cite this version:**

Yujian Huang. Experimental and numerical analysis of U-values of supply-air double windows. Construction durable. École Nationale des Travaux Publics de l'État [ENTPE], 2022. English. NNT : 2022ENTP0007 . tel-04412075

**HAL Id: tel-04412075**

**<https://theses.hal.science/tel-04412075>**

Submitted on 23 Jan 2024

**HAL** is a multi-disciplinary open access archive for the deposit and dissemination of scientific research documents, whether they are published or not. The documents may come from teaching and research institutions in France or abroad, or from public or private research centers.

L'archive ouverte pluridisciplinaire **HAL**, est destinée au dépôt et à la diffusion de documents scientifiques de niveau recherche, publiés ou non, émanant des établissements d'enseignement et de recherche français ou étrangers, des laboratoires publics ou privés.



Thesis National Number : 2022ENTP0007

**A THESIS OF ENTPE  
Member of the Université de Lyon**

**Doctoral school N° accreditation 162  
MEGA (Mécanique, Énergétique, Génie Civil, Acoustique)**

To obtain in the graduation of  
**PhD in Civil Engineering**

Defended on 13/12/2022 by:  
**Yujian HUANG**

---

**Experimental and Numerical Analysis of  
U-values of Supply-air Double Windows**

---

In front of the following examination committee:

Zhiqiang (John) ZHAI /Professor /University of Colorado Boulder

Committee chair

Liangzhu (Leon) WANG /Professor /Concordia University

Reviewer

Abdeslam DRAOUI /Professor /Abdelmalek Essaâdi University

Reviewer

Zhiqiang (John) ZHAI /Professor /University of Colorado Boulder

Examiner

Stéphanie GIROUX /Associate Professor /Claude Bernard University Lyon 1

Examiner

Richard CANTIN /ICTPE HDR /ENTPE

Co-supervisor

Mohamed EL MANKIBI /Research Director /ENTPE

Supervisor





Numéro national de thèse (NNT) : 2022ENTP0007

## **THÈSE DE DOCTORAT DE L'ENTPE Membre de l'Université de Lyon**

**École Doctorale N° accréditation 162  
MEGA (Mécanique, Énergétique, Génie Civil, Acoustique)**

**Spécialité / discipline de doctorat : Génie Civil**

Soutenue publiquement le 13/12/2022, par :  
**Yujian HUANG**

---

# **Analyse expérimentale et numérique des U-valeurs des double-fenêtres en mode insufflation**

---

Devant le jury composé de :

Zhiqiang (John) ZHAI, Professeur, Université du Colorado à Boulder

Président

Liangzhu (Leon) WANG, Professeur, Université Concordia

Rapporteur

Abdeslam DRAOUI, Professeur, Université Abdelmalek Essaadi

Rapporteur

Zhiqiang (John) ZHAI, Professeur, Université du Colorado à Boulder

Examineur

Stéphanie GIROUX, Maître de conférences HDR,

Université Claude Bernard Lyon 1

Examinatrice

Richard CANTIN, ICTPE HDR, ENTPE

Co-directeur de thèse

Mohamed EL MANKIBI, Directeur de Recherche, ENTPE-LTDS

Directeur de thèse

# **Experimental and Numerical Analysis of U-values of Supply-air Double Windows**

## **Abstract**

Windows area of French cities heritage buildings constitute a significant part of their facades. Thus, the improvement of window performance in heritage buildings has a large potential to achieve building energy efficiency goals. A challenge of window renovation in heritage buildings is that the façades of these buildings need to be preserved. To face this challenge, the supply-air double window is proposed as a renovation solution by putting a secondary window inside of the old window. During the window design, construction and renovation procedures, the U-value is an important indicator. Our research works are focus on the U-values of supply-air double windows, including proposing a new experimental method to identify the U-values, conducting a comprehensive parametric study on the U-values, determining a new method to calculate dynamic U-values and proposing an inverse identification framework. Specifically, an adjusted guarded hot box (GHB) experimental method was proposed by improving the GHB setup and calibration/testing process. During the GHB experiments, the U-values of different window configurations were tested and compared to reveal the application potentials of supply-air double windows. Furthermore, numerical simulations were performed based on a three-dimensional computational fluid dynamic (CFD) model which was validated by the GHB experimental data. Based on the simulations, a comprehensive parametric study was performed to better understand the variations in U-values and a sensitivity analysis was taken to compare the effects of different parameters on supply-air double windows. Furthermore, regression models which can support a fast decision-making under different boundary conditions were established and optimized based on data collected from CFD simulations. The optimized regression models were compared in terms of different evaluation indicators and also the effect of dataset size on model performance was investigated. Moreover, an inverse identification framework was proposed for renovated supply-air double windows. Such a framework could provide requirements for window renovation design parameter (e.g., the U-value of secondary window and supplied air flow rate) and thus facilitate the renovation work.

**Keywords:** *Supply-air Double Window; U-value; Guarded Hot Box (GHB) Method; Computational Fluid Dynamic (CFD) Simulation; Regression Model; Inverse Identification framework*

## **Acknowledgements**

Thanks firstly to Mohamed El Manbiki whose support and guidance contributed so substantially to the accomplishment of this dissertation, and who gave me opportunities to attend conferences held in Morocco, the Netherlands and Canada, and who always warmly invite me to coffee and tea; to Richard Cantin for giving me a lot of encouragements and giving me detailed feedback on the outcomes of my work; to Leon Wang and Abdeslam Draoui for reviewing my dissertation; to John Zhai and Stéphanie Giroux for taking part in my thesis jury; to the China Scholarship Council and the Région Auvergne-Rhône-Alpes for providing me financial supports; to Francette Pignard, Paul Martin de Beauce and Luc Delattre for their help and assistance; to Yaping Zhou for accompanying me in the last three years; to Mike Coillot who gave me a lot of help in my first year so that I can adapt to the school life as soon as possible; to Xin Gong and Tianrui Ouyang for bridging the communication gap between me and some French colleagues; to all the members in the team for sparing no effort in showing their friendliness; to my family, and particularly to my sister, for taking care of themselves and each other well; and to Min Tang who has the magical ability to make me happy.



# CONTENT

<b>ABSTRACT</b> .....	<b>2</b>
<b>ACKNOWLEDGEMENTS</b> .....	<b>4</b>
<b>LIST OF FIGURES</b> .....	<b>7</b>
<b>LIST OF TABLES</b> .....	<b>10</b>
<b>1 GENERAL INTRODUCTION</b> .....	<b>1</b>
<b>1.1 MOTIVATION, OVERVIEW &amp; CONTEXT</b> .....	<b>2</b>
<b>1.2 DEFINITION, CALCULATION AND IDENTIFICATION OF U-VALUE</b> .....	<b>5</b>
1.2.1 U-value definition and calculation .....	5
1.2.2 Identification methods .....	9
<b>1.3 SCIENTIFIC CHALLENGES, RESEARCH OBJECTIVES AND SCIENTIFIC APPROACHES</b> .....	<b>15</b>
1.3.1 Scientific challenges .....	15
1.3.2 Research objective and approaches .....	15
1.3.3 Dissertation Outline .....	17
<b>2 REVIEW OF TECHNOLOGIES AND PERFORMANCES OF MULTIPLE PANE WINDOWS</b> .....	<b>19</b>
<b>2.1 INTRODUCTION</b> .....	<b>20</b>
<b>2.2 APPLICATION TECHNOLOGIES</b> .....	<b>22</b>
2.2.1 Application of airflow — Ventilation windows .....	22
2.2.2 Application of flowing liquid — Liquid-flow windows .....	23
2.2.3 Application of aerogels — Aerogel Windows .....	25
2.2.4 Application of PCMs — PCM windows .....	26
<b>2.3 PERFORMANCE OF DIFFERENT APPLICATION TECHNOLOGIES</b> .....	<b>28</b>
2.3.1 Ventilation windows .....	28
2.3.2 Liquid-flow windows .....	30
2.3.3 Aerogel window .....	33
2.3.4 PCM Window .....	35
2.3.5 A comparison of different window technologies .....	38
<b>2.4 CONCLUSIONS</b> .....	<b>40</b>
<b>3 EXPERIMENTAL SETUP AND RESULTS</b> .....	<b>41</b>
<b>3.1 INTRODUCTION</b> .....	<b>42</b>
<b>3.2 EXPERIMENTAL SETUP DEVELOPMENT</b> .....	<b>44</b>
3.2.1 Guarded hot box .....	44
3.2.2 Conventional GHB method .....	49
3.2.3 Adjusted GHB method .....	54
3.2.4 Uncertainty Analysis .....	59
<b>3.3 EXPERIMENTAL RESULTS</b> .....	<b>60</b>
3.3.1 Calibration results .....	60
3.3.2 U-values of different window configurations .....	62
3.3.3 U-value with taking sample flanking loss into consideration .....	68
<b>3.4 CONCLUSIONS</b> .....	<b>71</b>

<b>4</b>	<b>PARAMETRIC AND SENSITIVITY ANALYSIS FOR SUPPLY–AIR DOUBLE WINDOWS BASED ON CFD SIMULATIONS</b>	<b>72</b>
<b>4.1</b>	<b>INTRODUCTION</b>	73
<b>4.2</b>	<b>CFD MODEL ESTABLISHMENT AND EVALUATION</b>	75
4.2.1	Model geometry and boundary conditions setup	75
4.2.2	Grid generation and grid independence analysis	78
4.2.3	CFD solver setup	80
4.2.4	Model selection and evaluation	80
<b>4.3</b>	<b>RESULTS</b>	83
4.3.1	Effects of window parameters	83
4.3.2	Effects of boundary conditions	91
4.3.3	Sensitivity analysis	96
<b>4.4</b>	<b>CONCLUSIONS</b>	99
<b>5</b>	<b>DETERMINATION, ANALYSIS AND ASSESSMENT OF A NEW DYNAMIC U-VALUE CALCULATION APPLIED TO SUPPLY–AIR DOUBLE WINDOWS</b>	<b>101</b>
<b>5.1</b>	<b>INTRODUCTION</b>	102
<b>5.2</b>	<b>METHODOLOGY</b>	103
5.2.1	Framework	103
5.2.2	Regression models	104
5.2.3	Model performance evaluation indicators	111
<b>5.3</b>	<b>MODEL TRAINING AND OPTIMIZATION</b>	113
5.3.1	Sensitivity analysis on the train/test splitting ratio	113
5.3.2	Hyper-parameter optimization	115
<b>5.4</b>	<b>RESULTS</b>	121
5.4.1	Comparison of different regression models	121
5.4.2	Effect of dataset size	125
<b>5.5</b>	<b>CONCLUSIONS</b>	127
<b>6</b>	<b>INVERSE IDENTIFICATION FRAMEWORK FOR RENOVATED SUPPLY–AIR DOUBLE WINDOWS — A CASE STUDY</b>	<b>128</b>
<b>6.1</b>	<b>INTRODUCTION</b>	129
<b>6.2</b>	<b>INVERSE IDENTIFICATION FRAMEWORK</b>	130
6.2.1	PSO algorithm	132
<b>6.3</b>	<b>CASE STUDY</b>	134
6.3.1	Description of the case study	134
6.3.2	Results and discussions	134
<b>6.4</b>	<b>CONCLUSIONS</b>	137
<b>7</b>	<b>GENERAL CONCLUSIONS</b>	<b>138</b>
<b>7.1</b>	<b>CONCLUSIONS</b>	139
<b>7.2</b>	<b>OUTLOOK AND PERSPECTIVE</b>	142
	<b>REFERENCE</b>	<b>143</b>

## List of Figures

Figure 1-1 (a) Total final consumption by sector from 1990 to 2019; (b) Energy consumption in 2019, available at <a href="http://www.iea.org/statistics">www.iea.org/statistics</a>	2
Figure 1-2 (a) CO <sub>2</sub> emissions by sector from 1990 to 2019; (b) CO <sub>2</sub> emissions in 2019, available at <a href="http://www.iea.org/statistics">www.iea.org/statistics</a>	3
Figure 1-3 Picture of Haussmann-style buildings, <a href="https://www.telerama.fr/scenes/haussmann-eventreur-ou-inventeur-de-paris,153998.php">https://www.telerama.fr/scenes/haussmann-eventreur-ou-inventeur-de-paris,153998.php</a>	4
Figure 1-4 Diagram of heat exchanges for a conventional window (in winter)	5
Figure 1-5 Diagram of heat exchanges for a supply-air double window (in winter)	8
Figure 1-6 Laboratory methods: (a) GHP method, (b) HFM method, (c) GHB method [23], (d) CHB method [23]	10
Figure 1-7 Heat transfer modes	11
Figure 1-8 Schematic of simplified models	12
Figure 1-9 Scientific approaches	17
Figure 2-1 Schematic illustrations of double-pane, triple-pane and quadruple-pane windows and double windows	21
Figure 2-2 Ventilation modes: (a) supply mode; (b) exhaust mode; (c) indoor circulation mode; (d) outdoor circulation mode; (e) dual airflow mode; (f) indoor circulation mode in winter and outdoor circulation mode in summer	23
Figure 2-3 Fluid circulation: (a) closed-loop circulation; (b) closed-loop circulation with submerged heat exchanger; (c) open-loop circulation	24
Figure 2-4 Configurations of liquid-flow windows	24
Figure 2-5 Configurations of PCM glazing	27
Figure 2-6 Energy saving potential of airflow [66,70], flowing liquid [38,43–45], aerogels [51,87,91,93,109] and PCMs [96] in different climates	38
Figure 3-1 Guarded hot box in ENTPE	45
Figure 3-2 Schematic of the guarded hot box	46
Figure 3-3 Data acquisition and control system	46
Figure 3-4 Interface of PID controllers	48
Figure 3-5 Air temperature profiles during a calibration test	48
Figure 3-6 Schematic of step 1	50
Figure 3-7 Schematic of step 2	51
Figure 3-8 Locations of Sensors in the calibration test	52
Figure 3-9 Picture of the calibration test	52
Figure 3-10 Picture and schematic of tested windows	54
Figure 3-11 Schematic of the adjusted GHB	55
Figure 3-12 Positions of sensors	56
Figure 3-13 Picture of the single-glazed window with a tube	57
Figure 3-14 Configurations of closed-air double windows and supply-air double windows	58
Figure 3-15 Picture of testing a closed-air double window and a supply-air double window	58
Figure 3-16 Calibrated heat losses under different air temperature difference and air velocities	60
Figure 3-17 Tube heat losses under different tube inlet air temperatures and velocities	61

Figure 3-18 Convective heat transfer coefficients in hot and cold sides	62
Figure 3-19 U-values of the single-glazed window, clear double-glazed window and Low-E double-glazed window	64
Figure 3-20 U-values of closed-air double windows with a 95 mm gap width	65
Figure 3-21 U-values of closed-air double windows with different gap widths	66
Figure 3-22 U-values of supply-air double windows with a 95 mm gap width	67
Figure 3-23 U-values of the VW3 with different inlet air velocities	68
Figure 3-24 U-values with taking the sample flanking loss into consideration	70
Figure 4-1 Simulation steps and ANSYS components	75
Figure 4-2 Model geometry	76
Figure 4-3 Schematic of grid generation	79
Figure 4-4 Temperature distribution along the mid-line of the airflow channel	80
Figure 4-5 Comparison on temperatures between experiment results and simulation results	82
Figure 4-6 Correlations between the window area and U-values	84
Figure 4-7 Correlations between the thermal conductivity of external window frame and U-values	85
Figure 4-8 Correlations between the thermal conductivity of internal window frame and U-values	86
Figure 4-9 Correlations between the air mass flow rate and U-values	88
Figure 4-10 Influence of the position of Low-E coating on the U-values	89
Figure 4-11 Correlations between the glazing surface emissivity and U-values	90
Figure 4-12 Correlations between the inside convective heat transfer coefficient and U-values	92
Figure 4-13 Correlation between the outside convective heat transfer coefficient and U-values	93
Figure 4-14 Correlations between the air temperature difference and U-values in Case #1	94
Figure 4-15 Correlations between the air temperature difference and U-values in Case #2	96
Figure 5-1 Schematic of framework	104
Figure 5-2 Schematic of the support vector regression	107
Figure 5-3 Schematic of the random forest regression	108
Figure 5-4 Schematic of the GBR model	110
Figure 5-5 Correlation between the train/test splitting ratio and average MAE value for the dataset D1, D2 and D3	114
Figure 5-6 Boxplots of MAE values for different train/test splitting ratios	115
Figure 5-7 Schematic of k-fold cross validation	116
Figure 5-8 MAE values with different number of neighbors	116
Figure 5-9 Correlations between the number of estimators and MAE values	119
Figure 5-10 Correlations between the maximum depth of estimators and MAE values	119
Figure 5-11 Scatter plots of the calculated U-values	123
Figure 5-12 Boxplots of error residuals produced by different models	124
Figure 5-13 Effect of dataset sizes on model performance	126
Figure 6-1 Flowchart of the inverse identification process	130
Figure 6-2 Flowchart of the inverse identification process with considering uncertainties	131
Figure 6-3 Flowchart of PSO algorithm	133

Figure 6-4 Correlation between the sampling size and inverse identification result	135
Figure 6-5 Impact of the uncertainty magnitude on the inverse identification result	136

## List of Tables

Table 1-1 Inside and outside convective heat transfer coefficients	7
Table 1-2 Information of CFD models	13
Table 2-1 Control systems and strategies of inlet water temperature	25
Table 2-2 Comparison of different application technologies	27
Table 3-1 Information of sensors	47
Table 3-2 Detailed testing reports of the single-glazed window, clear double-glazed window and Low-E double-glazed window	62
Table 3-3 Detailed testing reports of the DW1, DW2 and DW3	64
Table 3-4 Detailed testing reports of the VW1, VW2 and VW3	66
Table 3-5 Detailed testing reports by taking the sample flanking loss into consideration	69
Table 4-1 Physical properties of glass and frame	76
Table 4-2 Boundary conditions	76
Table 4-3 Window configuration parameters and boundary conditional parameters	77
Table 4-4 Comparison of tested U-values and simulated U-value	82
Table 4-5 Sensitivity analysis results of the VW1	97
Table 4-6 Sensitivity analysis results of the VW2	97
Table 4-7 Sensitivity analysis results of the VW3	98
Table 5-1 MAE of the dataset D1	117
Table 5-2 MAE of the dataset D2	117
Table 5-3 MAE of the dataset D3	118
Table 5-4 Optimized hyper-parameters of the RFR, ETR, GBR and XGBR models	119
Table 5-5 Model performance in terms of MAE, RMSE, NMAE, NRMSE and R <sup>2</sup>	124
Table 6-1 Constraints of air flow rate	136
Table 7-1 Correlations between the studied parameters and U-values	140

# **1 General Introduction**

## 1.1 Motivation, overview & Context

The report issued by the Intergovernmental Panel on Climate Change (IPCC) shows that global temperature has exceeded more than 1°C of warming since the pre-industrial era [1]. The global warming increases climate hazards. To avoid this, the Paris Agreement establishes a global framework to hold global warming below 2°C [2]. A necessary action is to reduce greenhouse gas (GHG) emissions.

The French energy transition law aims to reduce greenhouse gas emissions by 40% by 2030 and 75% by 2050 (compared to 1990), and reduce final energy consumption by 20% by 2030 and 50% by 2050 (compared to 2012) [3]. As presented in Figure 1-1 and Figure 1-2, the residential sector is the second most important sector responsible for energy consumption and CO<sub>2</sub> emissions after the transport sector. To reduce energy consumption of new buildings, the building regulations have set standards to ensure buildings to meet minimum performance requirements. However, in France new buildings are not the main part of building stocks. Indeed, as reported in [4], 66% of buildings are built before 1974. To achieve energy transition objectives, the building renovation attracts more and more attentions. The Energy Renovation Plan for Buildings [5] aims to renovate all of the old buildings to low energy buildings whose primary energy consumption is equal to or less than 80 kWh/(m<sup>2</sup> year) by 2050.

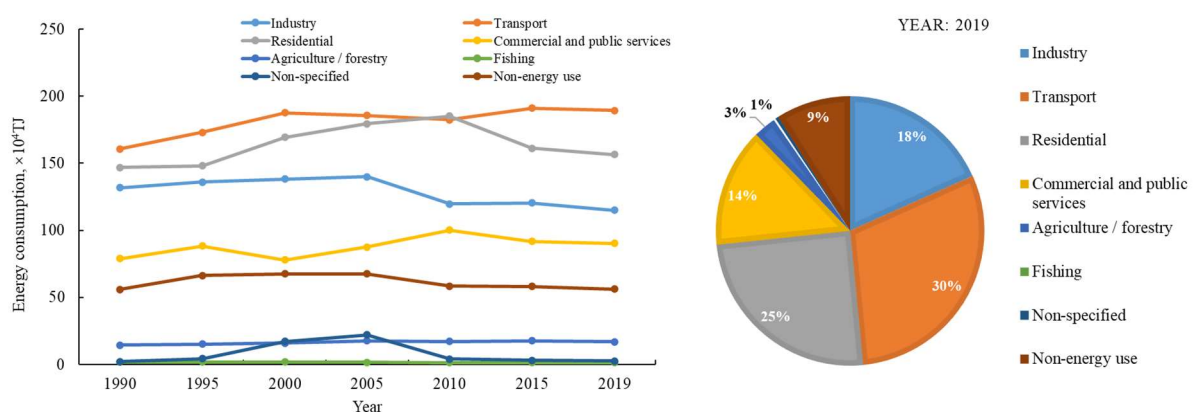


Figure 1-1 (a) Total final consumption by sector from 1990 to 2019; (b) Energy consumption in 2019, available at [www.iea.org/statistics](http://www.iea.org/statistics)



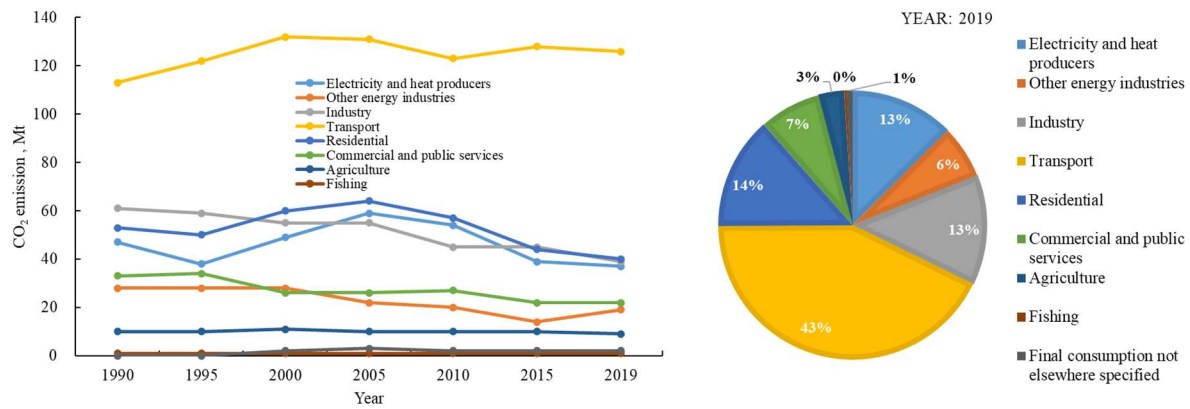


Figure 1-2 (a) CO<sub>2</sub> emissions by sector from 1990 to 2019; (b) CO<sub>2</sub> emissions in 2019, available at [www.iea.org/statistics](http://www.iea.org/statistics)

Among building envelopes (i.e., walls, roofs, floors and windows), the window is mainly responsible for building heat losses. For example, for a two-story building, the window area constitutes 30% of walls, and the energy losses through windows contribute to 60% of the total energy losses through the envelope [6]. In past decades, advanced coatings (e.g., thermochromic coating) which can be attached on the glass have been developed to adjust glass optical performance to meet different requirements [7]. And to improve window thermal performance, an effective technology that attracts increasing attentions is applying multi-pane windows. A review of multi-pane windows is presented in the next chapter. Also, a number of innovative designs for window frames have arisen [6].

Although a number of advanced window technologies have been developed, some of them cannot be applied for old buildings where the building appearances must be maintained [8]. The supply-air double window attracts our attentions owing to its multiple benefits. First, it can be an appropriate renovation solution for heritage buildings by adding an additional window inside of the old window, without damaging the building structure and appearance. Second, it can provide fresh air to improve indoor air quality. Third, it can preheat fresh air before air enters into the room and thus reduce the ventilation heating load. Fourth, using it do not affect the view to the outside. In fact, windows area of French cities heritage buildings also called Haussmann (as shown in Figure 1-3) constitute a high percent of their facades (more than 65 %).

Thus, an improvement of window performance will highly contribute to the improvement of global building performance.



*Figure 1-3 Picture of Haussmann-style buildings, <https://www.telarama.fr/scenes/hausmann-eventreur-ou-inventeur-de-paris,153998.php>*

## 1.2 Definition, calculation and identification of U-value

The U-value is an important indicator to characterize window thermal performance. It is often used in building simulation tools such as EnergyPlus to simulate energy performances. Moreover, accurate identification of U-value can support decision-making during buildings design and refurbishment processes. The conventional U-value is defined as the amount of heat losses through windows per  $m^2$  under one temperature degree difference between indoor and outdoor environments without taking solar radiation into account. It can reflect the thermal insulation performance of windows. A lower  $U$ -value indicates a higher insulation performance and it should be as low as possible. However, the conventional U-value cannot reflect the ability of a supply-air double window to recover part of heat losses from the interior window. To address this problem, the equivalent  $U$ -value ( $U_{eq}$  value) was firstly proposed by [9]. In this section, the definition, calculation and identification of U-value are introduced and analyzed.

### 1.2.1 U-value definition and calculation

#### (1) Standard U-value

Figure 1-4 represents the diagram of heat exchanges occurring in a conventional window. The heat exchange between the inside environment and interior window surface ( $Q_{int}$ ) is equal to that between the outside environment and exterior window surface ( $Q_{ext}$ ) under steady conditions.

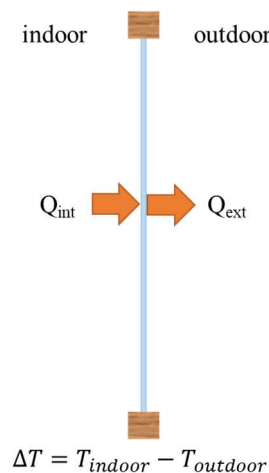


Figure 1-4 Diagram of heat exchanges for a conventional window (in winter)

The U-value can be calculated as:

$$U = \frac{Q_{int}}{A\Delta T} = \frac{Q_{ext}}{A\Delta T} \quad (1-1)$$

Where,  $\Delta T$  is the difference between indoor and outdoor air temperatures, °C;  $A$  is the window total area, m<sup>2</sup>.

As stated in the ISO 15099 [10], the U-value of a single-glazed window can be calculated as:

$$U = \frac{A_g U_g + A_f U_f + l_\psi \psi}{A} \quad (1-2)$$

Where,  $U_g$  is the U-value of glazing part, W/(m<sup>2</sup> K);  $U_f$  is the U-value of frame part, W/(m<sup>2</sup> K);  $\psi$  is a linear thermal transmittance that accounts for the interaction between glazing part and frame part, W/(m K);  $A_g$  is the area of glazing part, m<sup>2</sup>;  $A_f$  is the area of frame part, m<sup>2</sup>;  $l_\psi$  is the perimeter of glazing part, m.

For multi-glazed windows (including double-glazed windows and double windows), their U-values can be expressed as the reciprocal of the sum of the thermal resistance ( $R$ ),

$$U = \frac{1}{R} = \frac{1}{R_{s,ext} + R_{air,i} + R_{g,i} + R_{s,int}} \quad (1-3)$$

$$R_s = \frac{1}{h_r + h_c} \quad (1-4)$$

Where,  $R_{air}$  is the thermal resistance of  $i$ th air layer, (m<sup>2</sup> K)/W;  $R_g$  is the thermal resistance of  $i$ th glazing layer, (m<sup>2</sup> K)/W;  $R_s$  is the thermal resistance of exterior/interior surfaces, (m<sup>2</sup> K)/W;  $h_r$  is the external/internal radiative heat transfer coefficient, W/(m<sup>2</sup> K);  $h_c$  is the external/internal convective heat transfer coefficient, W/(m<sup>2</sup> K).

The radiative heat transfer coefficients are simply calculated as:

$$h_r = \frac{\varepsilon_s \sigma (T_s^4 - T_r^4)}{T_s - T_r} \quad (1-5)$$

Where,  $\varepsilon_s$  is the emissivity of glazing surface;  $T_s$  is the window surface temperature, °C;  $T_r$  is the radiation temperature, °C.

For the convective heat transfer coefficient, different values and correlations have been presented in standards and literatures, as shown in Table 1-1.

*Table 1-1 Inside and outside convective heat transfer coefficients*

Ref.	Window configuration	Inside convective heat transfer coefficient [W/(m <sup>2</sup> K)]	Outside convective heat transfer coefficient [W/(m <sup>2</sup> K)]
			$h_{c,ext} = 4.7 + 7.6v_s$
[11]	Supply-air double window	-	$v_s = \begin{cases} 0.25v, & v > 2m/s \\ 0.5, & v \leq 2m/s \end{cases}$ , if the surface is windward $v_s = 0.3 + 0.05v$ , if the surface is leeward
[12]	Double-glazed exhaust-air window	$h_{c,int} = 5.34 + 3.22v$	$h_{c,ext} = 5.62 + 3.9v$
[13]	Triple-glazed supply-air window	3.6	$h_{c,ext} = 5.15v^{0.81}$ ( $v$ is the wind speed at 10 meters high)
[14]	Ventilation window	8	23
[15]	Supply-air double window	7.7	25
[10]	-	3.6	20

## (2) U-values of supply-air double window

Figure 1-5 represents the diagram of heat exchanges occurring in a supply-air double window. As shown in Figure 1-5, the heat lost through the interior window is partly recovered by the supplied air. Thus, the heat loss from the interior window is larger than the heat loss from the exterior window.

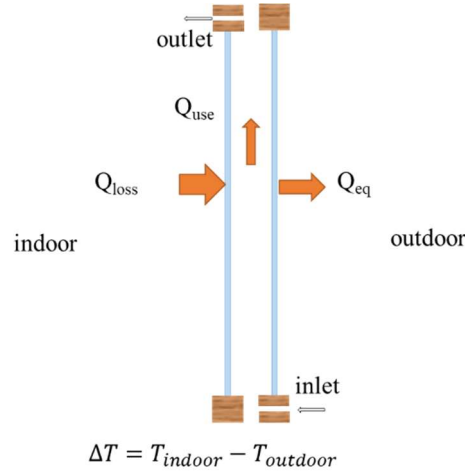


Figure 1-5 Diagram of heat exchanges for a supply-air double window (in winter)

To consider the recovered heat in the U-value, the  $U_{loss}$  value,  $U_{use}$  value and  $U_{eq}$  value were presented and defined [15]. The  $U_{loss}$  value represents the heat flux transferred through interior window per  $m^2$  under one degree of air temperature difference between the indoor and outdoor environments:

$$U_{loss} = \frac{Q_{loss}}{A\Delta T} \quad (1-6)$$

Where,  $\Delta T$  is the difference between indoor and outdoor air temperatures, °C.

The proposed  $U_{use}$  value represents the capability of supply-air double windows to recover the heat loss through interior window per  $m^2$ . It is calculated as Eq. (1-7):

$$U_{use} = \frac{Q_{use}}{A\Delta T} \quad (1-7)$$

$$Q_{use} = \dot{m}C(T_{ol} - T_{il}) \quad (1-8)$$

Where  $C$  is the specific heat capacity of air (J/kg °C),  $\dot{m}$  is the air mass flow rate (kg/s),  $T_{ol}$  is the window outlet air temperature (°C) and  $T_{il}$  is the window inlet air temperature (°C).

Also,  $Q_{use}$  can be expressed as Eq. (1-9):

$$Q_{use} = Ah_{ch1}\Delta T_1 - Ah_{ch2}\Delta T_2 \quad (1-9)$$

Where,  $h_{ch}$  represents the convective heat transfer coefficient in the ventilated airflow channel,  $W/(m^2 K)$ ;  $\Delta T_1$  and  $\Delta T_2$  are the temperature difference between channel's surfaces and airflow, °C.

The  $U_{eq}$  value represents the heat flux transferred through the exterior window per  $m^2$  under one degree of air temperature difference between the indoor and outdoor conditions (expressed as Eq. (1-10)). It can be calculated by the  $U_{loss}$  value and  $U_{use}$  value.

$$U_{eq} = \frac{Q_{eq}}{A\Delta T} \quad (1-10)$$

$$U_{eq} = U_{loss} - U_{use} \quad (1-11)$$

### 1.2.2 Identification methods

#### (1) Measurement methods

The guarded hot plate (GHP) method, heat flow meter (HFM) method and hot box (HB) method are three standard U-value measurement methods [16–22].

As shown in Figure 1-6(a), the GHP apparatus is composed of two cooling units and a heating unit surrounded by guarded sections. Specimens are placed between the cooling and heating units. In the GHP method, the power supplied to the heating unit is measured to determine the heat flow through the specimen. The HFM apparatus (as shown in Figure 1-6(b)) is similar to the GHP apparatus. In the HFM method, the heat flow densities are measured by heat flux meters placed on the surface of the specimen. The HB method includes the guarded hot box (GHB) method and the calibrated hot box (CHB) method. As illustrated in Figure 1-6(c), the CHB apparatus is composed of a metering box and a cold box. During the measurement, the laboratory temperature needs to be controlled to calibrate the flanking loss of the metering box. The specimen is placed between the metering box and the cold box. As shown in Figure 1-6(d), the GHB apparatus is composed of a guarding box, a metering box and a cold box. Due to the guarding box, the laboratory temperature does not need to be controlled. In the CHB and

GHB methods, the heat flow through the sample is determined by the energy supplied to the metering box, the calibrated metering box losses and flanking losses.

Among the above methods, the GHP method and HFM method are suited for glass units with homogeneous structures. While for full-scale windows with inhomogeneous structures, the HB method is recommended.

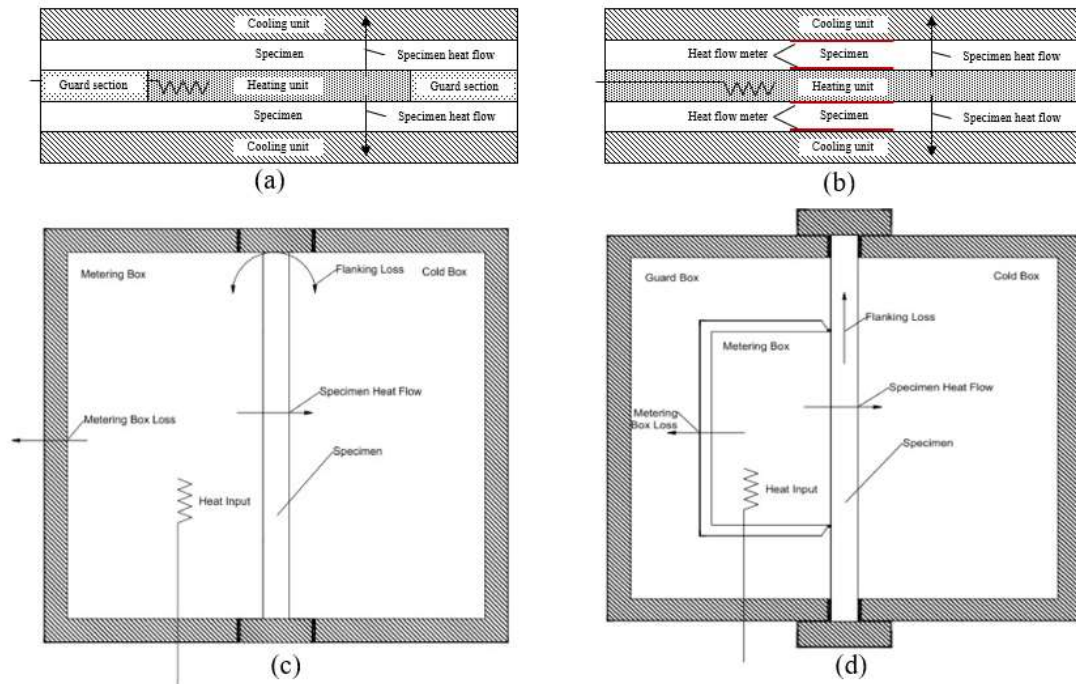


Figure 1-6 Laboratory methods: (a) GHP method, (b) HFM method, (c) GHB method [23], (d) CHB method [23]

## (2) Numerical simulations

In numerical simulations, the conduction, convection and radiation (as shown in Figure 1-7) need to be considered and coupled. Specifically, the conduction is present in the glazing part and frame part. The convection is occurred between indoor/outdoor air and window and between the supplied air and window. The radiation exists between the indoor/outdoor environment and interior/exterior face of window as well as between window surfaces.



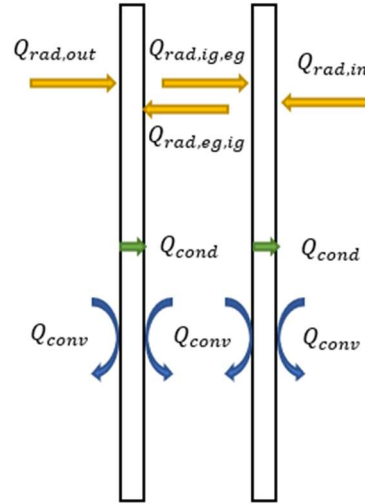


Figure 1-7 Heat transfer modes

The airflow between two windows adds difficulties in replicating the heat transfer process through numerical simulations. According to the complexity of treatments on the fluid problem, the numerical models could be categorized into simplified models and CFD models.

In the simplified model, the fluid between two glass panes is modeled based on either zero-dimension (as shown in Figure 1-8(a)) or one-dimension assumption (as shown in Figure 1-8(b)). For the zero-dimension assumption, the fluid is assumed uniform and for the one-dimension assumption, the fluid is divided into several sections along with the height.

The heat transfer between airflow and glass panes is calculated based on the convective heat transfer coefficient which is determined by empirical correlations. The energy balance equation for the simplified model can be written as Eq. (1-12).

$$\rho cV \frac{\partial T_{2,i}}{\partial \tau} = A_i h_{ch,12} (T_{1,i} - T_{2,i}) + A_i h_{ch,23} (T_{3,i} - T_{2,i}) + c\dot{m} (T_{2,i} - T_{2,i-1}) \quad (1-12)$$

Where,  $A_i$  is the area of glass surface  $i$ ,  $m^2$ ;  $V$  is the volume,  $m^3$ .

The empirical correlation of convective heat transfer given in standard ISO 15099 [10] is:

$$h_{ch,12} = h_{ch,23} = 2h_{c0} + 4v_{ch} \quad (1-13)$$

Where,  $h_{c0}$  is the convective heat coefficient in a non-ventilated air channel, W/(m<sup>2</sup> K);  $v_{ch}$  is the average air velocity in the channel, m/s.

$$h_{c0} = Nu \frac{\lambda}{d} \quad (1-14)$$

Where,  $Nu$  is the Nusselt number;  $\lambda$  is the air thermal conductivity, W/(m K);  $d$  is the gap width between channel surfaces, m.

$$Nu = [Nu_1, Nu_2]_{max} \quad (1-15)$$

$$Nu_1 = \begin{cases} 0.0673838Ra^{1/3}, & 5 \times 10^4 < Ra \\ 0.028154Ra^{0.4134}, & 10^4 < Ra \leq 5 \times 10^4 \\ 1 + 1.7596678 \times 10^{-10}Ra^{2.2984755}, & Ra \leq 10^4 \end{cases} \quad (1-16)$$

$$Nu_2 = 0.242 \left[ \frac{Ra}{H/d} \right]^{0.272} \quad (1-17)$$

$$Ra = \frac{\rho^2 d^3 g \beta C \Delta T}{\mu \lambda} \quad (1-18)$$

Where,  $Ra$  is the Rayleigh number;  $H$  is the height of the airflow channel, m;  $\rho$  is the air density, kg/m<sup>3</sup>;  $g$  is the gravity acceleration, m/s<sup>2</sup>;  $\beta$  is the thermal expansion coefficient of air, 1/K;  $\Delta T$  is the temperature difference between the left and right internal surfaces that face the airflow channel, °C;  $\mu$  is the air viscosity, kg/(m s).

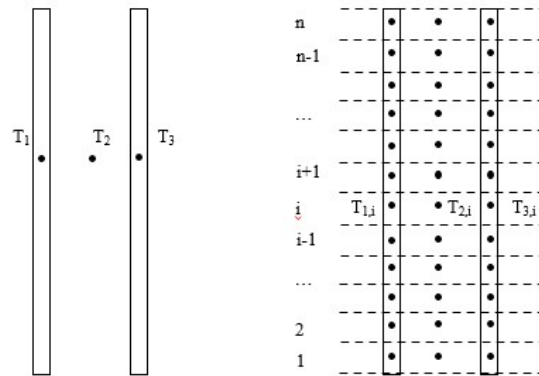


Figure 1-8 Schematic of simplified models

The simplified model could be solved by finite difference method and its computational cost per iteration is low. Such a method is suitable for long-term simulations and adapted in

building energy simulation tools (e.g., EnergyPlus). However, estimation errors may occur if the empirical correlation is not precisely fit for the studied phenomenon.

In the CFD model, the fluid medium is modeled based on two- or three-dimensional assumptions by meshing the fluid region into finite number of control volumes [24,25]. Compared to the simplified model, the CFD model could provide more accurate results. The information of CFD models established for ventilation window are summarized in Table 1-2.

*Table 1-2 Information of CFD models*

Reference	Structure	Dimension	Viscous model	Radiation model
Raffnsøe [26]	Air flow window	2D	RNG k-ε model	DTRM
Bhamjee [25]	Supply-air double window	2D	SST k-ω model, enhanced wall treatment	\
Gosselin [24]	Dual-airflow window	3D	RNG k-ε model	DO model
Southall, McEvoy [27]	Supply-air double window	2D	k-ε model	\
Gloriant [28]	Triple-glazed supply-air window	2D	Not mentioned	DO model

For each controlled volume, mass balance equation, momentum conservation equation and energy balance equation are established to get detailed temperature and velocity fields. The equations for the fluid medium are as Eq. (1-19)-(1-23) [29].

Mass conservation equation:

$$\frac{\partial u}{\partial x} + \frac{\partial v}{\partial y} + \frac{\partial w}{\partial z} = 0 \quad (1-19)$$

Momentum conservation equation:

$$\rho \left( u \frac{\partial u}{\partial x} + v \frac{\partial u}{\partial y} + w \frac{\partial u}{\partial z} \right) = -\frac{\partial p}{\partial x} + \mu \left( \frac{\partial^2 u}{\partial x^2} + \frac{\partial^2 u}{\partial y^2} + \frac{\partial^2 u}{\partial z^2} \right) \quad (1-20)$$

$$\rho \left( u \frac{\partial v}{\partial x} + v \frac{\partial v}{\partial y} + w \frac{\partial v}{\partial z} \right) = -\frac{\partial p}{\partial y} + \mu \left( \frac{\partial^2 v}{\partial x^2} + \frac{\partial^2 v}{\partial y^2} + \frac{\partial^2 v}{\partial z^2} \right) \quad (1-21)$$

$$\begin{aligned} \rho \left( u \frac{\partial w}{\partial x} + v \frac{\partial w}{\partial y} + w \frac{\partial w}{\partial z} \right) \\ = -\frac{\partial p}{\partial z} + \mu \left( \frac{\partial^2 w}{\partial x^2} + \frac{\partial^2 w}{\partial y^2} + \frac{\partial^2 w}{\partial z^2} \right) + \rho g \beta (T - T_c) \end{aligned} \quad (1-22)$$

Energy conservation equation:

$$\rho c_p \left( u \frac{\partial T}{\partial x} + v \frac{\partial T}{\partial y} + w \frac{\partial T}{\partial z} \right) = k \left( \frac{\partial^2 T}{\partial x^2} + \frac{\partial^2 T}{\partial y^2} + \frac{\partial^2 T}{\partial z^2} \right) + S \quad (1-23)$$

Where,  $u$ ,  $v$  and  $w$  indicate the velocity, m/s;  $\mu$  is the dynamic viscosity of air, kg/(m s);  $g$  is the gravitational acceleration, m/s<sup>2</sup>;  $T$  is temperature, °C;  $\beta$  is the thermal expansion coefficient, 1/K;  $S$  is the energy source, W;  $k$  is the thermal conductivity, W/(m K).

### **1.3 Scientific challenges, research objectives and scientific approaches**

#### **1.3.1 Scientific challenges**

U-value is the mean and an important indicator in characterizing window thermal performance and analyzing building energy consumption. Although several studies have been proposed for the U-values of supply-air double windows [29], a further exploration is still required to address the following issues:

(1) The GHB method is suggested for testing U-values of windows, but as stated in ISO 8990 [17] “the standard method does not provide for measurements where there is mass transfer through the specimen during the test”, an adapted GHB method is still lacked to test supply-air double windows.

(2) Although some parametric analyses have been performed for U-values of supply-air windows, there is no sensitivity analysis to compare the effects of different parameters on the U-values.

(3) The U-values of supply-air double windows are varying with the boundary conditions, and thus a single U-value cannot well reflect window thermal performance and support decision-makings under different conditions.

(4) To achieve energy goals, the requirements for window performance (i.e., minimum requirement of U-value) have been proposed. Such requirements can help users to fast choose a new window since the U-value of a new constructed window is often given by manufactures. While for a renovated supply-air double window, the U-value of renovated window is not given. To meet the requirement of minimum U-value, requirements for renovation design parameters which is straightforward for users to quickly determine possible renovation solutions are required.

#### **1.3.2 Research objective and approaches**

According to the scientific challenges, the research objectives are:

(1) Propose an adjusted and improved GHB method.

(2) Perform a comprehensive parametric study to help understand the variations in the U-values of supply-air double windows with mechanical ventilation.

(3) Determine a new method with high computational efficiency to calculate dynamic U-values for supply-air double windows under different boundary conditions (i.e., air temperatures and convective heat transfer coefficients).

(4) Propose an inverse identification method to address the above-mentioned issue (4). The basic idea of inverse identification is to inversely determine the unknown requirements of renovation design parameters (i.e., air flow rate) by continuously reducing the difference between the performance of renovated supply-air double window and the window performance requirements.

In order to accomplish these objectives, scientific methods (as shown in Figure 1-9) including experiments, numerical models and mathematical models are applied.

(1) Experiment

- Conventional guarded hot box
- Improved guarded hot box

(2) Numerical model

- Three-dimensional CFD model

(3) Mathematical model

- Regression models (multiple linear regression, K-nearest neighbor regression, support vector regression, random forest regression, extra tree regression, gradient boosting regression, extreme gradient boosting regression)
- Particle swarm optimization algorithm

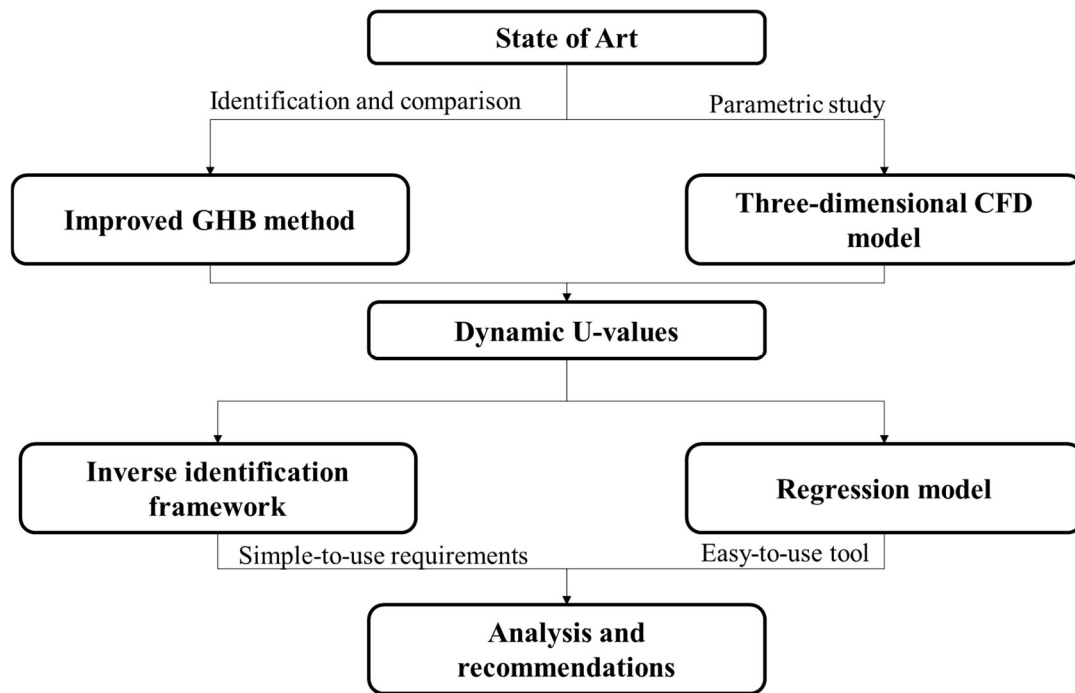


*Figure 1-9 Scientific approaches*

### 1.3.3 Dissertation Outline

The dissertation is composed of seven chapters. The first chapter presents the context and the definition, calculation and identification of window U-values.

The second chapter presents a review of technologies and performance of multiple pane windows. Also, the performances of different technologies are compared.

The third chapter presents the experimental setup and results. In this chapter, an adjusted guarded hot box (GHB) method is proposed. Based on the conventional and adjusted GHB methods, the U-values of a single-glazed window, a double-glazed window, a Low-E double-glazed window, three closed-air double windows and three supply-air double windows are measured and compared.

The fourth chapter presents the numerical model and simulation results. In this chapter, a three-dimensional CFD model is established and it is validated by the GHB experimental data. Based on the validated model, a comprehensive parametric study is performed to compare effects of different window configuration parameters and boundary conditional parameters on the U-values of supply-air double windows.

The fifth chapter analyzes and compares the performance of different regression methods to determine dynamic U-values of a supply-air double window. The regression models are trained and optimized based on the dataset collected from CFD simulations. Also, the impact of dataset size on model performance is discussed.

The sixth chapter proposes an inverse identification framework for renovated supply-air double window to provide requirements for renovation design parameters. In this chapter, a case study is performed with and without considering uncertainties of boundary conditions. Based on the case study, the requirement for air flow rate under deterministic scenarios and uncertain scenarios are compared and discussed.

Finally, the seventh chapter presents the conclusions and further work on the subject.



## **2 Review of Technologies and Performances of Multiple Pane Windows**

## 2.1 Introduction

Over the last years, different window technologies are proposed to improve window performance. The multiple pane window (including double-glazed windows and double windows, as shown in Figure 2-1) is the most popular to replace the conventional single pane window. As reported in [30], by replacing a single-glazed window with a double-glazed window, 72.6% energy could be saved in a warm region of Mexico. In a study conducted by Somasundaram et al., a low-e double glazing was installed inside of a clear glass facing three orientations (SE, SW, NW) [31]. They concluded that 9% saving of the daily energy consumption of air conditioning was achieved. Aydın performed numerical simulations based on different climatic zones of Turkey to determine the optimum air layer thickness [32]. The results showed that the optimum air layer thickness was 18-20 mm for Antalya, 15-18 mm for Trabzon and 12-15 mm for Kars. In multiple pane windows, the space between two glass panes is often filled with air or inert gas (e.g., argon, krypton and xenon) which can be treated as an additional component. This opens possibilities to apply airflow, flowing liquid, aerogel and PCM as advanced inter-pane medium to further improve window thermal and energy performances. In the development of application technologies, different types of liquids and promising materials (including aerogels and PCMs), different operation modes of airflow and flowing liquid, and different window structures have been proposed. And the performances of the proposed technologies as well as the influential factors have been widely investigated in studies. To better apply these technologies and help users select appropriate technologies, a comprehensive review including the existing application technologies and performance of different technologies is proposed in this Chapter.

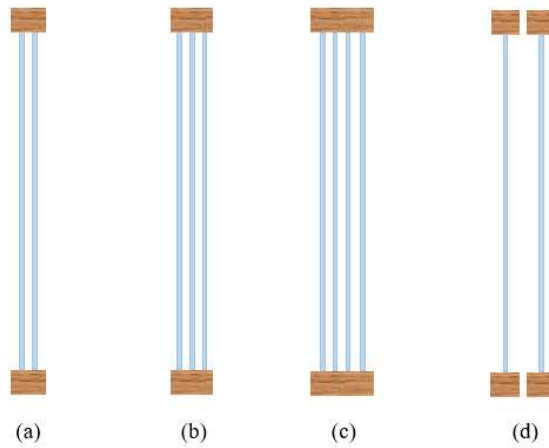


*Figure 2-1 Schematic illustrations of double-pane, triple-pane and quadruple-pane windows and double windows*

The chapter is structured into four sections: Section 2.1 is the introduction. Section 2.2 summarizes the application technologies of each advanced inter-pane medium as well as advantages and limitations of each medium in applications. Section 2.3 reviews comparative studies and parametric studies carried out for investigating performance of different application technologies and compares energy saving potentials of different inter-pane mediums under different climates. Section 2.4 concludes this chapter.

## 2.2 Application Technologies

In this section, application technologies of different advanced inter-pane mediums (i.e., airflow, flowing liquid, aerogel and PCM) are summarized. Also, advantages and disadvantages of each inter-pane medium in real applications are summarized and compared

### 2.2.1 Application of airflow —Ventilation windows

In ventilation windows, the air flowing through the cavity between two glass panes could be driven by either natural or mechanical forces. As illustrated in Figure 2-2, the ventilation mode can be designed as the supply mode, exhaust mode, indoor circulation mode, outdoor circulation mode and dual airflow mode [11,33]. In the supply mode, outdoor fresh air is provided and it is preheated by the solar radiation and the heat escaped from the interior glass before it enters a room. Thus, the supply-air window is often applied in cold climates to function as both a heat recovery device and a solar collector. Similar to the supply mode, the indoor circulation mode is also suitable for winter conditions. In the exhaust mode, indoor air is drawn out through the channel to cool the glass panes and remove accumulated heat in the cavity. Thus, the exhausting airflow window is often treated as a passive cooling system in summer. The airflow window operated in outdoor circulation mode holds the same function as the exhausting air window. In the dual airflow mode, the supply fresh air could be preheated and cooled by the exhaust air in winter and summer, respectively. Thus, the dual-airflow window is suitable for different climates acting like a heat exchanger. Another possible solution to achieve good performance in regions that have both heating demands in winters and cooling demands in summers is using reversible ventilated windows. In the reversible ventilated windows, airflow is operated in indoor air curtain mode under winter conditions and operated in outdoor air curtain mode under summer conditions. It should be mentioned that, the inner glass of the double windows illustrated in Figure 2-2 could be an insulated double-glazing units to improve the window thermal performance.

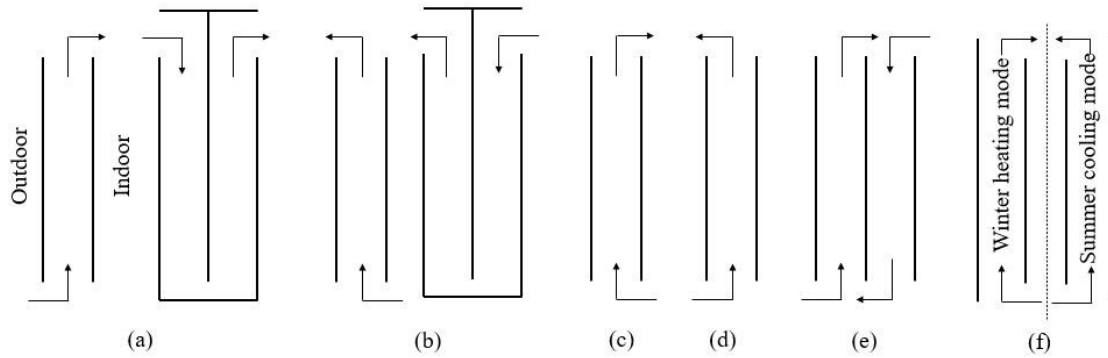


*Figure 2-2 Ventilation modes: (a) supply mode; (b) exhaust mode; (c) indoor circulation mode; (d) outdoor circulation mode; (e) dual airflow mode; (f) indoor circulation mode in winter and outdoor circulation mode in summer*

### 2.2.2 Application of flowing liquid — Liquid-flow windows

The applied liquids in multi-glazing windows can be divided into three categories: pure water [34], anti-freeze liquid [35] and coloring liquid [36–38]. The application of flowing liquid could improve the window's heat storage behavior and the absorbed heat in liquid could be used to pre-heat the domestic hot water through fluid circulation. The fluid circulation can be designed as closed-loop circulation or open-loop circulation. In the closed-loop system (Figure 2-3(a)), the fluid in the cavity between two glass panes keeps circulating inside and it exchanges heat with the feed water through the heat exchanger. To reduce piping requirement, Chow et al. proposed a closed-loop system with a submerged heat exchanger, as shown in Figure 2-3(b) [39]. In the open-loop circulation (Figure 2-3(c)), the feed water is directly supplied into the cavity to absorb solar heat gain and is later extracted from the cavity.

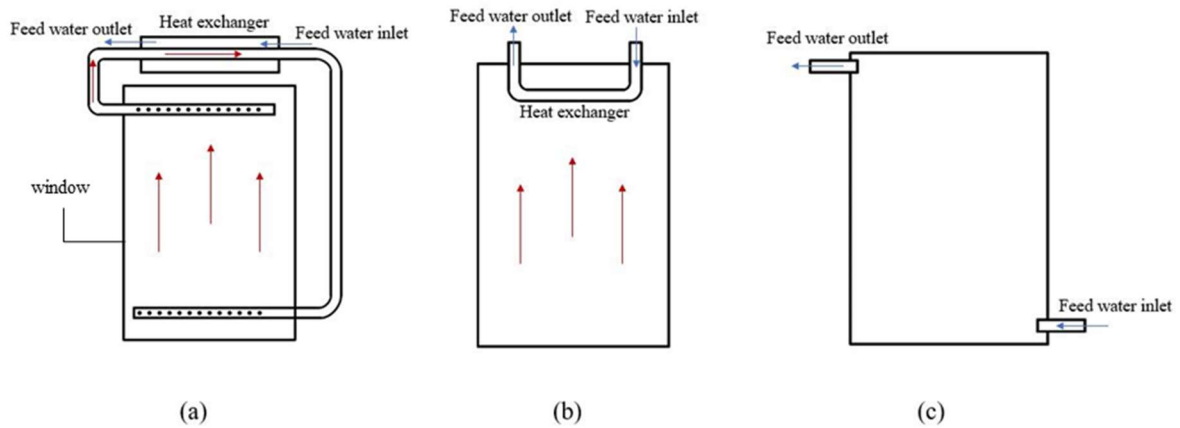


Figure 2-3 Fluid circulation: (a) closed-loop circulation; (b) closed-loop circulation with submerged heat exchanger; (c) open-loop circulation

The simple liquid-flow window configuration is composed of two glass panes and a liquid-flow layer. Due to the fact that the thermal conductivity of liquid is higher than that of air, some configurations made of triple or multiple glass panes (as shown in Figure 2-4) have been proposed to integrate liquid-flow layer with some components of low thermal conductivity, such as air layer [40], inert gas layer [41] and vacuum gap [42].

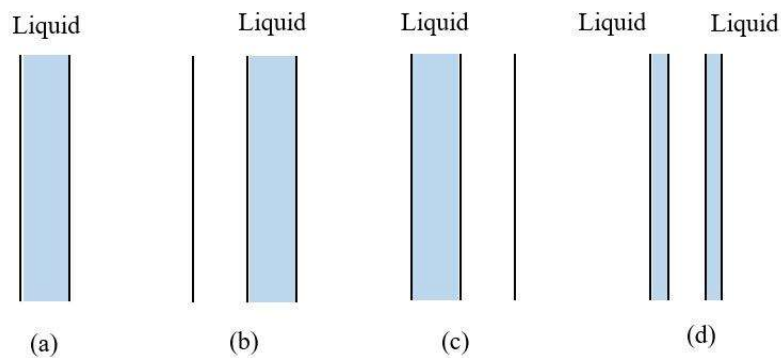


Figure 2-4 Configurations of liquid-flow windows

Another characteristic of liquid-flow windows is that the inlet liquid temperature is sometimes controlled at a constant value. According to this, the liquid-flow window could function as a heating or cooling radiator to achieve the desired performance. The control systems and strategies are different from case to case as shown in Table 2-1.

*Table 2-1 Control systems and strategies of inlet water temperature*

<b>Configuration</b>	<b>Control system</b>	<b>Control strategy</b>	<b>Ref</b>
Glass/ water/ glass;	Electric heater	The inlet temperature is taken as a constant value;	[43,44]
Glass/ argon/ glass/ water/ glass;	Ground source heat exchanger	The inlet temperature is taken as a constant value; Water keeps circulating in summer, and it stays in the cavity until reaching 35 °C in winter;	[45]
Glass/ vacuum gap/ glass/ water/ glass (cooling season); Glass/ water/ glass/ vacuum gap/ glass (heating season);	Not mentioned	The warm water is supplied when there are more than 15 days with daily average temperature lower than 21 °C, and cold water is supplied for the remaining period.	[42]
Glass/ water/ glass/ air/ low-e glass/ water/ glass;	Ground source heat exchanger	For the outer fluid, its inlet temperature is taken as outdoor air temperature; For the inner fluid, its inlet temperature is fixed at 16.7 °C.	[46]
Glass/ water/ glass/ air/ low-e glass/ water/ glass;	Ground source heat exchanger	For the outer fluid, its inlet temperature is taken as outdoor air temperature; For the inner fluid, its inlet temperature is fixed at 22.9 °C.	[47]
Glass/ water/ glass/ air/ glass/ water/ glass;	Not mentioned	For the outer fluid, its inlet temperature is taken as ambient temperature; For the inner fluid, its inlet temperature is fixed at constant value (34 °C, 37 °C and 40 °C) in January, February and December, and it is set as ambient temperature in other months	[48]

### 2.2.3 Application of aerogels — Aerogel Windows

Aerogels are porous materials that have a super lightweight property and a low thermal conductivity. In this view, aerogels are often used in double glazing as an additional insulation layer. The employed aerogels can be divided into two categories: granular aerogels and monolithic aerogels [49]. Compared to the granular aerogels, monolithic aerogels show better performance in terms of higher light transmittance together with higher insulation performance

[50]. Nevertheless, the application of the monolithic aerogel is restricted due to the difficulty in the production of monolithic aerogel with a high optical quality [51].

#### 2.2.4 Application of PCMs — PCM windows

A PCM is a substance which is capable of releasing/absorbing a large amount of energy in the form of latent heat based on phase changing. The phase transition can be classified into four states: solid–solid, solid–liquid, gas–solid and gas–liquid [52]. For practical purposes, only solid–liquid PCMs can be used for building applications [53]. There are a wide variety of commercial PCMs with different melting temperatures. Commonly, PCMs are classified into three types: organic (e.g., paraffin, fatty acid), inorganic (e.g., salt hydrates and metals) and eutectic (e.g., capric + lauric acid) [54,55]. Each type of PCM has some advantages and disadvantages for use in buildings, which have been summarized in previous studies [52,53]. The main limitation for most PCMs is the low thermal conductivity, which indicates that a long time is required to complete the melting or solidification process [55]. This adds the difficulty of PCM applications in buildings. To enhance the thermal conductivity of PCMs, a number of approaches have been proposed, such as adding metal structures, microparticles and nanoparticles and impregnating porous materials with PCMs [53,55,56]. Among these approaches, the addition of nanoparticles has attracted more and more attention due to the fact that nanoparticles have super high thermal conductivities and small sizes (less than 100 nm). Nanoparticles could be divided into the following types: carbon-based, ceramic-based, metal-based, polymer-based and semiconductor [56]. The excellent performance of nanoparticles in improving the thermal conductivity of PCMs has been revealed in studies [57,58]. Nano-enhanced PCMs have been applied in some fields to improve the energy storage capacity [56,59], but their application in multi-glazing windows is still limited.

The use of PCMs as an inter-pane medium could improve the thermal inertia of windows. The simple prototype of PCM glazing is composed of two clear glass panes and a PCM layer (Figure 2-5(a)). Due to the fact that the PCM has a higher thermal conductivity than the air layer, some researchers have proposed multi-panes glazing as shown in Figure 2-5 by filling



the PCM in the inner or outer cavity [60,61] or integrating the PCM layer with the aerogel layer [62] to achieve the required conductivity. Moreover, the utilization of the outer gas layer or aerogel layer could help activate the PCM's melting process in severe cold climates, and the inner gas layer is suitable for hot climates to avoid overheating phenomenon.

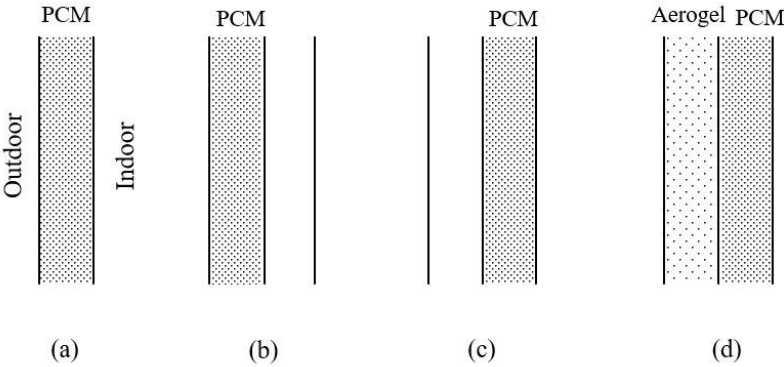


Figure 2-5 Configurations of PCM glazing

The advantages of disadvantages of each advanced inter-pane medium in real applications are summarized in Table 2-2.

Table 2-2 Comparison of different application technologies

Inter-pane medium	Advantages	Disadvantages
Airflow	<ul style="list-style-type: none"> <li>- Light-weight;</li> <li>- Transparent.</li> </ul>	<ul style="list-style-type: none"> <li>- Condensation problem under humid conditions and at low ambient temperature.</li> <li>- Additional fans are needed for mechanical ventilation;</li> </ul>
Flowing liquid	<ul style="list-style-type: none"> <li>- Transparent;</li> <li>- High heat capacity.</li> </ul>	<ul style="list-style-type: none"> <li>- Heavy-weight;</li> <li>- Leakage risk;</li> <li>- Additional facilities are needed such as piping and heat exchanger.</li> </ul>
Aerogel	<ul style="list-style-type: none"> <li>- High insulation performance;</li> <li>- Light-weight.</li> </ul>	<ul style="list-style-type: none"> <li>- Durability issue;</li> <li>- Subsidence problem;</li> <li>- Translucent.</li> </ul>
PCM	<ul style="list-style-type: none"> <li>- High thermal energy storage capacity.</li> </ul>	<ul style="list-style-type: none"> <li>- Not translucent in the solid state;</li> <li>- Increased weight;</li> <li>- Leakage problem.</li> </ul>

## 2.3 Performance of different application technologies

### 2.3.1 Ventilation windows

Carlos et al. conducted experiments based on the outdoor test cells built in Portugal and carried out simulations to investigate the effectiveness of supply-air windows in preheating fresh air for different orientations and different climate regions [63,64]. They concluded that the supply-air window could be chosen for any orientation of buildings where pre-heating fresh air is needed even if there is a lack of solar radiation. They also tested different configurations by changing the inner window from a single glass window to a double glass window [65]. But they did not compare supply air windows with conventional multi-glazing windows. Barakat performed experiments in Ottawa, Canada, to compare a supply-air window with a double-glazed insulated window and a triple-glazed insulated window [66]. The supply-air window was a sealed double-glazed window retrofitted by adding extra glazing on the outside. The experiment was conducted for four months during the heating season, and the reductions in energy consumption were shown as 25% and 20% compared to the insulated double-glazed window and triple-glazed window, respectively. In [33], a supply-air triple-glazing window was compared with conventional double- and triple-glazed windows, and it performed better than the conventional ones in terms of daily energy balance.

Skaff and Gosselin also investigated the benefits of introducing the airflow operated in outdoor air curtain mode into different double-glazing units under a summer design condition, in terms of total heat gain [67]. The tested double-glazing units adopted different exterior glass panes with different absorption coefficients. The results pointed out that, the reduction in heat gain caused by the airflow was in the range of 6.8%–55%. The seasonal energy performance of a mechanically ventilated exhausting airflow window in a typical evaporatively-cooled space in Shiraz city is presented in [12]. The average heat gain of the studied window was 16.6% less than that of the absorptive-clear double window during the cooling season from May to September. The authors also studied the impact of the air cavity thickness and the window aspect ratio on the window performance in the hottest month. They found that the heat gains

increased with the increase of the cavity thickness but decreased with the increase of the aspect ratio. Considering that the extra energy consumption of fans will increase when the cavity thickness is decreased, there is a minimum thickness to achieve positive net energy savings, and the minimum thickness is larger for higher aspect ratios. Choi et al. performed CFD simulations for an exhausting airflow window which was composed of an outer clear single glass pane and an inner double low-e glazing [68]. From their results, the weekly cooling energy was reduced by 9% when the ventilated window was applied instead of triple glazing with the same glass panes.

In order to evaluate the performance of a dual-airflow window, a modified EnergyPlus program have been developed [69]. On this basis, Wei et al. carried out a comprehensive parametric study and determined an optimum design for the studied dual-airflow window [70]. The optimized dual-airflow window could save 25% energy for cooling and heating in Guangzhou, 28% in Kunming, 29% in Shanghai, 32% in Beijing and 34% in Harbin, as compared to a conventional triple glazing. In this view, the dual-airflow window has greater potential of energy saving in colder climates.

The energy saving potentials of different reversible ventilated windows have been revealed in several studies [71–75]. Based on the PASLINK test cell in Porto, Leal and Maldonado carried out experiments for a reversible ventilated window (named the SOLVENT window) with fixed double glazing and movable absorptive glazing [71]. The ESP-r based simulations were later validated and performed to compare the SOLVENT window with a double clear glazing window and a solar control window. The energy demand for heating, cooling and lighting was reduced by 16% and 8%, respectively. The performance of a reversible ventilated window made of fixed float glass and moveable absorptive glass under the climates of Hong Kong and Beijing was clearly shown in [72,73]. The authors concluded that the reversible mechanism was not necessary in Hong Kong, but it really had a significant energy saving advantage in Beijing. As reported in [73], the total heat gain was reduced by 24.9% compared to that of a double absorptive-clear glazing system for the summer months in Beijing, but it increased by 46.2% for the winter months.

As a summary, ventilation operation modes, window structures, air flow rates and glazing properties are important parameters which need to be considered in the application of airflow in multi-glazing windows. Attributed to various operation modes, the utilization of airflow could satisfy requirements in different climates.

### 2.3.2 Liquid-flow windows

The double-glazed water-flow window has been extensively studied by a research team in Hong Kong [34,35,39,76–81]. In [77], the heat gains of a variety of single-glazed and double-glazed windows were simulated under a steady-state summer condition. A clear-clear double-glazed window resulted in 380 W/m<sup>2</sup> heat gain, and this value was reduced to 314–319 W/m<sup>2</sup> for the clear-clear water-flow window. Under the climate in Hong Kong, the absorptive-clear water-flow window could reduce annual room heat gain by around 32% in comparison with the absorptive-clear double glazing [78]. When clear-reflective water-flow glazing was utilized, indoor heat gain was reduced by 40% and 13% compared to reflective single glazing and reflective-clear double glazing, respectively [79]. In addition, 22–35% reductions in cooling loads were found in a large sport center by replacing clear-reflective water-flow glazing with conventional double glazing [34]. The annual performance of absorptive-absorptive water-filled glazing with a submerged heat exchanger in nine cities of China was reported in [39]. The results showed that compared to air-cavity double glazing, the room heat gain was reduced by 10–20%, and the net energy savings (heating, cooling and water heating) achieved 916.85–1813.15 MJ/m<sup>2</sup>. Also, a variety of influencing factors including the glazing property [76], glazing height-to-width ratio (GHTWR) [80], water circulation design [81], header design [82], water layer thickness [80], supply water flow rate [81], warm water temperature [81] and concentration of propylene glycol in anti-freeze liquid [35] have been studied by the same research team. The main results are as follows:

- As the GHTWR decreased, the room heat gain was reduced, but the water heat gain was improved until the GHTWR was around 0.4. With a further decrease in the GHTWR, the water heat gain was reduced [80].

- A higher water heat gain but a lower room heat gain could be found in the open-loop system compared with the closed-loop system [81].
- Modifying the opening diameter or distribution of openings on headers had insignificant effects on the indoor heat gain [82].
- As the water layer thickness increased, both the water heat gain and room heat gain decreased [80].
- When the supply water rate increased from 200 ml/min to 400 ml/min, the water heat gain was improved, but no obvious improvement was observed when the rate had a further increase [81].
- Increasing the warm water temperature resulted in a greater room heat gain but a lower water heat gain [81].
- The decrease in the water heat gain could be observed by increasing the anti-freeze concentration [35].

The annual energy performance of a double-glazed water-flow window (see the details in Table 2-1) in the continental climate was evaluated by Gile-Lopez and Gimenez-Molin based on simulations [43,44]. The numerical model was validated by experiments taken in a small box in Madrid, Spain. The energy demand for heating and cooling was reduced by 18.26% compared to the air-filled double glazing. But they did not mention whether the energy used to preheat the water was considered.

The performance of triple-glazed liquid-flow windows could be found in [38,42,45,83]. In [45], the performance of a water-flow window (see the details in Table 2-1) was evaluated based on considering cases with and without the use of water heat gain. Based on the presented annual simulation results in thirteen cities, this review shows a calculation of energy saving rates caused by the utilization of water flow. The energy saving rates were in the range of -12–80% and -2–82% for cases without and with the use of water heat gain, respectively. In their further research, another similar configuration with dynamic control of liquid transparency was proposed and investigated in seven cities [38]. Lyu et al. performed annual simulations for a

vacuum-water flow window (see the details in Table 2-1) in three cities of China [42]. Compared to that of a double-glazed water-flow window, the room heat gain was reduced by around 42% in the cooling climate. While for the heating climate, the use of a vacuum layer reduced not only the heat loss but also the excessive room heat gain when the solar radiation or outdoor temperature was high. An experimental study for the same configuration was carried out in the cooling season of Chengdu, China, by comparing it to a similar configuration with an outer insulation air gap instead of a vacuum gap [83].

Li et al. performed simulations of an office room equipped with a quadruple-glazed double-circulation flow window (see the details in Table 2-1) for the cooling season in Shanghai, China [46]. Simulations were carried out to achieve zero indoor heat gain (case 1) and zero cooling load (case 2) by varying the water flow rate. As compared to the base case with a low-e double-glazed window, the net energy savings for the air-conditioning system, water-heating device and pump were found as 576–635 MJ for case 1 and 926.1–1223.5 MJ for case 2. A related study for the same configuration (see the details in Table 2-1) in Shenzhen is presented in [47]. The authors analyzed the window performance with different water flow rates and different water shading rates. Another study for a similar window configuration (see the details in Table 2-1) was also performed in Shenzhen, China [48]. The results showed that the net energy savings were 305 kWh, 273 kWh and 238 kWh for the cases with 34 °C, 37 °C and 40 °C inlet water temperatures compared to the normal double-glazed window.

Stopper et al. assessed the energy performance of quintuple-glazed double-circulation flow windows in Munich (Germany) and Dubai (UAE), based on simulations [84]. In the studied window, the inner fluid layer was a clear fluid and the outer fluid layer was a clear fluid or dyed fluid. The outer fluid and inner fluid were separated by two Kryton layers. By comparing with the solar control glazing, it was found that the studied window without coloring the outer fluid increased the cooling demand by around 39% in Munich and 25% in Dubai. While for the window with coloring the outer fluid, it decreased the cooling demand by around 23% in Munich and 44% in Dubai, when compared to solar control glazing.

As a summary, the benefits of flowing liquid could be better exerted by optimizing window structures, glazing properties and operation parameters (i.e., liquid circulation mode, liquid flow rate, inlet liquid temperature and liquid transparency). The application of flowing liquid is more suitable for hot climates and temperate climates than for cold climates.

### 2.3.3 Aerogel window

Two cases in Denmark were numerically investigated for assessing the applicability of monolithic aerogel glazing. One was a new built house insulated according to the Danish building code, and the other was a low-energy house insulated according to the passive house standard [85,86]. As concluded by authors, the annual heating demand for the new built house and the low-energy house could be decreased by 19% and 34%, respectively, by replacing argon-filled triple glazing with aerogel glazing. Berardi replaced double glazing with monolithic aerogel glazing in an educational building in Massachusetts (USA) as a retrofit solution [87]. The simulated energy savings were shown around 12%, 14%, 18% and 21% for 40%, 60%, 80% and 100% replacement, respectively. Buratti performed EnergyPlus simulations to evaluate the impact of monolithic aerogel glazing on building energy performance in different cities of Europe [88]. From their given results, energy savings for heating, cooling and lighting could be calculated. The energy saving rates were 3.7–5.6% for Helsinki (Finland), 2.5–4.3% for Turin (Italy), 3.1–5.5% for Paris (France), and –1.6% for Rome (Italy), when compared to low-e double glazing. Wang et al. evaluated the monolithic aerogel glazing performance in different climate areas of China by using the eQuest energy simulation program [89]. From their given results, energy savings for cooling and heating could be calculated compared to a conventional double-glazing window. The energy saving rates were around 14% for Harbin, 10% for Beijing, 9% for Shanghai, 8% for Guangzhou, and 7% for Kunming.

A comparison between granular aerogel glazing, low-e glazing and conventional single glass was adopted in Hong Kong based on EnergyPlus simulations [90]. From the simulations, it was found that the cooling load reduction caused by the aerogel glazing was almost the same

as that caused by the low-e glazing. By properly designing aerogel thicknesses and particle sizes in [91], 8.5% and 5.4% of cooling energy saving could be achieved in Hong Kong compared to the conventional double window and double low-e window, respectively. To balance the requirements of energy savings and visible transmittance, the authors suggested a 12 mm aerogel thickness and 4 mm particle size. Gao et al. numerically investigated the applicability of aerogel glazing in Norway, in terms of the total energy demand for heating, cooling and lighting [92]. The results pointed out that, the use of 14 mm granular aerogel in the cavity between two glass panes instead of air could lead to about 21% reduction in total energy demand. When the aerogel thickness increased to 30 mm, the aerogel glazing had a similar performance with triple low-e glazing. Buratti et al. also investigated the performance of granular aerogel glazing in Rome, Paris and Ottawa [93]. The results showed that the heating energy demand reductions were 13% for Ottawa, 24% for Paris and 29% for Rome, and the cooling energy demand reductions were around 21% for Ottawa, 20% for Paris and 18% for Rome, when compared to conventional double glazing. However, when the aerogel was integrated with low-e glazing, its benefit in reducing cooling demand was negligible. The feasibility of granular aerogel glazing in four cities (i.e., Harbin, Beijing, Changsha, Kunming) in China was assessed in [94] by comparing to conventional double glazing, triple glazing and low-e double glazing. The results showed that the aerogel glazing performed better than the other three glazing in the heating season, but in the cooling season, the low-e double glazing was the most suitable one. To improve aerogel glazing performance in warm and hot regions, Belloni et al. proposed a double-glazing unit filled with a mixture of silica granular aerogel and hollow silica powder [95]. They simulated the energy demand of an office building in Tokyo with different window orientations, based on EnergyPlus software. A reduction (14–24%) in the cooling demand could be observed attributed to the addition of powder. Moreover, the proposed aerogel glazing outperformed low-e glazing with a 22% (north)–62% (south) reduction in heating energy demand.

As a summary, the aerogel thickness and particle size are two important factors that need to be considered in designing granular aerogel glazing. For monolithic aerogel glazing, studies



carried out for investigating its influential factors are still lacking. The utilization of aerogels has great energy saving potential under cold climates but their performance is limited under hot climates. Mixing aerogels with power is a feasible way to improve their performance in hot climates.

#### 2.3.4 PCM Window

The energy performance of double-glazed PCM windows has been evaluated by several researchers in different climate regions [96–104]. Goia et al. compared a double-glazed unit filled with RT35 paraffin and a traditional double-glazed unit by taking experiments in the outdoor test cell (TWINS test facility) located in Torino [97,98]. The comparative analyses showed that the PCM-filled unit performed effectively in summer with a 20%–55% reduction in daily entering energy, while its performance in mid-season and winter was not as favorable as that in summer. In [96], in-situ experiments were conducted in Nanjing (China) based on two identical outdoor chambers installed with a PCM window and a hollow glass window respectively. With experiment data, the numerical model was validated and simulations were then performed based on selected typical days. The simulated energy saving rates were found as 39.5%, -43.5%, -78.9% and -5.8% for the sunny summer day, the rainy summer day, the sunny winter day and the rainy winter day, respectively. A similar performance was reported in a study performed in Changsha, another city of China with hot summers and cold winters [103]. Further investigations of the PCM window in Nanjing were carried out by [99] with varying the latent heat of fusion, melting temperature and difference between liquidus temperature and solidus temperature. A higher energy saving rate was observed when the latent heat of fusion increased from 205 kJ/kg to 287 kJ/kg. In relation to three melting temperature ranges, the energy saving rate was decreased from 18.3% to 8.5% and 10.5% when the melting temperature of 27–29 °C altered to 31–33 °C and 23–25 °C, respectively. In this view, the authors suggested the melting temperatures of 25 °C–31 °C for summer conditions in Nanjing. A similar trend of the energy saving rate could be observed in varying the temperature differentials between liquidus temperature and solidus temperature of the PCM. Liu et al. conducted experiments in a small-scale test facility located in Daqing (China) on two sunny

days in October [102]. Based on the measured data, the numerical model was validated to simulate the PCM glazing performance with different melting temperatures (14–16 °C, 16–18 °C and 18–20 °C) and different PCM filling thicknesses (4–50 mm) on a typical summer day. The authors found that, the total transmitted energy decreased by 109.1% as the PCM thickness increased from 4 mm to 50 mm when the melting temperature was 14–16 °C. But the trend of total transmitted energy was not always consistent with the increase in PCM thickness. Increasing the thickness may lead to a reversed trend for some PCMs. This result is in agreement with [104], in which the total transmitted energy was effectively reduced with increasing the PCM thickness from 4 mm to 30 mm, but the trend was reversed when the thickness was further increased to 50 mm. More comprehensive parametric studies based on a typical summer day in Daqing could be found in [100,101].

There are few studies have been carried out for learning the application performance of nano-enhanced PCMs. Li et al. investigated nano-PCM double-glazing units based on simulations. They selected representative days in summer, autumn and winter in Daqing city to perform simulations to test four different combinations of nanoparticle enhanced PCMs considering nanoparticle volume fractions which are 1% and 10% and nanoparticle diameters which are 10 nm and 100 nm [105]. It was found that the heat gain was larger for a higher volume fraction, but the influence of the nanoparticle diameter on the heat gain was the opposite. Another interesting finding is that the magnitude of the impact of the studied parameters was dependent on the season and the highest one was in winter. In their another study [106], the impact of different nanoparticle types (i.e., Cu, CuO and Al<sub>2</sub>O<sub>3</sub>), volume fractions (i.e., 0.1–10%) and sizes of nanoparticles (i.e., 5–25 nm) on window performance under summer conditions was investigated. They recommended CuO nanoparticles with a size under 15 nm and a volume fraction below 1%.

Assessments of triple-glazed PCM windows have been reported in [60,62,107,108]. Li et al. also carried out experiments for a triple glazing filled with PCM in the outer cavity (TW + PCM) on summer days. On the sunny summer day, the heat gain was reduced by 16.6% and 28%, and on the rainy summer day, it was reduced by 14.7% but increased by 4.5%, as

compared to that of the PCM double window (DW + PCM) and conventional triple glazing (TW), respectively. A similar triple-glazed configuration with an inner argon insulation layer was investigated in summer conditions of Lodz city based on ESP-r software [107]. The simulated results showed that the cooling energy saved by the PCM window was 14.7–25% for the east orientation and 11.2–17.1% for the west orientation, when compared to a traditional window. Li et al. proposed a triple-glazed aerogel-PCM window, and they numerically analyzed the influence of the thermal conductivity, density, specific heat and thickness of silica aerogel on the window energy performance in the severe cold climate of China [62]. Among the studied parameters, the thermal conductivity and thickness were the two most important factors. As expected, the lowest energy consumption was found when the thermal conductivity was the lowest and the aerogel thickness was the largest. While there was no latent heat of PCM exploited when the aerogel had large thicknesses such as 40 mm and 50 mm. In this view, the 30 mm aerogel was recommended for the studied climate conditions. Further comparative and parametric studies were recently conducted by [108]. Ten different glazing configurations were proposed: double-glazed window (DW), double-glazed PCM window (DW-Par), double-glazed aerogel window (DW-Sil), triple-glazed window (TW), triple-glazed window with inner PCM layer (TW-Par), triple-glazed window with outer aerogel layer (TW-Sil), triple-glazed aerogel-PCM window (TW-Sil-Par), and three improved TW-Sil-Par for optimization purposes. It was found that when applying PCM in either double or triple glazing, the energy consumption was improved due to the fact that the PCM layer has lower conductivity than the air layer with the same thickness. In addition, compared to DW, the energy savings were 11.41% for TW-Par and 16.35% for TW-Sil-Par. With a further optimization of TW-Sil-Par, the energy saving rate could achieve 70.16% compared to the DW.

As a summary, the feasibility of applying PCM in multi-glazing windows is highly related to window structures, PCM filling thickness and PCM properties (e.g., conductivity, melting temperature and latent heat). Studies on PCM glazing have mainly been conducted on typical days, while there are few studies to assess its seasonal or annual performance to reveal its

applicability under different climates and determine optimum designs. In addition, the application of nano-enhanced PCMs in multi-glazing windows still needs further exploration.

### 2.3.5 A comparison of different window technologies

In this section, the reported seasonal and annual energy savings for cooling and heating caused by the utilization of advanced inter-pane medium instead of air layer are summarized in Figure 2-6.

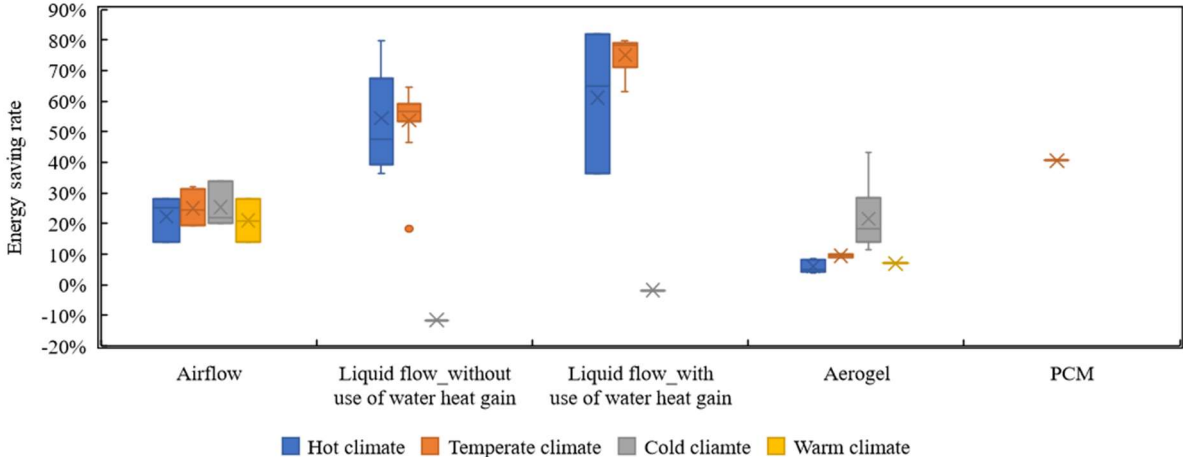


Figure 2-6 Energy saving potential of airflow [66,70], flowing liquid [38,43–45], aerogels [51,87,91,93,109] and PCMs [96] in different climates

As shown in Figure 2-6, the average energy saving rates caused by the application of airflow are 22% for hot climates, 25% for temperate climates, 25% for cold climates and 21% for warm climates. In terms of flowing liquid, the average values are 54% and 61% for hot climates, 54% and 75% for temperate climates and -12% and -2% for cold climates, with and without the use of water heat gain, respectively. This indicates that the application of flowing liquid is more suitable for hot climates and temperate climates than for cold climates. In terms of aerogels, the average values are 6% for hot climates, 7% for warm climates, 10% for temperate climates, and 22% for cold climates. In this view, the application of aerogels is more suitable for heating conditions than cooling conditions. In terms of PCMs, the value is 41% in Nanjing. Future studies for investigating the year-round energy performance of PCM applications in different climates are required. Moreover, by comparing the average energy

saving rates of different inter-pane media under the same climate, it could be concluded that the flowing liquid, airflow, flowing liquid and aerogel have the largest energy saving potential in hot climates, warm climates, temperate climates and cold climates, respectively.

## 2.4 Conclusions

Multiple pane windows (including double-glazed windows and double windows) have attracted increasing attention over the recent years due to their effective performance in saving energy consumption. The common medium between two glass panes is stationary air or inert gas and it could be treated as an extra component in multiple pane windows. This opens possibilities to apply different fluids and promising filling materials, including airflow, flowing liquid, aerogel and phase change material (PCM), as advanced inter-pane medium to further enhance window performance. The performance of application technologies (i.e., ventilation window, liquid-flow window, aerogel window and PCM window) has been summarized and compared in this chapter. Among the above-mentioned technologies, the supply-air double window attracts our attention and its U-values are further investigated in next chapters.

## **3 Experimental Setup and Results**

### 3.1 Introduction

In existing studies, the U-values of supply-air windows are normally tested in in-situ experiments, by measuring heat flux together with recording the inside and outside air temperatures [15,110]. In these experiments, the experimental boundary conditions are not steady-state conditions. In addition, the heat flux is typically measured by attaching heat flux meters on the surfaces of glass and the measured U-value is actually the center-of-glass U-value rather than the U-value of a whole window. In current studies, the laboratory experiments of supply-air double windows under steady-state conditions are still rare.

Among standard U-value measurement methods, the hot box method (including the CHB method and GHB method) can accurately measure the total U-value of windows with inhomogeneous structures. The standardized GHB method for testing a single-glazed window is provided in [22]. Before testing a window, the calibration test is required to determine the heat losses of GHB. The calibrated heat losses include two parts. The first part is from the metering box to guarding box including the heat loss of metering box walls, the heat loss from contact points between the metering box and sample frame, and the air infiltration heat loss. The second part is from the metering box to cold box through the contact points between the tested sample and sample frame. While as stated in ISO 8990 [17] “*the standard method does not provide for measurements where there is mass transfer through the specimen during the test*”, the provided standardized method is not adapted to testing a supply-air double window. More specifically, once the air is introduced from the cold box to metering box, the input power of metering box is partly used to heat the supplied air. This part of heat, however, is hard to be quantified due to insufficient air mixing and air infiltration. To solve this problem, Appelfeld and Svendsen [111] added a tube in the GHB to return the supplied air to the cold box. While in their experiments, the additional heat loss due to the installation of a tube was not considered. Additionally, they didn’t mention how to determine the sampling flanking loss for a supply-air double window.



To address the above-mentioned problems, this chapter proposes an improved GHB method for supply-air double windows. The improved parts include the GHB setup and GHB calibration procedure. The purposes of this chapter include:

- (1) Identify thermal performance of supply-air double windows.
- (2) Compare different window configurations including a single-glazed window, a clear double-glazed window, a Low-E double-glazed window, supply-air double windows and closed-air double windows.
- (3) Validate future numerical models.

This chapter include five sections. Section 3.1 points out the necessity of improving the GHB method to test supply-air double windows. Section 3.2 introduces the conventional GHB method and the adjusted and highly improved GHB method. Section 3.3 presents the experimental results and compares the thermal performance of different window configurations. Section 3.4 concludes this chapter.

## 3.2 Experimental setup development

In this study, the guarded hot box is utilized to test U-values of different window configurations. In addition, to quantitatively analyze the deviation between the window U-value and center-of-glass U-value, the heat flux meter is used to measure the center-of-glass U-value.

### 3.2.1 Guarded hot box

A guarded hot box constructed in LTDS/ENTPE (as shown in Figure 3-1) has been adapted and improved for the purpose of our study. The metering box has exterior dimension of 1420 mm (length)  $\times$  1420 mm (width)  $\times$  725 mm (depth) and interior dimension of 1020 mm (length)  $\times$  1020 mm (width)  $\times$  525 mm (depth). Its walls are constructed by extruded polystyrene (XPS) board, plywood and aluminum protective coat. The guarding box has an outer size of 2060 mm (length)  $\times$  2060 mm (width)  $\times$  1020 mm (depth). The air thickness between side walls of guarding box and metering box is 225 mm and that between back walls is 190 mm. The dimension of cold box is 2060 mm (length)  $\times$  2060 mm (width)  $\times$  1020 mm (depth). The sample frame is constructed by the same material as the metering box and its opening size is 1020 mm  $\times$  1020 mm. For specimens smaller than the sample frame opening, XPS boards are used to fill the gap. To prevent air leakage from the metering box to cold box, the joints between the sample perimeters and sample frame are sealed by tapes. Twenty-two clamp mechanisms are employed to lock the cold box and sample frame, the metering box and sample frame, and the guarding box and sample frame. In addition, incompressible gasket material is utilized to minimize the air infiltration of the metering box.



*Figure 3-1 Guarded hot box in ENTPE*

The schematic of the guarded hot box is shown in Figure 3-2. In the metering box, there are two square-fin heaters attached on the back wall and bottom wall, respectively. The input power of each heater is controlled to achieve and maintain a desired air temperature. A wooden baffle painted black is installed in the metering box and it is parallel to the sample to form an airflow channel. Three DC-powered axial flow fans are installed at the top of baffle. The power input to the fans is considered to be completely converted into heat when the air temperature of metering box achieves a steady state. Similar to the metering box, one wooden baffle and three DC-powered axial flow fans are installed in the cold box. The cold box is also equipped with a glycol cooling system. The guarding box is used to minimize lateral heat loss of the metering box walls by keeping the air temperature of the guarding box as the same as the metering box. There are four square-fin heaters in the guarding box. The control of the input voltage to the heaters and fans is made using LABVIEW.

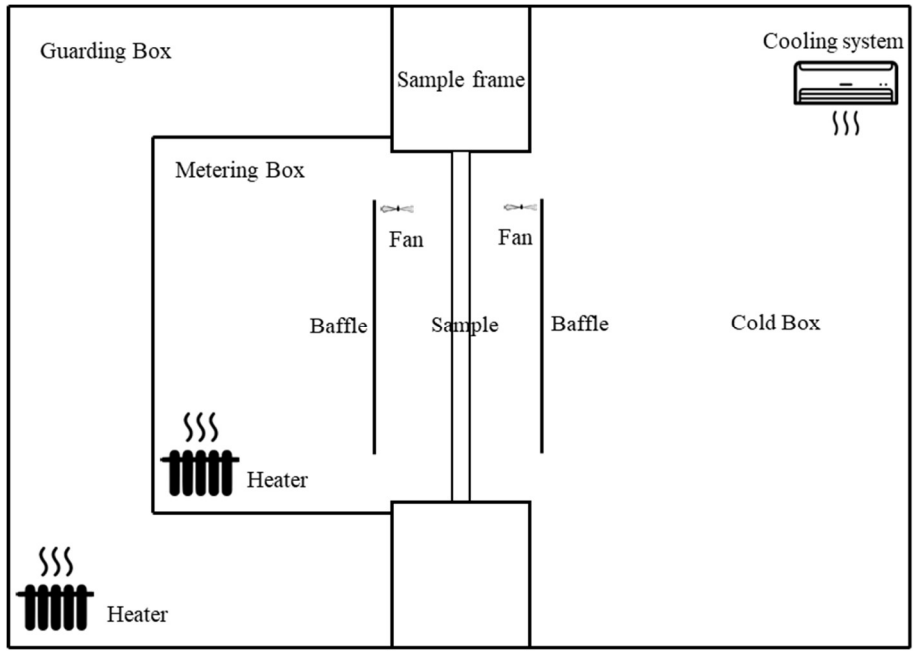


Figure 3-2 Schematic of the guarded hot box

(1) Measurement instrument, data acquisition and control system

The data acquisition and control systems are of importance to accurately identify window thermal transmittance. The schematic of the established data acquisition and control system during this PhD work is shown in Figure 3-3.

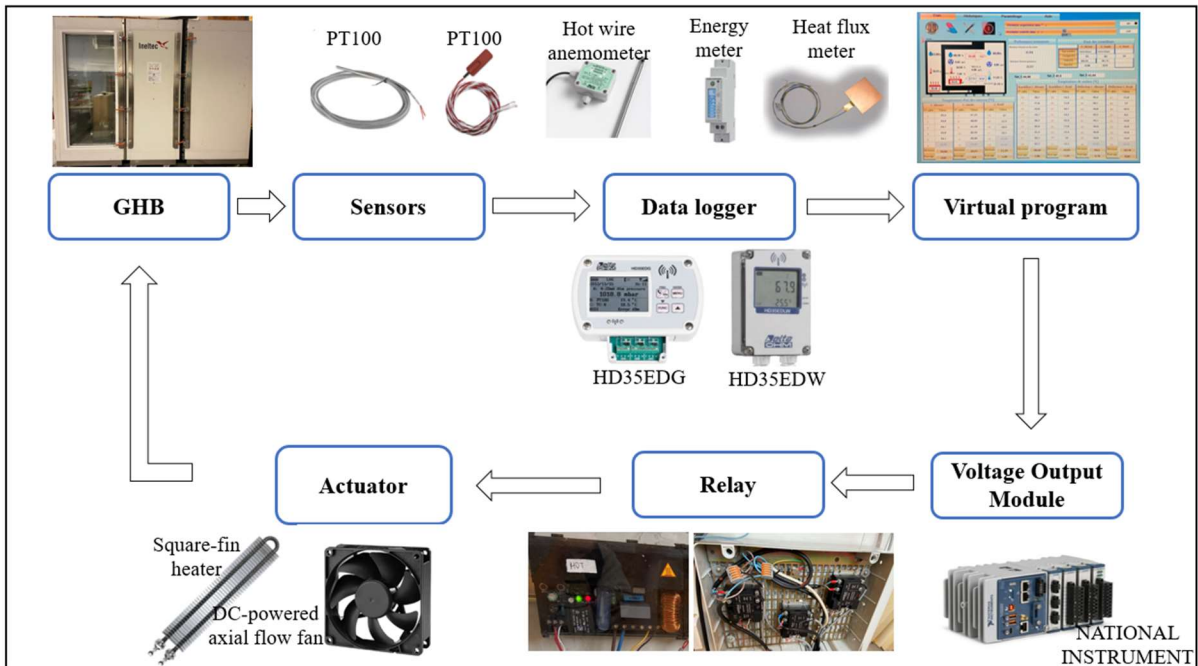


Figure 3-3 Data acquisition and control system

In our tests, the measurement instrument includes 4-wire PT100 patch sensors (30mm × 15mm), 4-wire PT100 platinum probes (4mm Diameter, 50mm Long), hot wire anemometers, heat flux meters (manufactured by Captec, 100mm × 100mm) and energy meters. The detailed information of sensors is summarized in Table 3-1.

*Table 3-1 Information of sensors*

<b>Instrument</b>	<b>Parameter measured</b>	<b>Uncertainty</b>
PT100 temperature sensors	Temperature, °C	±0.15 °C
Hot wire anemometer	Air velocity, m/s	±3%
Heat flux meter (Captec)	Heat flux, W/(m <sup>2</sup> K)	±3%
Energy meter	Input power, W	±1%

The sensors are connected with radio data loggers (DeltaOHM HD35EDW, HD35EDG) which have terminal header inputs. The data loggers store measurements in the internal memory and send them automatically to the base unit (HD35AP) at an interval of 2s. The base unit acts as an interface between the data loggers positioned in measurement sites and the computer with HD35AP-S basic PC software. It communicates wireless with the remote data loggers.

The acquired data (i.e., air temperature and air velocity) are fed into the proportional-integral-differential (PID) controller as input feedback. The PID controllers are built on the LABVIEW platform, as illustrated in Figure 3-4. The outputs of controllers are then transmitted into the Voltage Output Module of NATIONAL INSTRUMENT (NI-9263) for converting transmitted output signals into analog signals. The analog signals are provided as inputs of relays which permits a small amount current to control high current loads. The controlled loads are then provided to the actuators.

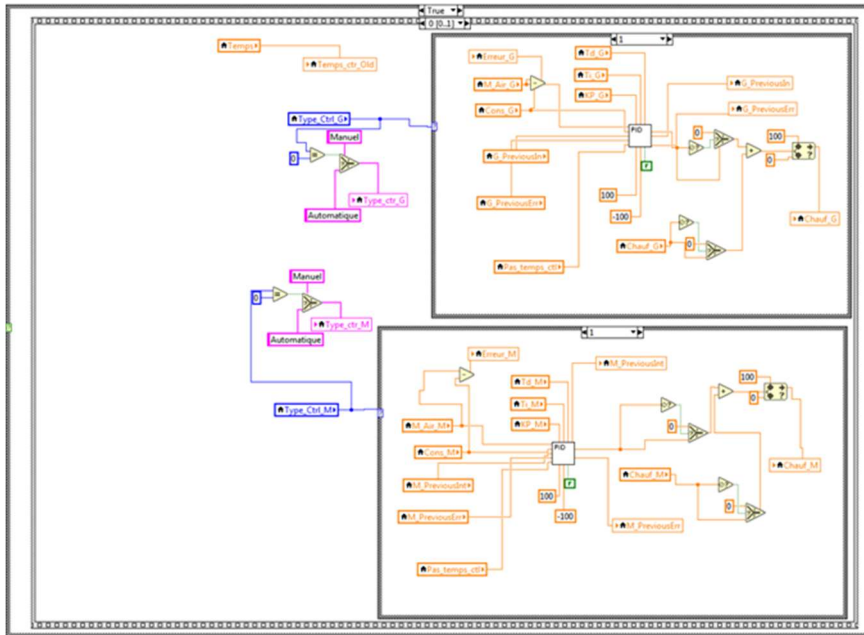


Figure 3-4 Interface of PID controllers

As mentioned in [112], “the controllers shall keep any random temperature fluctuations and long-term drifts within 1% of the air-to-air temperature difference over the specimen for at least two consecutive test periods.” Figure 3-5 shows an example of temperature variations in the guarding box, metering box and cold box during a calibration test. The air temperature difference between hot and cold sides is 24.8 °C. After 15h running, the maximum temperature fluctuations are 0.06 °C in metering box, 0.07 °C in guarding box and 0.13 °C in cold box.

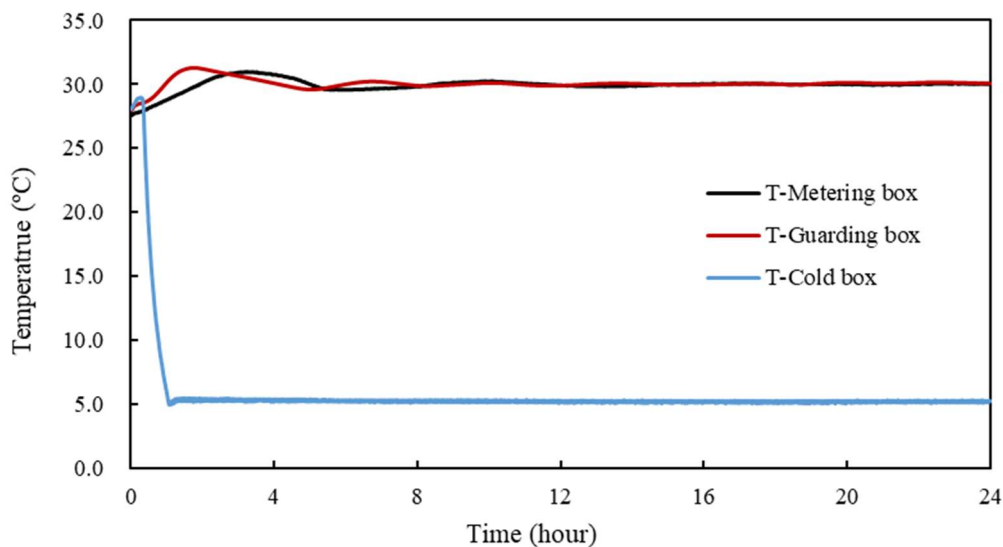


Figure 3-5 Air temperature profiles during a calibration test

### 3.2.2 Conventional GHB method

#### (1) Calibration procedure

In the calibration test, the heat losses required to be calibrated include the extraneous heat loss and sample flanking loss. The extraneous heat loss represents the heat loss from metering box to guarding box and it is the sum of the heat loss through metering box walls, the flanking loss occurred at the contact points between metering box and sample frame, and the heat loss due to air infiltration. The sample flanking loss represents the heat loss from metering box to cold box and it occurs at the contact point where the specimen touches the sample frame. The calibration steps are summarized as follows.

Step 1: Determine the extraneous heat loss by placing a sample frame without opening between the metering box and cold box (as shown in Figure 3-6) or placing a XPS with homogeneous structures in the opening of sample frame together with controlling the temperature of metering box as the same as that of cold box. The extraneous heat loss can be calculated as Eq. (3-1).

$$Q_{ex} = Q_{in} - Q_F \quad (3-1)$$

Where,  $Q_{ex}$  is the extraneous heat loss, W;  $Q_{in}$  is the input power of heaters, W;  $Q_F$  is the heat transferred through the sample which can be measured by heat flux meters, W.

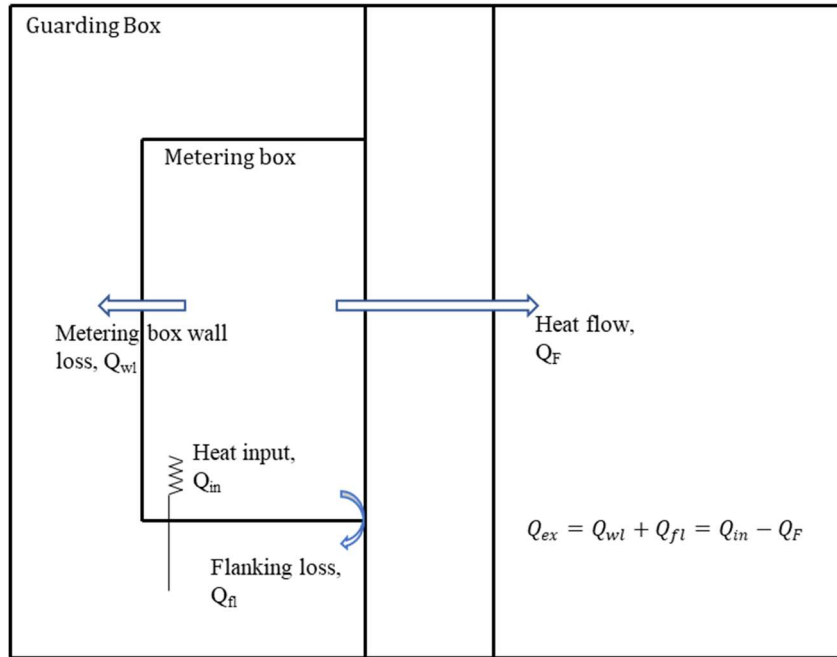


Figure 3-6 Schematic of step 1

Step 2: Determine the sample flanking loss, by putting a XPS plate with homogeneous structure in the opening of the sample frame (as shown in Figure 3-7). It can be calculated as Eq. (3-2).

$$Q_{sfl} = Q_{in} - Q_{ex} - Q_F \quad (3-2)$$

Where,  $Q_{sfl}$  is the sample flanking loss, W.



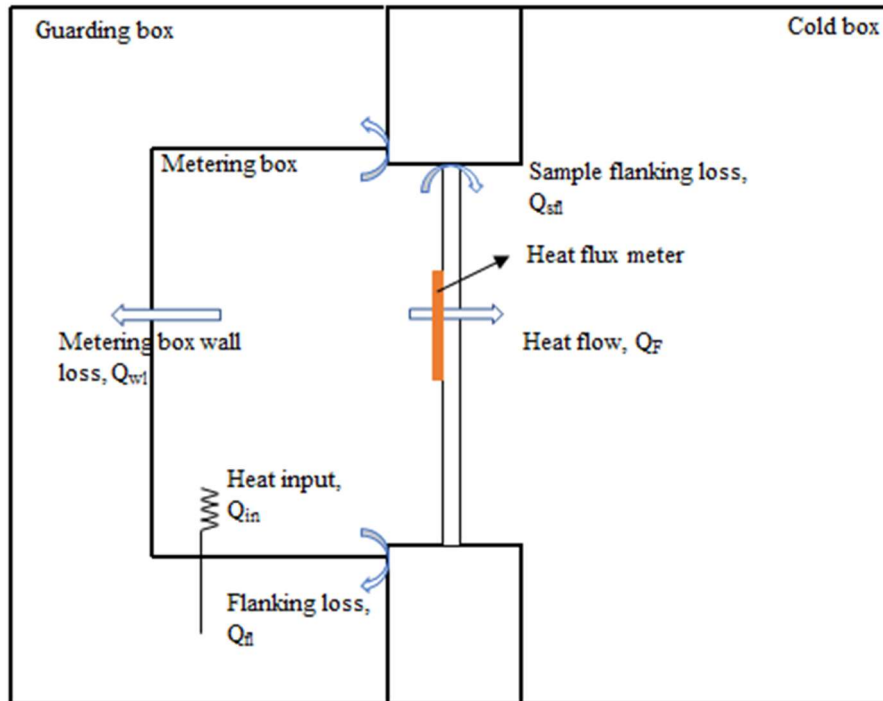


*Figure 3-7 Schematic of step 2*

In the calibration tests, fourteen air temperature sensors are installed in the guarding box, metering box and cold box. The measured temperatures of each box are averaged and transmitted into the PID controller. In addition, nine surface temperature sensors are attached on the surfaces of baffles and XPS plates, respectively. Two hot wire anemometers are put in the middle of the airflow channel between the baffle installed in the metering box/cold box and the tested sample. Besides, the power input to the heaters and axial flow fans installed in the metering box are monitored by energy meters separately. Also, heat flux meters are attached on the surface of tested sample. The measurement time step is one minute. The locations of sensors are shown in Figure 3-8 and Figure 3-9.

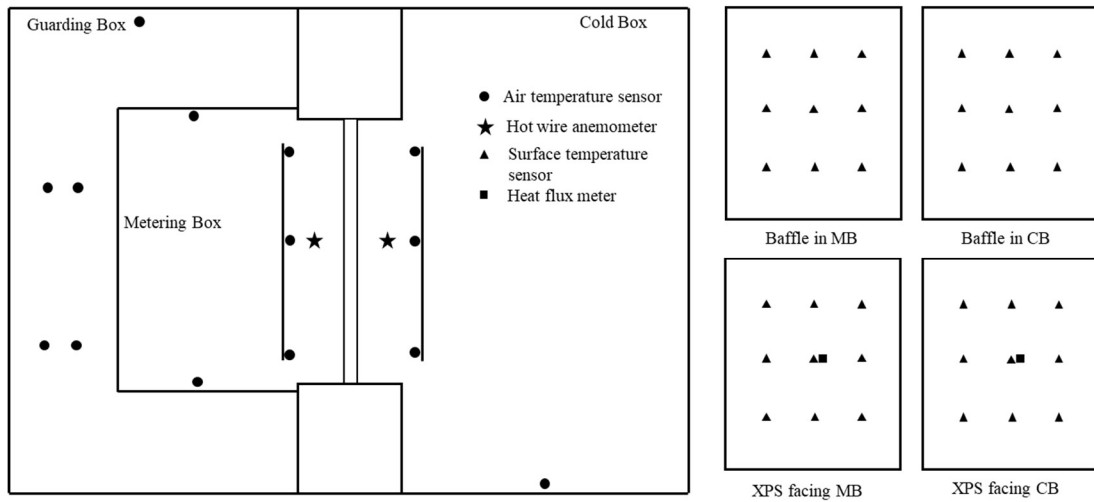


Figure 3-8 Locations of Sensors in the calibration test



Figure 3-9 Picture of the calibration test

The monitored surface temperatures are latter used to determine the convective heat transfer coefficients in hot and cold sides. The convective heat transfer coefficient can be determined by the convective heat flux and the difference between surface temperature and air temperature:

$$h_c = \frac{q_c}{T_s - T_a} = \frac{q_F - q_r}{T_s - T_a} \quad (3-3)$$

Where,  $h_c$  is the convective heat transfer coefficient, W/(m<sup>2</sup> °C);  $q_c$  is the convective heat flux, W/m<sup>2</sup>;  $T_s$  is the surface temperature, °C;  $T_a$  is the air temperature, °C;  $q_F$  is the measured heat flux, W/m<sup>2</sup>;  $q_r$  is the radiation heat flux, W/m<sup>2</sup>.

The radiation heat flux can be quantified according to the following formulas:

$$q_r = E \cdot h_{ro} \cdot (T_s - T_r) \quad (3-4)$$

$$h_{ro} = 4\sigma T_m^3 \quad (3-5)$$

$$T_m^3 = \frac{(T_r^2 + T_s^2) \cdot (T_r + T_s)}{4} \quad (3-6)$$

$$E = \frac{1}{\frac{1}{\varepsilon_1} + \frac{1}{\varepsilon_2} - 1} \quad (3-7)$$

Where,  $h_{ro}$  is the radiative heat transfer coefficient, W/(m<sup>2</sup> °C);  $E$  is surface emissivity;  $T_r$  is the mean radiant temperature seen by sample (i.e., the mean temperature of baffle surface seen by sample), °C.

## (2) Window testing procedure

In the window testing procedure, the boundary conditions including the air temperatures of cold box and metering box as well as the air velocities in hot and cold sides need to be controlled as the same as those in the calibration test.

The U-value of a tested window is calculated as Eq. (3-8):

$$U = \frac{Q_{in} - Q_{ex} - Q_{sfl}}{A \cdot \Delta T_{MB-CB}} \quad (3-8)$$

Based on the conventional GHB method, three different window configurations are tested, including a clear single-glazed window, a clear double-glazed window and a Low-E double-glazed window (as shown in Figure 3-10). These windows have the same dimension of 888 mm × 888 mm and they are made of wooden frames with a thermal conductivity of 0.13 W/(m K). The thickness of glass is 4 mm and for the clear double-glazed window and the Low-E double-

glazed window, the gap width between two glasses is 12 mm. For the Low-E double-glazed window, the Low-E film is facing the closed air cavity.



Figure 3-10 Picture and schematic of tested windows

### 3.2.3 Adjusted GHB method

#### (1) Adjustment of GHB setup

As shown in Figure 3-11, a tube is installed to be connected with the outlet of the tested supply-air double window. Attributed to the tube, the supplied air is returned back to the cold box instead of entering into the metering box. To reduce the heat loss from the installed tube, the tube is wrapped with glass wool which is typically used as insulation material. Additionally, for the part of the tube that is exposed to the metering box, the rubber plastic cotton is also used as an additional insulating layer. Before testing a window, the tube loss needs to be calibrated.

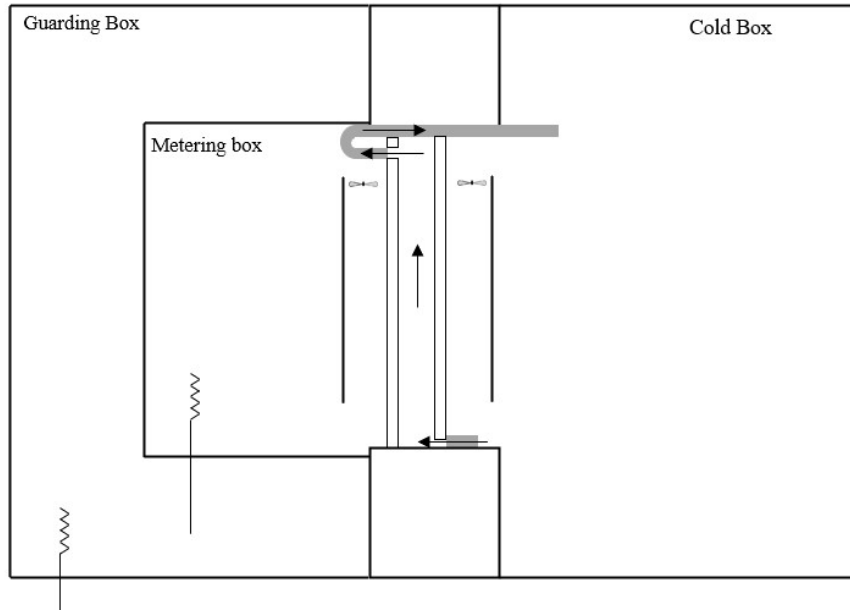


Figure 3-11 Schematic of the adjusted GHB

## (2) Adjustment of calibration and testing procedure

For the supply-air double windows, the sample flanking loss happens at the contact points between the interior window and the sample frame. The sample flanking loss is related with the air temperatures and velocities in both sides of the interior window. One side of interior window is facing the metering box and the other side is facing the airflow channel. So, before identifying the sample flanking loss, the air temperature and air velocity of airflow channel needs to be measured at first. The measured values are then used as the input of the controllers in the calibration test of sample flanking loss to control the air temperature and velocity in cold side. The calibration and window test procedure are shown as follows:

Step 1: Determine the extraneous heat loss ( $Q_{ex}$ ) which is the sum of metering box loss ( $Q_{wl}$ ) and flanking loss ( $Q_{fl}$ ).

Step 2: Put a supply-air double window in the adjusted GHB setup. As shown in Figure 3-12, three air temperature sensors are placed in the airflow channel to get the average air temperature and one hot wire anemometer is put at the middle point of airflow channel to measure the air velocity. In addition, one air temperature sensor is placed at the inlet and outlet vent, respectively.

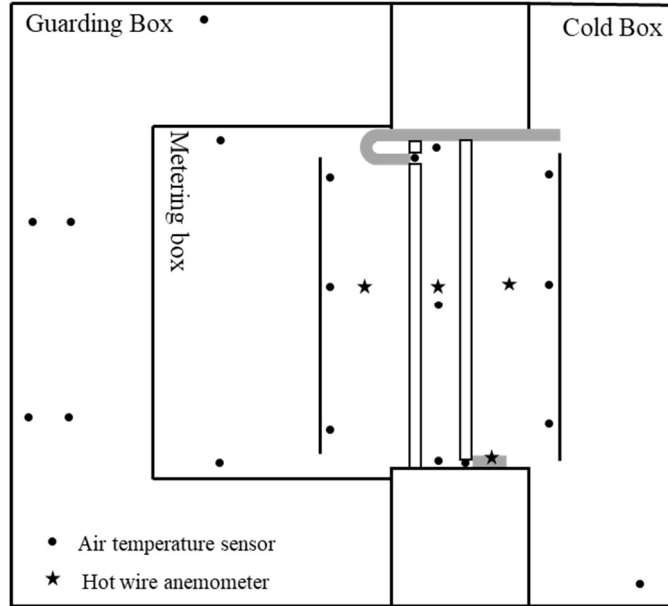


Figure 3-12 Positions of sensors

Step 3: Determine the sample flanking loss ( $Q_{sfl}$ ), by putting a XPS plate with homogeneous structure in the opening of the sample frame. The air temperature of cold box is controlled as the average temperature of airflow channel measured in step 2, and also the air velocity in cold side is set as the air velocity measured in step 2.

Step 4: Determine the tube heat loss ( $Q_{thl}$ ) by the putting a single-glazed window in the opening of the sample frame and installing the insulated tube (as shown in Figure 3-13). The inlet air temperature of tube is controlled as the outlet air temperature measured in step 2, and the inlet air velocity of tube is set as the inlet air velocity of the supply-air double window. The input power of metering box is measured and named as  $Q_{in1}$ . Then the tube is removed and the input power of metering box is measured again and named as  $Q_{in2}$ . The tube heat loss can be calculated by:

$$Q_{thl} = Q_{in1} - Q_{in2} \quad (3-9)$$

Where,  $Q_{in1}$  is the input power of heaters when a single-glazed window is put in the opening of sample frame with installing the insulated tube, W;  $Q_{in2}$  is the input power of heaters when a single-glazed window is put in the opening of sample frame without installing the tube, W.

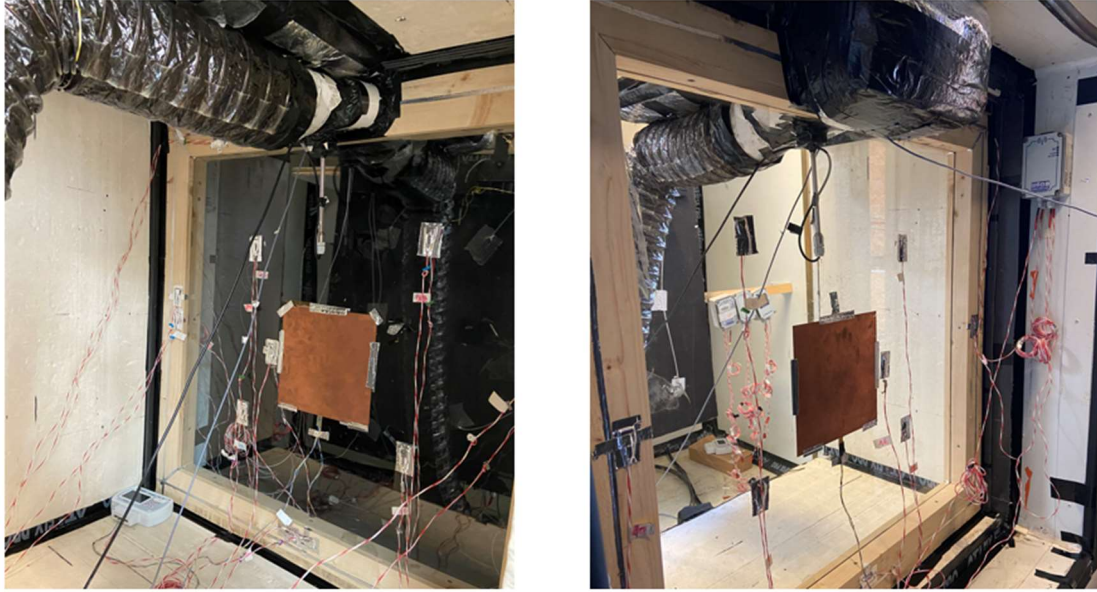


Figure 3-13 Picture of the single-glazed window with a tube

The U-value of closed-air double window is calculated as Eq. (3-10):

$$U = \frac{Q_{in} - Q_{ex} - Q_{sfl}}{A \cdot \Delta T_{MB-CB}} \quad (3-10)$$

The U-value of supply-air double window is calculated as Eq. (3-11), Eq. (3-12) and Eq. (3-13):

$$U_{loss} = \frac{Q_{in} - Q_{ex} - Q_{sfl} - Q_{thl}}{A \cdot \Delta T_{MB-CB}} \quad (3-11)$$

$$U_{use} = \frac{A_t \cdot v_{il} \cdot \rho \cdot C \cdot \Delta T_{il-ol}}{A \cdot \Delta T_{MB-CB}} \quad (3-12)$$

$$U_{eq} = U_{loss} - U_{use} \quad (3-13)$$

Where,  $A_t$  is the tube opening area, m<sup>2</sup>;  $\Delta T_{il-ol}$  is the temperature difference between window inlet and outlet air temperature, °C.

### (3) Description of the tested window configurations

Three supply-air double windows with different configurations (as shown in Figure 3-14) were tested: VW1 (composed of two single-glazed windows), VW2 (composed of a single-

glazed window and a clear double-glazed window) and VW3 (composed of a single-glazed window and a Low-E double-glazed window).

Also, three closed-air double windows (as shown in Figure 3-14) were tested based on the adjusted calibration procedure: DW1 (composed of two single-glazed windows), DW2 (composed of a single-glazed window and a clear double-glazed window), DW3 (composed of a single-glazed window and a Low-E double-glazed window). It should be mentioned that, in the test of closed-air double windows, the air velocity in the cavity is assumed as 0 as the air movement is induced by the natural convection and it is weak enough to be neglected. So, before identifying the sample flanking loss, only the air temperature of cavity needs to be measured.

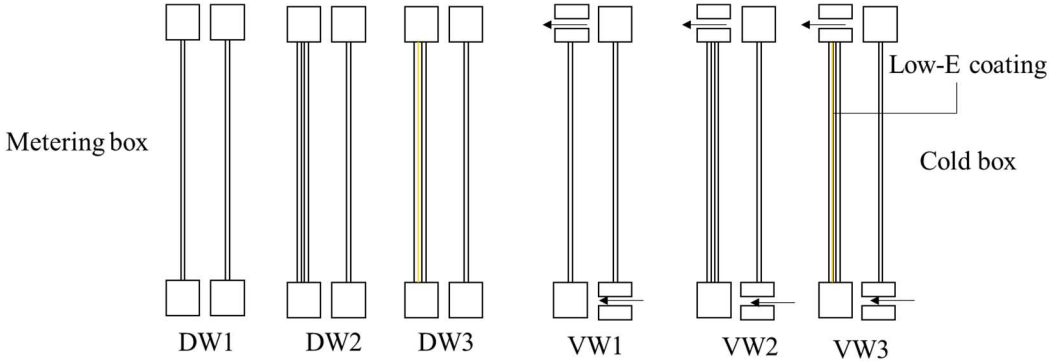


Figure 3-14 Configurations of closed-air double windows and supply-air double windows

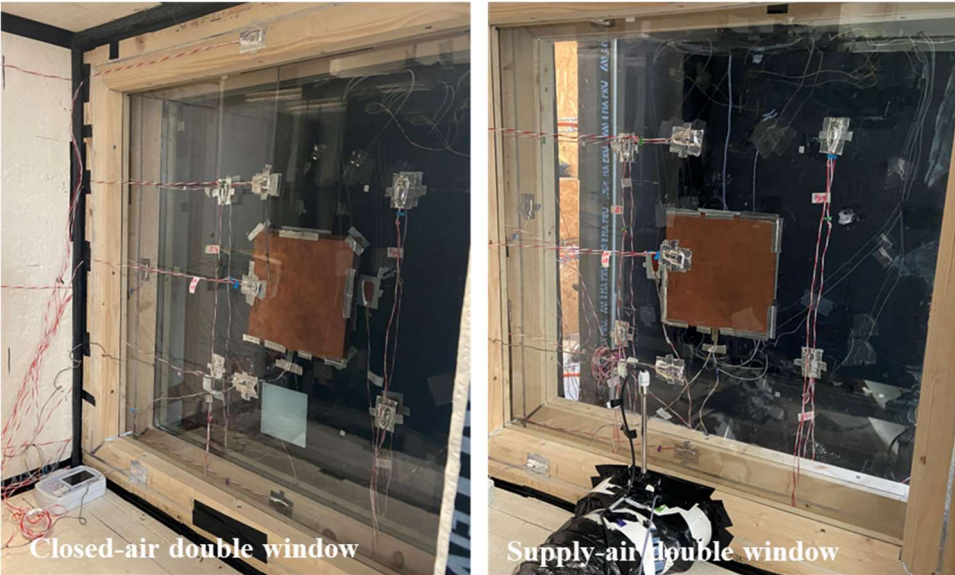


Figure 3-15 Picture of testing a closed-air double window and a supply-air double window



### 3.2.4 Uncertainty Analysis

Different variables such as temperature, heat flux and input energy are measured with above-mentioned instruments during the tests. The difference between the measured value and the true value is defined as measurement error and it causes uncertainties in variables. To assess the effect of uncertainty in individual variable on the uncertainties in the final results, the uncertainty analysis is needed by using the law of propagation. Specifically, assume  $f$  is a function of independent variables  $x_1, x_2, \dots, x_n$ .

$$f = f(x_1, x_2, \dots, x_n) \quad (3-14)$$

The uncertainty of  $f$  can be calculated by the following equation:

$$u_f = \sqrt{\left(\frac{\partial f}{\partial x_1} u_1\right)^2 + \left(\frac{\partial f}{\partial x_2} u_2\right)^2 + \dots + \left(\frac{\partial f}{\partial x_n} u_n\right)^2} \quad (3-15)$$

Or

$$\frac{u_f}{f} = \sqrt{\left(\frac{\partial f}{\partial x_1} \frac{u_1}{f}\right)^2 + \left(\frac{\partial f}{\partial x_2} \frac{u_2}{f}\right)^2 + \dots + \left(\frac{\partial f}{\partial x_n} \frac{u_n}{f}\right)^2} \quad (3-16)$$

Where,  $u_1, u_2, \dots, u_n$  are the uncertainties of variables  $x_1, x_2, \dots, x_n$ .

### 3.3 Experimental results

#### 3.3.1 Calibration results

Based on the calibration tests, the effects of air temperature difference and air velocity on sample flanking loss are investigated. Also, the influences of tube inlet air temperature and velocity on the tube heat loss are analyzed.

##### (1) Sample flanking loss

During the tests, the air velocity in hot side was controlled at 0.1 m/s, the air velocity in cold side was controlled at 0 and 1.5 m/s, respectively. The temperature in hot side was set at 30 °C, and the temperature of cold side was changed in the range of 0.9-10.3 °C.

The measured sample flanking losses are shown in Figure 3-16. From this figure, it can be observed that the calibrated sample flanking loss increases with increasing the air temperature difference between hot and cold sides. This is due to the fact that an increased air temperature difference can result in an increase in the total heat flux from metering box to cold box. In addition, it can be found that the calibrated sample flanking loss is larger as the air velocity in cold side is larger. This is because the convective heat exchange between the tested sample and cold side is enhanced.

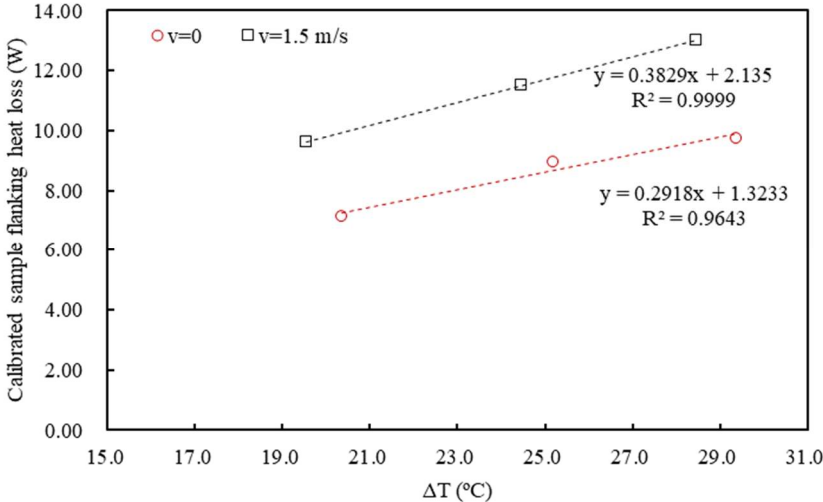


Figure 3-16 Calibrated heat losses under different air temperature difference and air velocities

## (2) Tube heat loss

To analyze the influence of tube inlet air temperature on the tube heat loss, the tube inlet air velocity was controlled at around 0.3 m/s, the inlet air temperature was changed from 1.3 °C to 13.0 °C. The correlation between tube heat loss and tube inlet air temperature is presented in Figure 3-17. It can be found that the tube heat loss has a linear negative correlation with the tube inlet air temperature. When the inlet air temperature of tube is lower, the tube heat loss is higher. This is reasonable as a lower inlet air temperature leads to a larger temperature gradient between the inside and outside of the tube. To further analyze the influence of tube inlet air velocity on the tube heat loss, the tube inlet air temperature was controlled at 4.2 °C, the inlet air velocity was changed from around 0.3 m/s to 0.9 m/s. The tube heat losses measured with different inlet air velocities are illustrated in Figure 3-17. As shown in figure, the influence of air velocity on the tube heat loss can be neglected when the air velocity is in the range of 0.3-0.9 m/s.

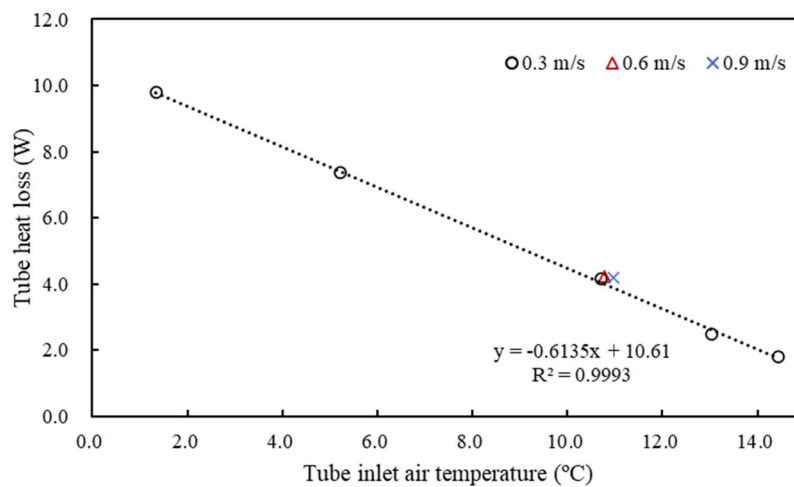


Figure 3-17 Tube heat losses under different tube inlet air temperatures and velocities

## (3) Convective heat transfer coefficient

The calculated convective heat transfer coefficients are presented in Figure 3-18. It can be seen that the convective heat transfer coefficient in cold side is larger than that in hot side due to the fact that the air velocity in cold side (1.5 m/s) is larger than the air velocity in hot side (0.1 m/s).

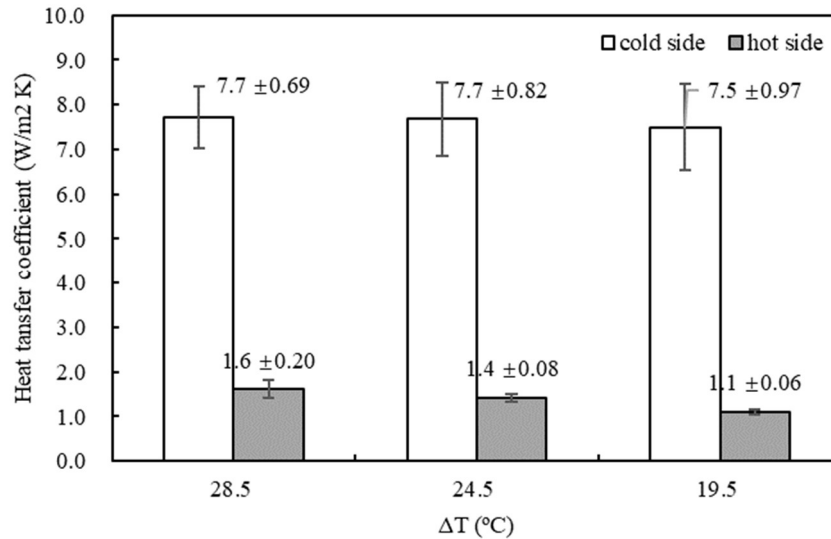


Figure 3-18 Convective heat transfer coefficients in hot and cold sides

### 3.3.2 U-values of different window configurations

#### (1) Single windows

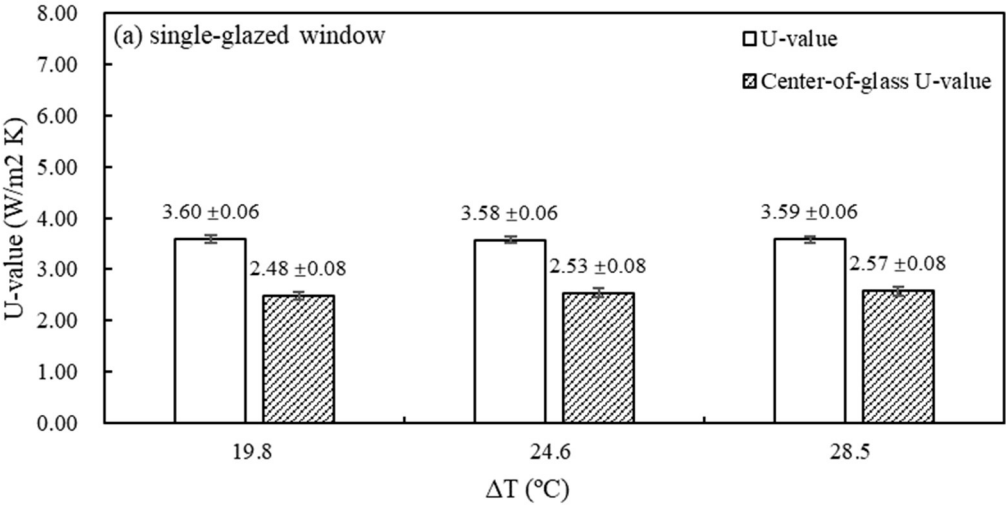
During the tests of single windows, the air temperature of metering box was set as 30 °C, and the air temperature of cold box was varied from 1.5 °C to 10.2 °C. The air velocity in hot and cold sides were set as 0.1 m/s and 1.5 m/s, respectively. The calculated heat transferred through the tested window ( $Q_w$ ) and the measured heat flux ( $q_F$ ) through center-of-glass are shown in Table 3-2.

Table 3-2 Detailed testing reports of the single-glazed window, clear double-glazed window and Low-E double-glazed window

Configuration	$T_{MB}$ [°C]	$T_{CB}$ [°C]	$Q_w$ [W]	$q_F$ [W/(m <sup>2</sup> K)]
Single-glazed window	30 ± 0.15	1.5 ± 0.15	80.7 ± 1.11	73.0 ± 2.19
	30 ± 0.15	5.4 ± 0.15	69.5 ± 0.97	62.3 ± 1.87
	30 ± 0.15	10.2 ± 0.15	56.3 ± 0.80	49.1 ± 1.47
Clear double-glazed window	30 ± 0.15	1.7 ± 0.15	48.3 ± 0.83	49.7 ± 1.49
	30 ± 0.15	5.5 ± 0.15	42.0 ± 0.73	42.7 ± 1.28
	30 ± 0.15	10.2 ± 0.15	34.6 ± 0.62	34.5 ± 1.03
Low-E double-glazed window	30 ± 0.15	1.5 ± 0.15	35.9 ± 0.74	30.2 ± 0.91
	30 ± 0.15	5.2 ± 0.15	29.8 ± 0.64	25.6 ± 0.77
	30 ± 0.15	10.2 ± 0.15	22.9 ± 0.53	20.4 ± 0.61

Figure 3-19(a)-(c) show the window total U-value and center-of-glass U-value of the tested single-glazed window, clear double-glazed window and Low-E double-glazed window, under different air temperature difference between hot and cold sides. As shown in Figure 3-19(a), the U-value of the single-glazed window is around 3.60 W/(m<sup>2</sup> K). As shown in Figure 3-19(b), the U-value of the clear double-glazed window slightly decreases from 2.30 W/(m<sup>2</sup> K) to 2.17 W/(m<sup>2</sup> K) by increasing the ΔT from 19.5 °C to 28.5 °C. A possible reason is that when the ΔT is lower the moisture content of wooden frame is higher and thus its thermal conductivity is lower. Among the tested three windows, the Low-E double-glazed window has the lowest U-value. As shown in Figure 3-19(c), the U-value of double-glazed Low-E window slightly increases from 1.46 W/(m<sup>2</sup> K) to 1.59 W/(m<sup>2</sup> K) by increasing the ΔT from 19.5 °C to 28.5 °C. This is probably due to the fact that the radiation heat transfer is enhanced as the temperature of cold side decreases.

In addition, it could be observed from Figure 3-19. that the window U-value is always higher than the center-of-glass U-value. When the temperature difference between hot and cold sides increases from 19.5 °C to 28.5 °C, the deviations between the U-value and the center-of-glass U-value are 31.1%, 29.3% and 28.4% for the single-glazed window, 21.6%, 19.8% and 19.0% for the clear double-glazed window, 29.5%, 32.7% and 33.3% for the double-glazed Low-E window. It indicates that the building simulations rely on the center-of-glazing values might lead to significant errors.



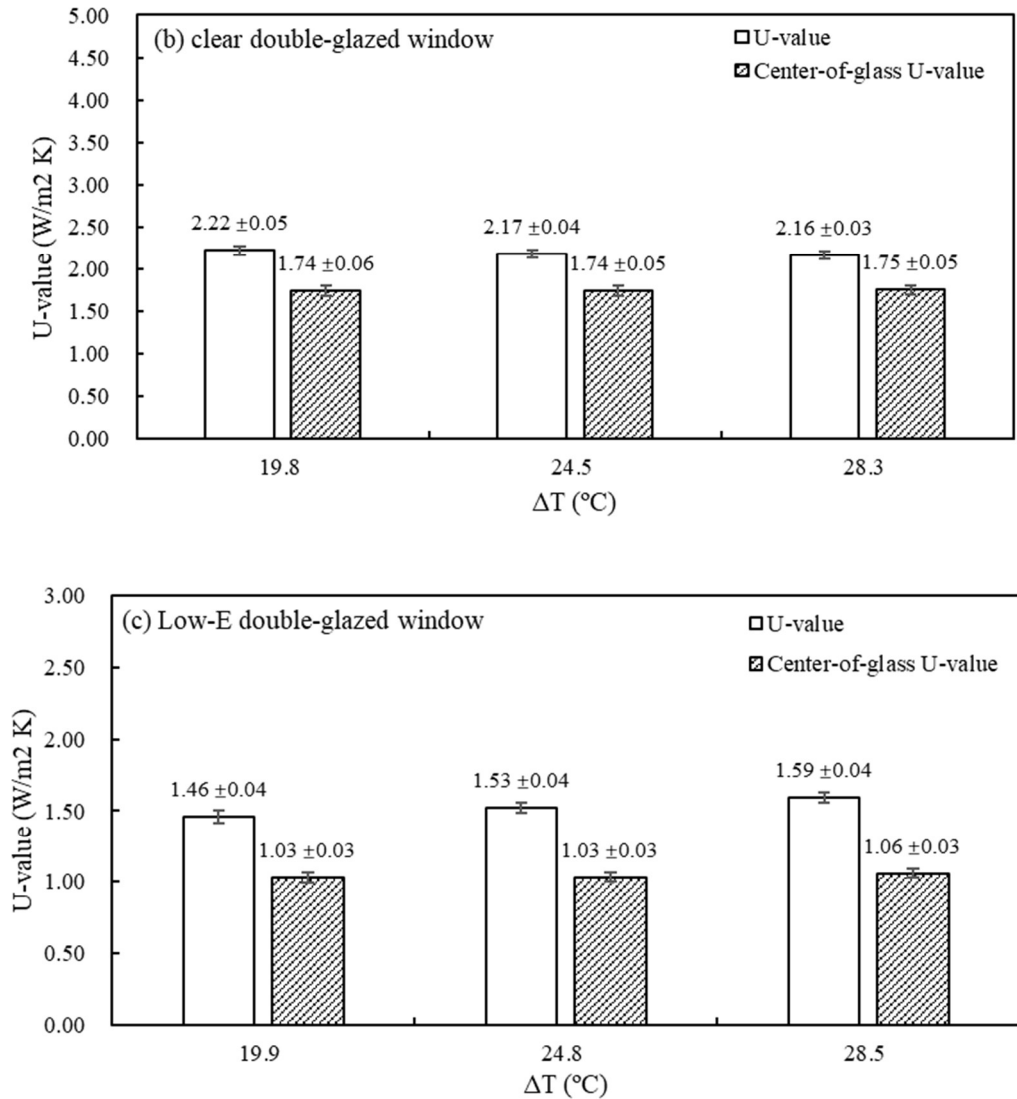


Figure 3-19 U-values of the single-glazed window, clear double-glazed window and Low-E double-glazed window

## (2) Closed-air double windows

During the experiments of closed-air double windows, the air temperatures of hot and cold sides were controlled as shown in Table 3-3. The air velocities in hot and cold sides were controlled at 0.1 and 1.5 m/s, respectively. The experimental data shows that the average air temperatures of cavity between two windows are 19.0 °C, 17.5 °C and 15.9 °C for DW1, DW2 and DW3, respectively.

Table 3-3 Detailed testing reports of the DW1, DW2 and DW3

Configuration	$T_{MB}$	$T_{CB}$	$Q_w$	$q_F$
---------------	----------	----------	-------	-------

	[°C]	[°C]	[W]	[W/(m <sup>2</sup> K)]
DW1	30±0.15	10.7±0.15	30.1±0.44	20.8±0.62
DW2	30±0.15	10.6±0.15	22.9±0.38	20.0±0.60
DW3	30±0.15	10.2±0.15	17.7±0.23	14.8±0.44

The U-values and center-of-glass U-values of closed-air double windows with a 95 mm gap width are shown in Figure 3-20. As shown in this figure, among the tested three closed-air double windows, the DW3 has the lowest U-value of 0.75 W/(m<sup>2</sup> K). This is expected as the DW3 is retrofitted by adding a Low-E double-glazed window which has lower U-value than the single-glazed window and clear double-glazed window.

Compared to the single-glazed window, the U-values of closed-air double windows are reduced by 45.0%, 58.3% and 68.6% when the secondary window is adopting the single-glazed window, the clear double-glazed window and the Low-E double-glazed window, respectively. This indicates that adding a secondary window can significantly improve the window thermal performance and it has a large potential to reduce building energy losses.

Also, it can be observed from Figure 3-20 that the window U-value is always higher than the center-of-glass U-value. The deviations between window U-value and center-of-glass U-value are 45.5% for the DW1, 30.7% for the DW2, 33.6% for the DW3.

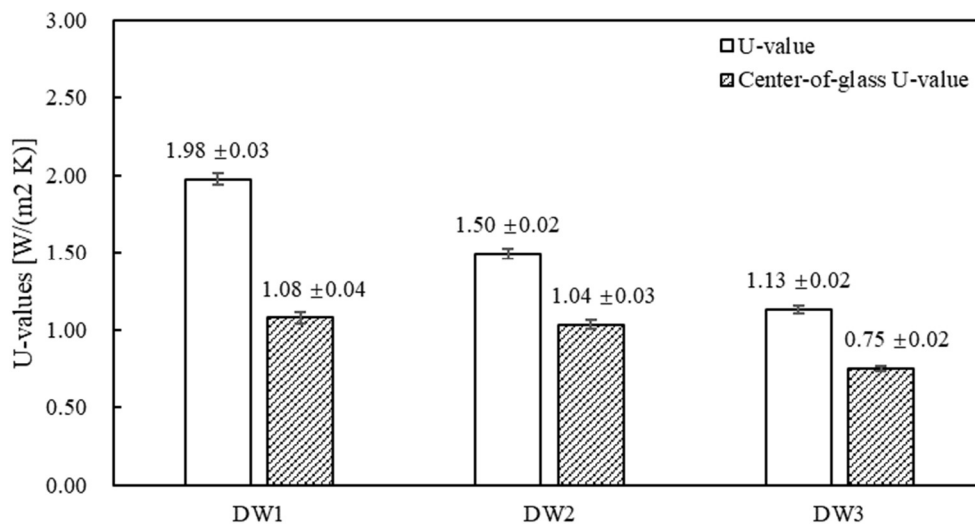


Figure 3-20 U-values of closed-air double windows with a 95 mm gap width

To investigate the impact of gap width on U-values, the gap width was changed from 25 mm to 95 mm. As shown in Figure 3-21, the impact of gap width is insignificant for the closed-air double windows.

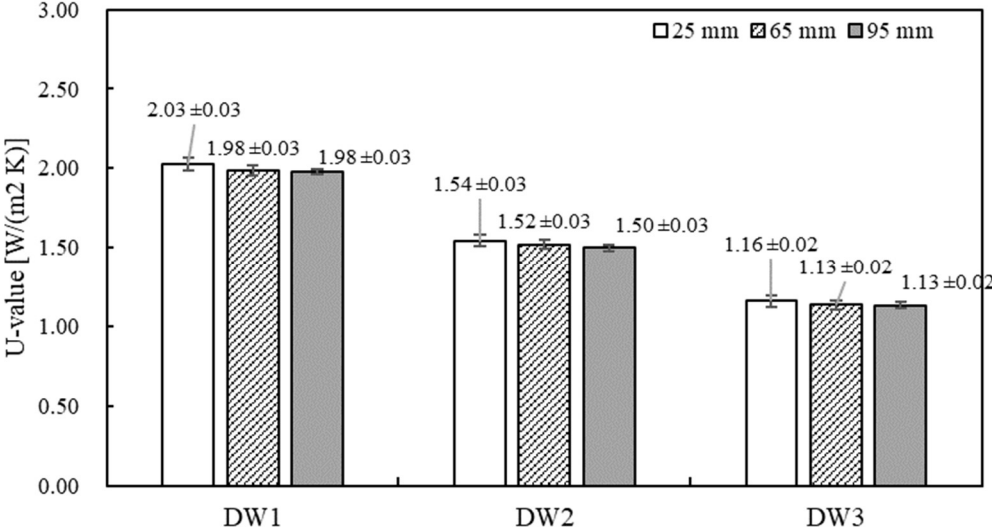


Figure 3-21 U-values of closed-air double windows with different gap widths

(3) Supply-air double windows

This subsection presents the thermal performance of supply-air double windows with a 95 mm gap width. During the tests, the air temperatures of hot and cold sides were controlled as shown in Table 3-4. The air velocities in hot and cold sides were controlled at around 0.1 and 1.5 m/s, respectively. The window inlet air velocity was controlled at 0.3 m/s. Based on the monitored data, the average air temperatures of cavity are calculated and they are 11.2 °C, 9.6 °C and 8.6 °C for the VW1, VW2 and VW3, respectively. The calculated heat transferred through the window and the measured heat flux through the center of glass are listed in Table 3-4.

Table 3-4 Detailed testing reports of the VW1, VW2 and VW3

Configuration	$T_{MB}$ [°C]	$T_{CB}$ [°C]	$T_{it}$ [°C]	$T_{ot}$ [°C]	$Q_w$ [W]	$q_F$ [W/(m² K)]
VW1	30 ± 0.15	6.3 ± 0.15	5.9 ± 0.15	15.3 ± 0.15	52.2 ± 0.87	46.6 ± 1.40
VW2	30 ± 0.15	6.1 ± 0.15	5.8 ± 0.15	13.1 ± 0.15	34.4 ± 0.87	33.7 ± 1.01
VW3	30 ± 0.15	6.0 ± 0.15	5.6 ± 0.15	11.4 ± 0.15	27.4 ± 0.93	23.4 ± 0.70



Figure 3-22 show the U-values of supply-air double windows. As shown in this figure, among three tested window configurations, the VW1 has the highest  $U_{loss}$  value and the highest  $U_{use}$  value. This is because the secondary window of VW1 has the lowest U-value and thus more heat enters from the hot side to the airflow channel to preheat the supplied air. In terms of  $U_{eq}$  value, the VWs has the lowest value. In this view, the Low-E double-glazed window is more suggested in the window retrofitting work.

Compared to the single-glazed window, the U-values of supply-air double windows are reduced by 64.7%, 81.9% and 85.3% when the secondary window is adopting the single-glazed window, the clear double-glazed window and the Low-E double-glazed window, respectively. Compared to the closed-air double windows, supply-air double windows can achieve 35.8%-56.7% reductions on U-values. This indicates that supply-air double windows have a larger application potential than closed-air double windows in window renovation works.

It also can be observed from Figure 3-22 that the center-of-glass U-value is always smaller than the  $U_{loss}$  value. The deviations between the  $U_{loss}$  value and the center-of-glass U-value are 29.6% for VW1, 22.9% for VW2, and 33.1% for VW3.

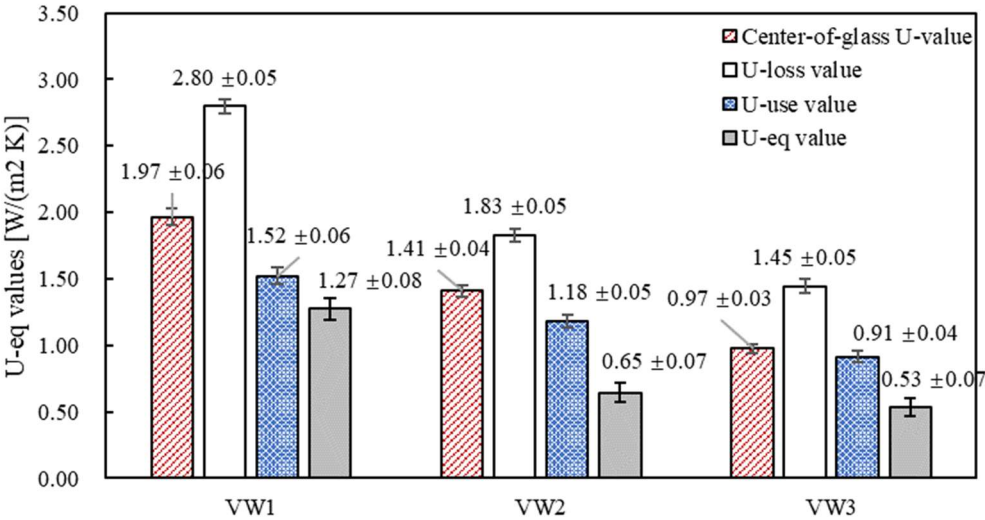


Figure 3-22 U-values of supply-air double windows with a 95 mm gap width

Also, the effect of inlet air velocity on the U-values of VW3 is further investigated by varying the inlet air velocity from 0.3 m/s to 0.9 m/s. The results are presented in Figure 3-23.

As illustrated in this figure, the  $U_{loss}$  value and  $U_{use}$  value are larger for a larger inlet air velocity. The current result cannot reflect the impact of inlet air velocity on the  $U_{eq}$  value. More accurate measurement instruments are required in future studies.

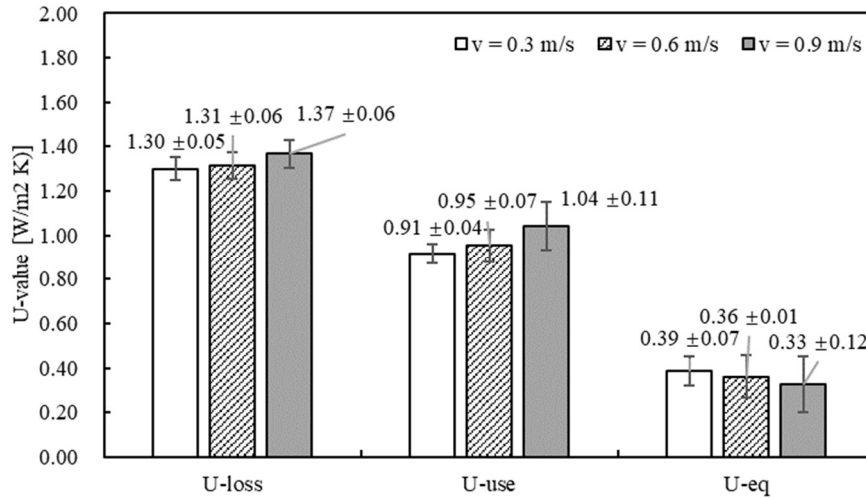


Figure 3-23 U-values of the VW3 with different inlet air velocities

### 3.3.3 U-value with taking sample flanking loss into consideration

For the purpose of simply comparing different window configurations, the sample flanking loss is taken into consideration of U-value. The U-value considering the sample flanking loss is denoted as  $U'$  value and it can be expressed as the following formulas.

For single windows and closed-air double windows,

$$U' = \frac{Q_{in} - Q_{ex}}{A \cdot \delta T} \quad (3-17)$$

For supply-air double windows,

$$U'_{loss} = \frac{Q_{in} - Q_{ex} - Q_{thl}}{A \cdot \delta T} \quad (3-18)$$

$$U'_{eq} = U'_{loss} - U_{use} \quad (3-19)$$

The heat flow transferred through the tested window are listed in Table 3-5.

Table 3-5 Detailed testing reports by taking the sample flanking loss into consideration

Configuration	$T_{MB}$ [°C]	$T_{CB}$ [°C]	$Q$ [W]
Single-glazed window	30±0.15	10.2±0.15	66.0±0.73
Clear double-glazed window	30±0.15	10.2±0.15	44.3±0.49
Low-E double-glazed window	30±0.15	10.1±0.15	32.7±0.39
DW1	30±0.15	10.7±0.15	34.7±0.42
DW2	30±0.15	10.6±0.15	27.8±0.33
DW3	30±0.15	10.2±0.15	23.1±0.16
VW1	30±0.15	10.7±0.15	49.2±0.64
VW2	30±0.15	10.6±0.15	36.1±0.61
VW3	30±0.15	10.5±0.15	29.4±0.68

The  $U'$  values of the single-glazed window, clear double-glazed window, Low-E double-glazed window, DW1, DW2 and DW3 and the  $U'_{eq}$  values of VW1, VW2 and VW3 are illustrated in Figure 3-24. As shown in figure, compared to the single-glazed window, the  $U'$  values of closed-air double windows are reduced by 46.2%, 56.9% and 65.0% when the secondary window is using the single-glazed window, the clear double-glazed window and the Low-E double-glazed window, respectively. By comparing the  $U'$  of the single-glazed window with the  $U'_{eq}$  values of the VW1, VW2 and VW3, it can be found that renovating the single-glazed window into the VW1, VW2 and VW3 can reduce the U-value by 55.9%, 69.7% and 73.4%, respectively.

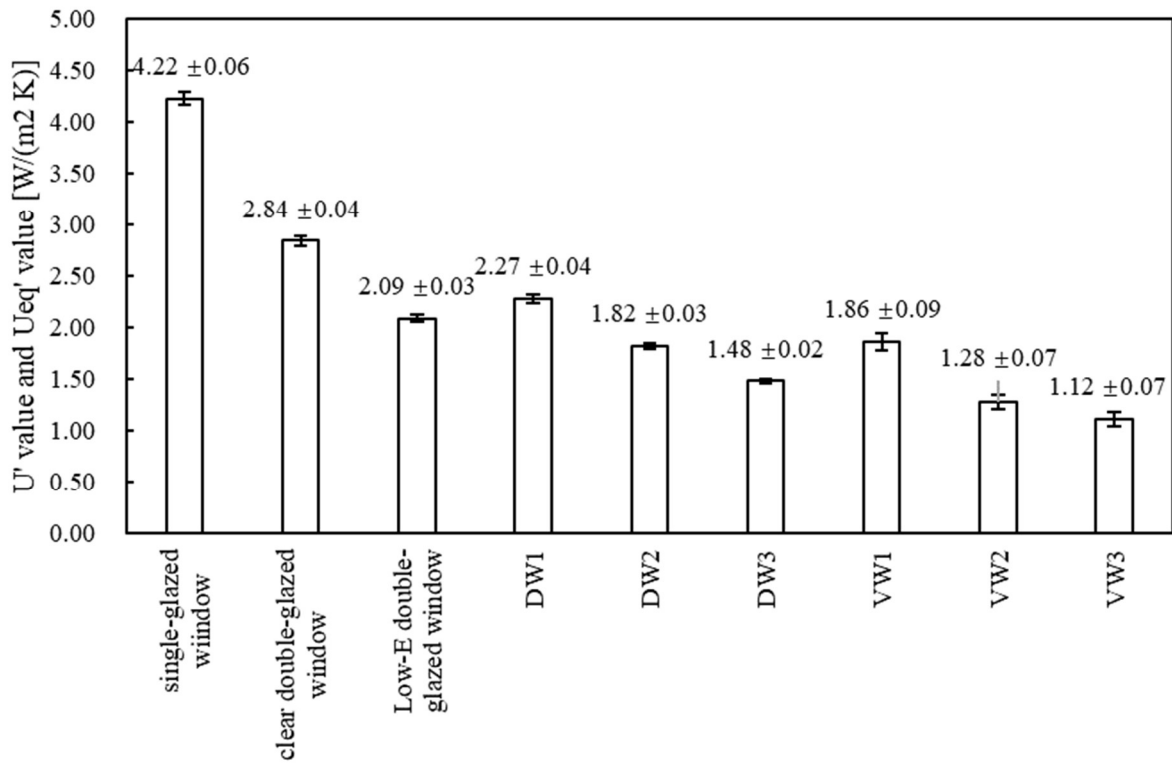


Figure 3-24 U-values with taking the sample flanking loss into consideration

### 3.4 Conclusions

The conventional GHB method is not adapted for testing supply-air double windows due to the exist of the airflow channel. In this study, an adjusted and highly improved GHB method is proposed. Based on the conventional GHB method and adjusted GHB method, nine window configurations are compared to see the potential of window renovation by adding a secondary window. Also, the center-of-glazing U-value and the total U-value are compared. The results are summarized as follows:

(1) Compared to the single-glazed window, the U-values of closed-air double windows are reduced by 45.0%, 58.3% and 68.6% by adding the single-glazed window, clear double-glazed window and Low-E double-glazed window as a secondary window, respectively.

(2) Compared to the single-glazed window, the U-values of supply-air double windows are reduced by 64.7%, 81.9% and 85.3% by adding the single-glazed window, clear double-glazed window and Low-E double-glazed window as a secondary window, respectively. The supply-air double windows have a larger potential in reducing the U-value than the closed-air double windows.

(3) The deviations between center-of-glass U-value and total U-value are in the range of 19.0%-45.5% for different window configurations. This indicates that the use of center-of-glass U-value in building code will lead to significant errors.

## **4 Parametric and Sensitivity Analysis for Supply-air Double windows based on CFD simulations**

## 4.1 Introduction

In previous studies, the influence of different window design parameters and boundary conditions on the U-values of supply-air windows were studied based on experiments or numerical simulations. Wright carried out simulations to investigate U-values and  $U_{eq}$  values of eleven window configurations composed of different inner and outer glazing units with or without supply air flow [9]. The airflow channel was 15 mm. It was found that, the supply air-flow utilization could lead to 31–58% reduction of U-value. Also, the author noted that the low-e coating could better exert its benefit when it was placed on the surface of the inner glazing that faces the airflow channel. A similar finding was reported in [110] that the  $U_{eq}$  value was almost reduced by 50% by changing the position of low-e coating. Another finding in [110] was that an increase in the supply air flow rate from 5.6 l/s to 14 l/s in a 30 mm cavity led to a decrease in the  $U_{eq}$  value from 1.12 to 0.67 W/(m<sup>2</sup> K). In a later study performed by Southall and McEvoy [27], the correlation between the window area and  $U_{eq}$  value was calculated based on CFD simulations. Carlos et al. [15] investigated U-values based on in-situ experiments and numerical analysis. They found that compared to the supply-air double window with an inner single-glazed unit, the window with an inner double-glazed unit had a lower  $U_{loss}$  value, a lower  $U_{use}$  value and a lower  $U_{eq}$  value. When the air flow rate increased, the  $U_{loss}$  value and  $U_{use}$  value increased, while the  $U_{eq}$  value decreased. They also found that when the air temperature difference between cold and hot sides increased, the  $U_{loss}$  value and  $U_{use}$  value increased, while the  $U_{eq}$  value decreased.

Although some parametric analyses have been performed for U-values of supply-air windows, there is no sensitivity analysis that compares the effect of different parameters on the U-values. To address this problem, the aim of this chapter is to propose a comprehensive parametric study by simultaneously considering the impact of window structure as a prime influencing factor and the effects of geometry/thermal/optical parameters of internal/external windows and boundary conditional parameters on U-values. The parametric study is based on CFD simulations. In total, 154 numerical scenarios are simulated.

This chapter includes five sections: Section 4.1 summarizes the existing parametric studies on the U-values of supply-air window. Section 4.2 presents the procedure of CFD simulation and evaluation of the established model. Section 4.3 and 4.4 provide the results of parametric studies and sensitivity analysis. Section 4.5 concludes this chapter.



## 4.2 CFD model establishment and evaluation

CFD models for three supply-air double windows (i.e, VW1, VW2 and VW3) were established using commercial CFD software ANSYS 19.0. The procedure of establishing a CFD model is shown in Figure 4-1. For sake of simplicity, the supply-air double window which is composed of two single-glazed windows is taken as an example to describe details of CFD establishment and evaluation. The simulations were runed on a personal computer with a Intel(R) Core(TM) i7-8565U CPU and 8 GB memory.

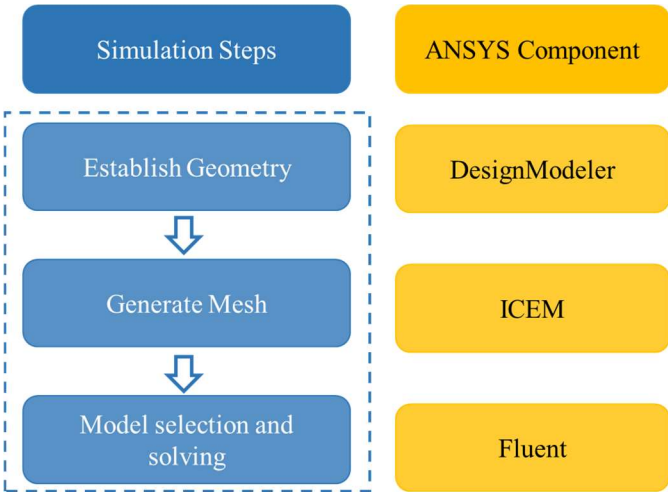
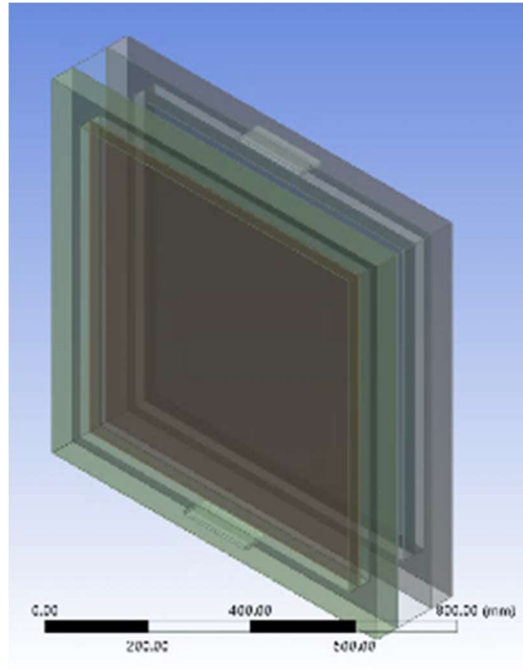


Figure 4-1 Simulation steps and ANSYS components

### 4.2.1 Model geometry and boundary conditions setup

Figure 4-2 shows the model geometry. The window size is 0.888 m × 0.888 m and the gap width between two windows is 95 mm.



*Figure 4-2 Model geometry*

Physical properties of glazing and window frame are listed in Table 4-1. The air density is set as a function of temperature using the Boussinesq approximation method.

*Table 4-1 Physical properties of glass and frame*

<b>Property</b>	<b>Glass</b>	<b>Frame</b>
Density [kg/m <sup>3</sup> ]	2500	450
Specific heat [J/(kg K)]	750	1880
Thermal conductivity [W/(m K)]	1	0.13
Emissivity	0.8	0.9

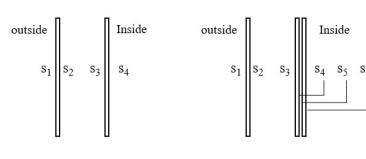
In the model evaluation procedure, the boundary conditions are set as the same as the experimental conditions as shown in Table 4-2. The lateral walls are considered adiabatic.

*Table 4-2 Boundary conditions*

<b>Boundary conditions</b>	<b>Value</b>
Air temperature in hot side [°C]	30
Air temperature in cold side [°C]	6.3
Inlet air temperature [°C]	5.9
Convective heat transfer coefficient in hot side [W/(m <sup>2</sup> K)]	1.6
Convective heat transfer coefficient in cold side [W/(m <sup>2</sup> K)]	7.8
Inlet/outlet air mass flow rate [kg/s]	0.003

In the latter parametric studies, the window configuration parameter and boundary conditional parameters are summarized in Table 4-3.

Table 4-3 Window configuration parameters and boundary conditional parameters

	Variables	Other parameters
#1	Window size [H(m) × W(m)]: 0.888×0.888; 0.888×1.332; 0.888×1.776; 0.888×2.220; 0.888×2.664; 0.888×3.108;	$T_{int} = 20\text{ °C};$ $T_{ext} = 5\text{ °C};$ $T_{il} = 5\text{ °C};$ $h_{c,int} = 7.7\text{ W/(m}^2\text{ K)}$ $h_{c,ext} = 25\text{ W/(m}^2\text{ K)}$ $\dot{m} = 0.006\text{ kg/s}$ $k_{f,int} = k_{f,ext} = 0.13\text{ W/(m K)}$
#2	Thermal conductivity of external window frame, $k_{f,ext}$ : 0.1; 0.2; 0.3; 0.4; 0.5 [W/(m K)]	Size: 0.888 m×0.888 m $T_{int} = 20\text{ °C};$ $T_{ext} = 5\text{ °C};$ $T_{il} = 5\text{ °C};$ $h_{c,int} = 7.7\text{ W/(m}^2\text{ K)}$ $h_{c,ext} = 25\text{ W/(m}^2\text{ K)}$ $\dot{m} = 0.006\text{ kg/s}$ $k_{f,int} = 0.13\text{ W/(m K)}$
#3	Thermal conductivity of internal window frame, $k_{f,int}$ : 0.1; 0.2; 0.3; 0.4; 0.5 [W/(m K)]	Size: 0.888 m×0.888 m $T_{int} = 20\text{ °C};$ $T_{ext} = 5\text{ °C};$ $T_{il} = 5\text{ °C};$ $h_{c,int} = 7.7\text{ W/(m}^2\text{ K)}$ $h_{c,ext} = 25\text{ W/(m}^2\text{ K)}$ $\dot{m} = 0.003\text{ kg/s}$ $k_{f,ext} = 0.13\text{ W/(m K)}$
#4	mass flow rate, $\dot{m}$ : 0.001; 0.002; 0.003; 0.004; 0.005; 0.006; 0.007 [kg/s]	Size: 0.888 m×0.888 m $T_{int} = 20\text{ °C};$ $T_{ext} = 5\text{ °C};$ $T_{il} = 5\text{ °C};$ $h_{c,int} = 7.7\text{ W/(m}^2\text{ K)}$ $h_{c,ext} = 25\text{ W/(m}^2\text{ K)}$ $k_{f,int} = k_{f,ext} = 0.13\text{ W/(m K)}$
#5	Position of Low-e Coating Configuration I: surface 1, 2, 3, 4 Configuration II: 1, 2, 3, 4, 5, 6	Size: 0.888 m×0.888 m $T_{int} = 20\text{ °C};$ $T_{ext} = 5\text{ °C};$ $T_{il} = 5\text{ °C};$ $h_{c,int} = 7.7\text{ W/(m}^2\text{ K)}$ $h_{c,ext} = 25\text{ W/(m}^2\text{ K)}$ $\dot{m} = 0.003\text{ kg/s}$ $k_{f,int} = k_{f,ext} = 0.13\text{ W/(m K)}$
	 <p>Configuration I: A double-pane window with surfaces labeled s1, s2, s3, and s4. The left side is labeled 'outside' and the right side is labeled 'Inside'. Configuration II: A triple-pane window with surfaces labeled s1, s2, s3, s4, s5, and s6. The left side is labeled 'outside' and the right side is labeled 'Inside'.</p>	
#6	Value of emissivity: 0.03; 0.1; 0.2; 0.3; 0.4; 0.5	Size: 0.888 m×0.888 m $T_{int} = 20\text{ °C};$

---

		$T_{ext} = 5 \text{ }^\circ\text{C};$ $T_{il} = 5 \text{ }^\circ\text{C};$ $h_{c,int} = 7.7 \text{ W}/(\text{m}^2 \text{ K})$ $h_{c,ext} = 25 \text{ W}/(\text{m}^2 \text{ K})$ $\dot{m} = 0.006 \text{ kg/s}$ $k_{f,int} = k_{f,ext} = 0.13 \text{ W}/(\text{m K})$
#7	Inside convection heat transfer coefficient, $h_{c,int}$ : 1; 3; 5; 7.7; 10 [W/(m <sup>2</sup> K)]	Size: 0.888 m×0.888 m $T_{int} = 20 \text{ }^\circ\text{C};$ $T_{ext} = 5 \text{ }^\circ\text{C};$ $T_{il} = 5 \text{ }^\circ\text{C};$ $h_{c,ext} = 25 \text{ W}/(\text{m}^2 \text{ K})$ $\dot{m} = 0.003 \text{ kg/s}$ $k_{f,int} = k_{f,ext} = 0.13 \text{ W}/(\text{m K})$
#8	Outside Convection heat transfer coefficient, $h_{c,ext}$ : 5; 10; 15; 20; 25 [W/(m <sup>2</sup> K)]	Size: 0.888 m×0.888 m $T_{int} = 20 \text{ }^\circ\text{C};$ $T_{ext} = 5 \text{ }^\circ\text{C};$ $T_{il} = 5 \text{ }^\circ\text{C};$ $h_{c,int} = 7.7 \text{ W}/(\text{m}^2 \text{ K})$ $\dot{m} = 0.003 \text{ kg/s}$ $k_{f,int} = k_{f,ext} = 0.13 \text{ W}/(\text{m K})$
#9	Outdoor air temperature, $T_{ext}$ : 0; 5; 10; 15 [°C]	Size: 0.888 m×0.888 m $T_{int} = 20 \text{ }^\circ\text{C};$ $T_{il} = T_{ext};$ $h_{c,int} = 7.7 \text{ W}/(\text{m}^2 \text{ K})$ $h_{c,ext} = 25 \text{ W}/(\text{m}^2 \text{ K})$ $\dot{m} = 0.003 \text{ kg/s}$ $k_{f,int} = k_{f,ext} = 0.13 \text{ W}/(\text{m K})$
#10	Indoor air temperature, $T_{int}$ : 10; 15; 20; 25 [°C]	Size: 0.888 m×0.888 m $T_{ext} = 5 \text{ }^\circ\text{C};$ $T_{il} = 5 \text{ }^\circ\text{C};$ $h_{c,int} = 7.7 \text{ W}/(\text{m}^2 \text{ K})$ $h_{c,ext} = 25 \text{ W}/(\text{m}^2 \text{ K})$ $\dot{m} = 0.003 \text{ kg/s}$ $k_{f,int} = k_{f,ext} = 0.13 \text{ W}/(\text{m K})$

---

#### 4.2.2 Grid generation and grid independence analysis

The ANSYS ICEM CFD, which is a flexible grid-generation tool, is applied to generate grids in unstructured hexahedral format. Considering that the gradients of air temperatures and air velocities are significant near the boundary, concentrated grid is utilized to ensure the accuracy. The schematic of grid is shown in Figure 4-3.

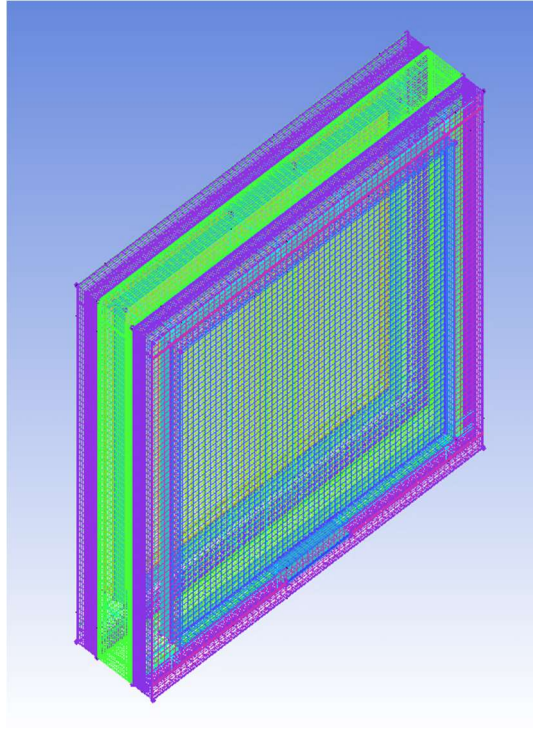


*Figure 4-3 Schematic of grid generation*

The computational time of CFD simulation is mainly determined by the size of grids. A smaller size of grids indicates a larger number of grids which leads to a longer computational time. Furthermore, the size of grids is a key parameter that influences the CFD result accuracy. It is therefore necessary to perform the grid independence analysis. The grid independence analysis was conducted for different grid numbers: 254,400 (grid #1), 322,104 (grid #2), 438,334 (grid #3) and 770,172 (grid #4). The simulated outlet air temperatures are 15.1 °C, 15.3 °C, 15.2 °C and 15.3 °C for the grid #1, #2, #3 and #4. Also, the temperature distributions along the mid-line of the cavity for different grids are presented, as shown in Figure 4-4. From this figure, it can be observed that the simulation deviations between grid #2, grid #3 and grid #4 are minor. To balance the computational time and simulation results the grid #2 is adopted.

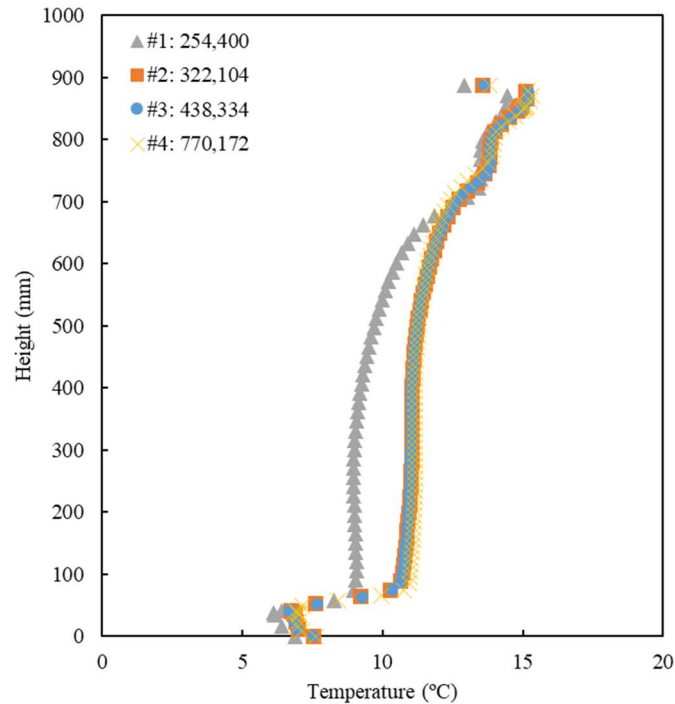


*Figure 4-4 Temperature distribution along the mid-line of the airflow channel*

#### 4.2.3 CFD solver setup

The pressure-based solver is applied. For pressure-velocity coupling, the Coupled scheme is used. The spatial discretization used for the momentum and energy is the second order upwind scheme, and it used for the turbulent kinetic energy, specific dissipation rate and discrete ordinates is the first order upwind scheme. The pressure discretization is done by PRESTO!. The Least Squares Cell based method is used for the gradient reconstruction. Default values are kept for the under-relaxation factors. The criteria of residuals convergence are set as  $1e-03$  for the continuity, x, y, z momentum, turbulent kinetic energy and turbulent specific dissipation rate and  $1e-06$  for energy and do-intensity. Also, the heat fluxes transferred through the interior window and exterior window are monitored. When the change in the monitored values is less than one percent, the values are considered as stable.

#### 4.2.4 Model selection and evaluation

Proper selection of a turbulence model and a radiation model is important for model accuracy. In the Fluent software, available turbulence models include one-equation model (i.e., Spalart-Allmaras), two-equation model (i.e.,  $k-\omega$  model and  $k-\epsilon$  model) and Reynolds stress

model (i.e.,  $k\text{-kl-}\omega$  transition model, SST transition model), and available radiation models include the surface-to-surface model (S2S), P-1 model, Rosseland model, Discrete transfer method (DTRM) and Discrete ordinates model (DO). Among these available models, the  $k\text{-}\omega$  SST model and  $k\text{-}\epsilon$  RNG with enhanced wall function are the two most popular turbulence models for double-façade systems, and the S2S model and DO model are the two popular radiation models for glazing systems. To determine proper turbulence and radiation model, four cases are simulated and compared.

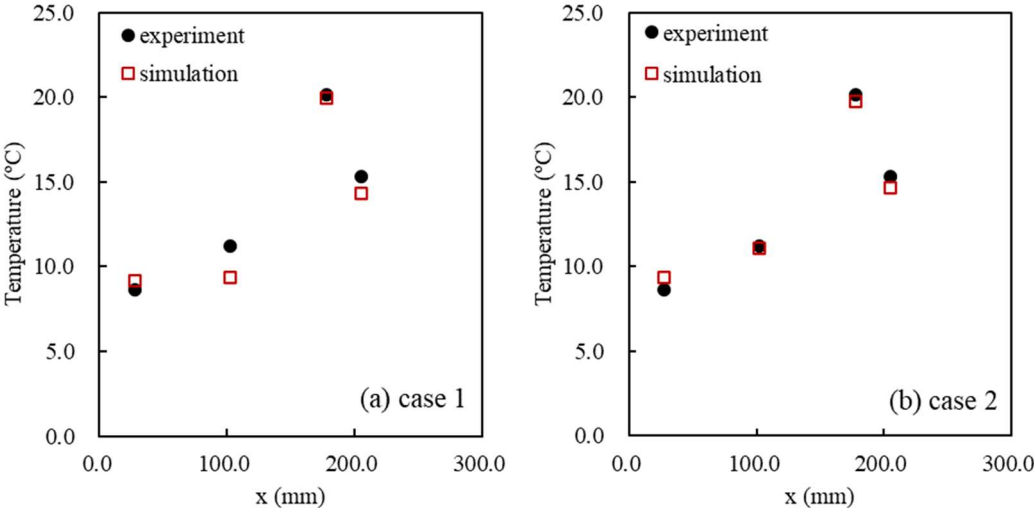
Case 1:  $k\text{-}\epsilon$  RNG enhanced model, S2S model

Case 2:  $k\text{-}\omega$  SST model, S2S model

Case 3:  $k\text{-}\omega$  SST model, DO model

Case 4:  $k\text{-}\epsilon$  RNG enhanced model, DO model

The data collected from the GHB experiment is used to validate the established CFD model. In particular, the exterior glazing temperature, interior glazing temperature, air temperature at the middle point of the airflow channel and outlet air temperature are selected as validation indicators. Figure 4-5 shows the comparison of experimental and numerical results in four cases.



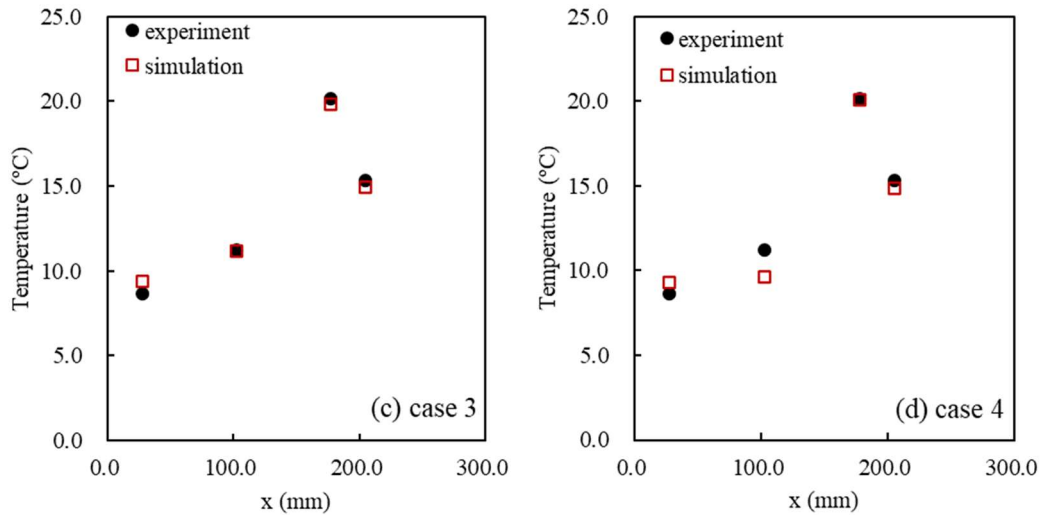


Figure 4-5 Comparison on temperatures between experiment results and simulation results

As can be seen, the CFD result is in good agreement with experiment. In particular, for the outlet air temperature, the errors are 0.96 °C, 0.67 °C, 0.37 °C and 0.46 °C for case 1, case 2, case 3 and case 4, respectively. For the interior glazing temperature, the deviations are 0.53 °C, 0.68 °C, 0.74 °C and 0.63 °C for case 1, case 2, case 3 and case 4, respectively. For the exterior glazing temperature, the errors are 0.18 °C, 0.39 °C, 0.30 °C and 0.04 °C for case 1, case 2, case 3 and case 4, respectively. For the air temperature at the middle point of airflow channel, the deviations between the experiments and simulations are obvious in case 1 and case 4. In particular, the deviations are 1.81 °C, 0.13 °C, 0.01 °C and 1.58 °C for case 1, case 2, case 3 and case 4. Also, the simulated U-values are compared with the experimental data. It can be found that the case that uses k- $\omega$  SST model and DO model has the best performance.

Table 4-4 Comparison of tested U-values and simulated U-value

	$U_{loss}$ [W/(m <sup>2</sup> K)]	$U_{use}$ [W/(m <sup>2</sup> K)]	$U_{eq}$ [W/(m <sup>2</sup> K)]
Exp.	2.80 ± 0.05	1.52 ± 0.06	1.27 ± 0.08
Case 1	2.6	1.4	1.2
Case 2	2.6	1.4	1.2
<b>Case 3</b>	<b>2.8</b>	<b>1.5</b>	<b>1.3</b>
Case 4	2.8	1.5	1.4



### 4.3 Results

In this chapter, the effects of various parameters on the U-values of three supply-air windows (VW1, VW2 and VW3) are analyzed. The studied parameters include window configuration parameters (i.e., window size, thermal conductivity of internal/external window frame, air flow rate, location of Low-E coating and emissivity of low-E coating) and boundary conditional parameters (i.e., inside/outside convective heat transfer coefficient and indoor/outdoor air temperatures). In the simulations, we change only one of these parameters in a predetermined range and keep the other parameters at a default value (see Table 4-3). To better understand the variations in the U-values, the outlet air temperature and temperature rise in supply-air double windows are also presented in this chapter. Moreover, a sensitivity analysis is provided in this section to evaluate the relative importance of studied parameters.

#### 4.3.1 Effects of window parameters

##### (1) Window size

The effect of window size on the U-values is illustrated in Figure 4-6. As shown in the Figure 4-6(a)-(c), the  $U_{loss}$  value decreases as the window area increases from 0.79 m<sup>2</sup> to 2.76 m<sup>2</sup>. A similar trend can be overserved in the  $U_{use}$  value. This means the heat recovery capacity per m<sup>2</sup> of window is reduced for a larger window. However, a larger temperature rise can be observed in Figure 4-6(d). This can be explained by the fact that the time for preheating supplied air is longer for a larger window. For the  $U_{eq}$  value, it increases by 26.5% for the VW1, 22.4% for the VW2 and 13.4% for the VW3 when the window area increases from 0.79 m<sup>2</sup> to 2.76 m<sup>2</sup>, which indicates the decreasing rate of the  $U_{loss}$  value is lower than that of the  $U_{use}$  value. This result agrees with the result found in [27].

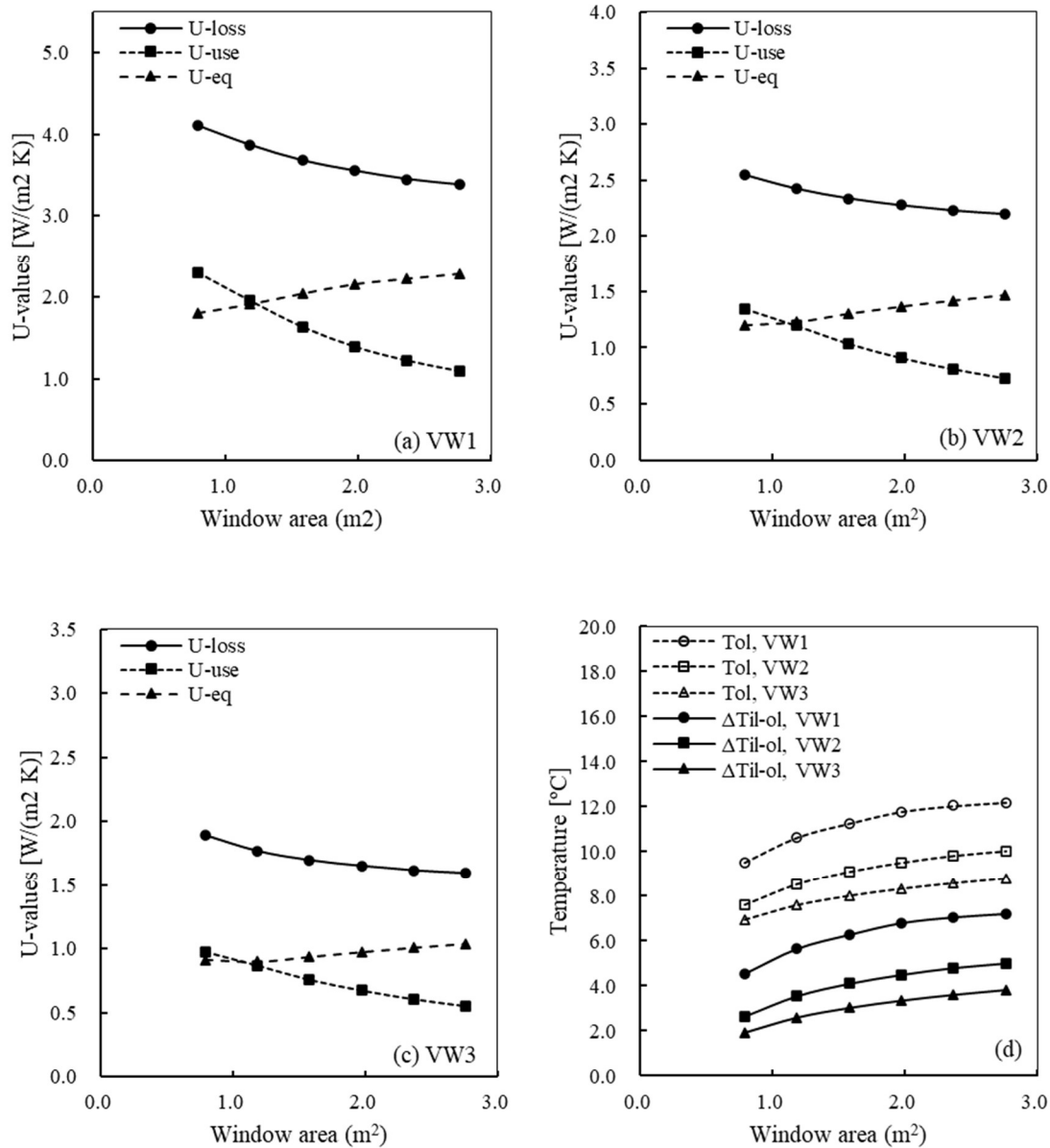


Figure 4-6 Correlations between the window area and U-values

(2) Thermal conductivity of external window frame

Figure 4-7(a)-(c) shows the correlations between the thermal conductivity of external window frame and U-values. It can be seen that a lower window frame thermal conductivity is associated to a lower  $U_{eq}$  value as the heat escaped from the window is reduced. The reductions of  $U_{eq}$  values are 6.5%, 6.4% and 6.8% for the VW1, VW2 and VW3, respectively, with the thermal conductivity decreasing from 0.5 W/(m K) to 0.1 W/(m K). Similar to the  $U_{eq}$  value, the  $U_{loss}$  value is also reduced as the thermal performance of external window frame is

improved. However, the reductions of the  $U_{loss}$  value are relatively weak. And thus, the trend of  $U_{use}$  value is opposite to the trend of  $U_{loss}$  value. As illustrated in Figure 4-7(d), there is no obvious change in the temperature rise.

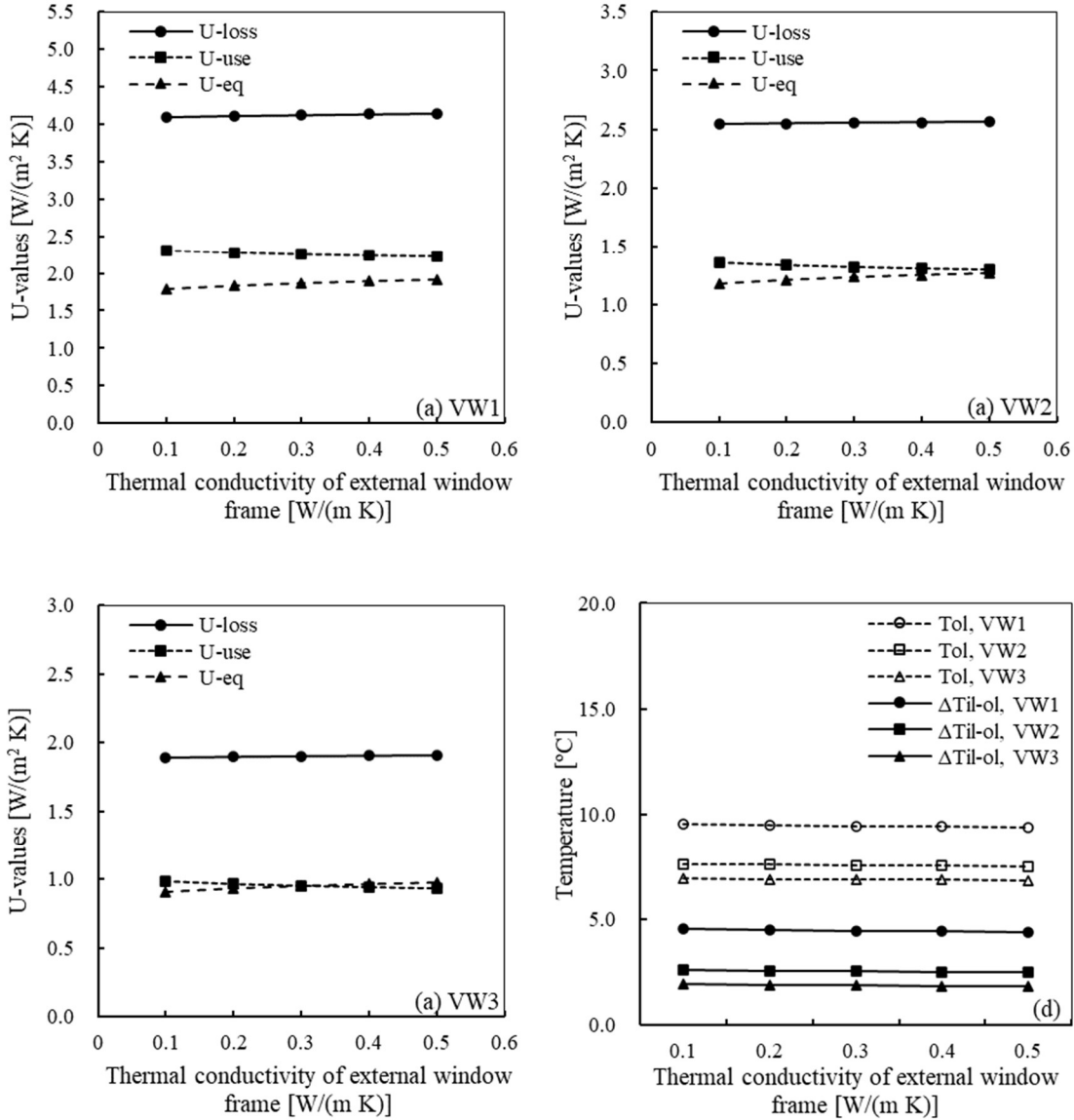


Figure 4-7 Correlations between the thermal conductivity of external window frame and U-values

(3) Thermal conductivity of internal window frame

Figure 4-8(a)-(c) shows the correlations between the thermal conductivity of internal window frame and U-values. As can be seen, using an internal window frame with a lower thermal conductivity can help reducing the  $U_{loss}$  value as the heat loss from indoor to the

airflow channel is reduced. In particular, as the thermal conductivity of inner window frame decreases from 0.5 W/(m K) to 0.1 W/(m K), the reduction of  $U_{loss}$  value is 6.1% for the VW1, 11.2% for the VW2 and 16.1% for the VW3. Similar to the  $U_{loss}$  value, both the  $U_{use}$  value and  $U_{eq}$  value are lower as the internal window has a better insulation performance. This implies both the recovered heat and heat escaped from the external window are reduced. As illustrated in Figure 4-8(d), the trend of temperature rises against the thermal conductivity of internal window frame is similar with that of the  $U_{use}$  value.

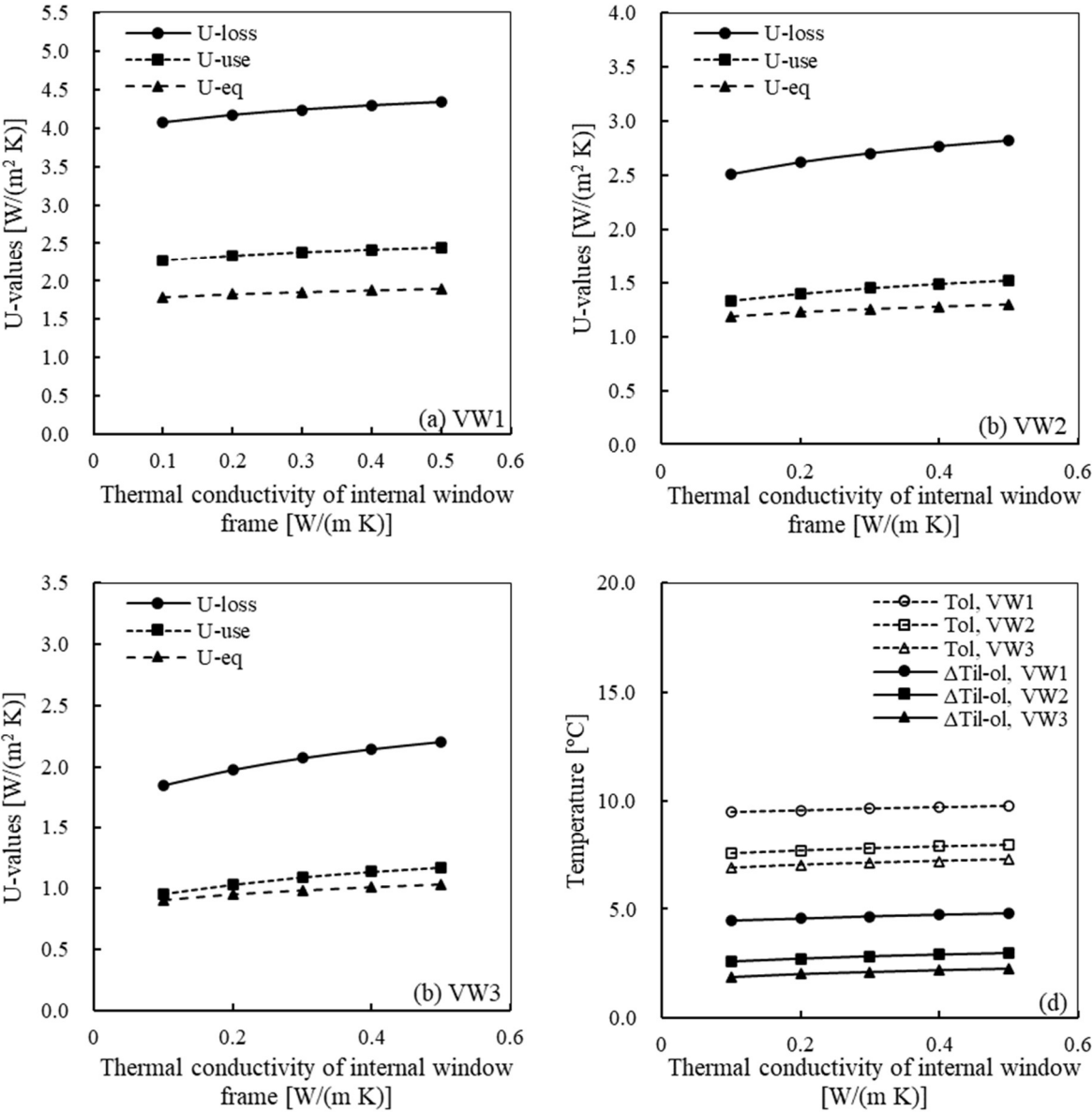
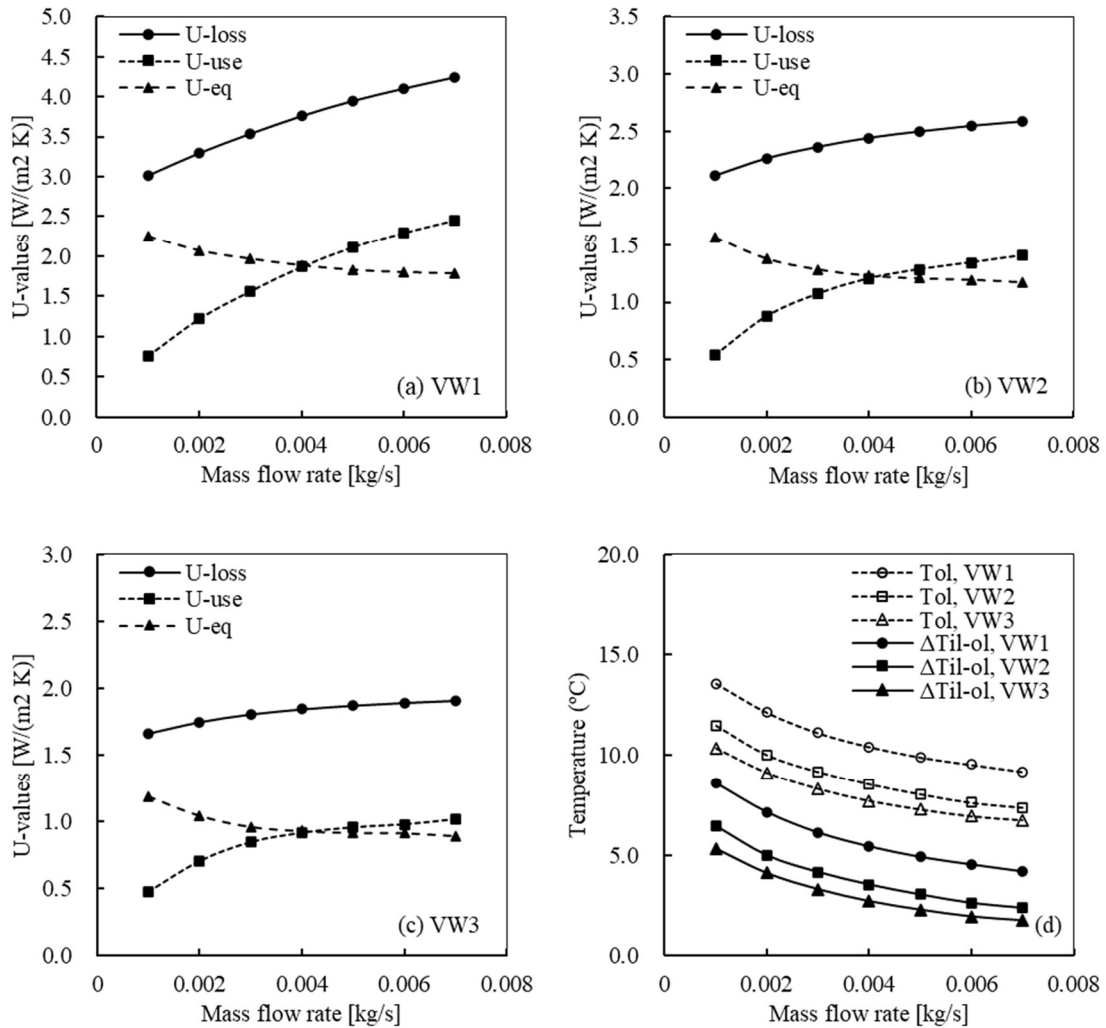


Figure 4-8 Correlations between the thermal conductivity of internal window frame and U-values

(4) Air flow rate

As shown in Figure 4-9(a)-(c), the  $U_{loss}$  value increases as the air mass flow rate increases. There are two explanations for this result. First, a larger air mass flow rate indicates a larger air velocity in the cavity which further enhances the convective heat transfer between the interior window and airflow. Second, the increase of air mass flow rate results in a shorter time for air preheating, and thus the average temperature of airflow channel is decreased and the temperature gradient between the indoor environment and airflow channel is increased. For the  $U_{use}$  value, it also increases when the air mass flow rate increases. However, as illustrated in Figure 4-9(d), the outlet air temperature and temperature rise are decreasing. For the  $U_{eq}$  value, it is reduced by 20.7%, 24.8% and 24.6% for the VW1, VW2 and VW3, respectively, as the air flow rate rises from 0.001 kg/s to 0.007 kg/s. This indicates the increase of  $U_{use}$  value is at a higher rate than  $U_{loss}$  value. This result agrees with the result found in [15,110].



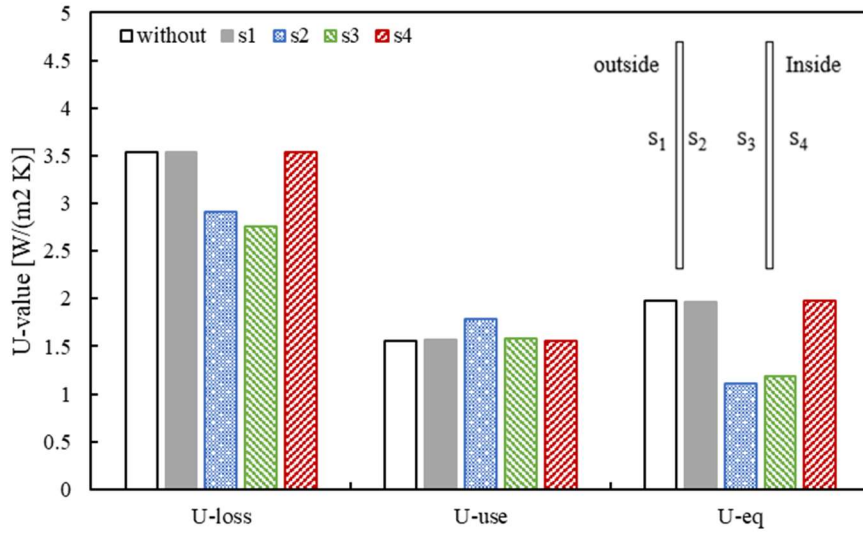
*Figure 4-9 Correlations between the air mass flow rate and U-values*

(5) Glazing optical properties

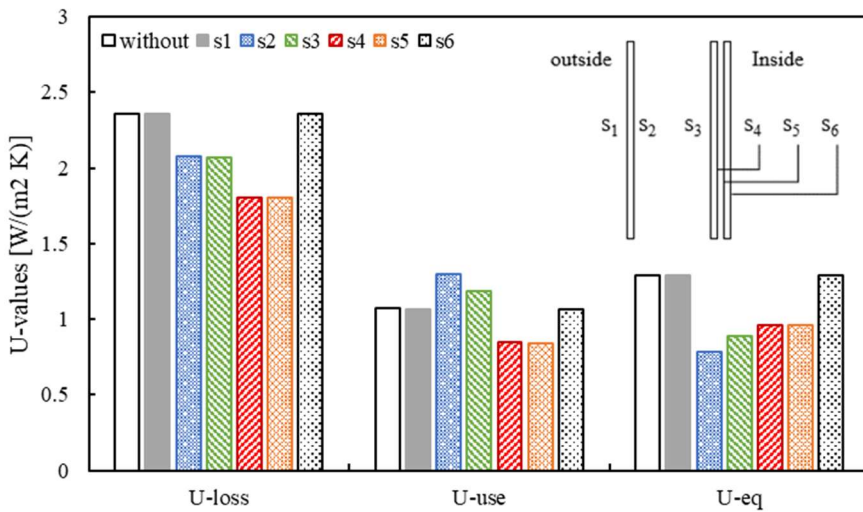
In this subsection, both the effect of the position of Low-E coating and the effect of the emissivity of Low-E coating on the U-values are investigated. The U-values of two window configurations (configuration I: composed of an inner single-glazed window and an outer single-glazed window, configuration II: composed of an inner double-glazed window and outer single-glazed window) with a Low-E coating on different positions are shown in Figure 4-10.

As illustrated in Figure 4-10, putting a Low-E coating (emissivity: 0.03) on the surfaces that face the environment (i.e., surface 1 and 4 of the configuration I, surface 1 and 6 of the configuration II) have a neglectable influence on the U-values. It can be explained by the fact that the long-wave radiation between environment and windows is insignificant under the simulated condition. From Figure 4-10(a), it can be seen that the  $U_{loss}$  value is lower when the Low-E coating is attached on the surface 3 than surface 2. While the  $U_{use}$  value is higher when the Low-E coating is attached on the surface 2 than surface 3. As a combined result of  $U_{loss}$  value and  $U_{use}$  value, the  $U_{eq}$  value is lowest by putting Low-E coating on surface 2. From Figure 4-10(b), it can be seen that the  $U_{loss}$  value is lower when the Low-E coating is attached on the surfaces facing the closed air layer (i.e., surface 4 and 5) than the surfaces facing the airflow channel (i.e., surface 2 and 3). While the  $U_{use}$  value is higher when the Low-E coating faces the airflow channel. The lowest  $U_{eq}$  value is obtained for the configuration II with Low-E coating on surface 2.

Comparing Figure 4-10(a) and (b), it can be said that the use of Low-E coating has a more significant contribution on the reduction of  $U_{eq}$  value of configuration I than configuration II. In particular, the reduction of  $U_{eq}$  value can reach 43.4% and 39.3% for configuration I and II, respectively.



(a) Configuration I



(b) Configuration II

Figure 4-10 Influence of the position of Low-E coating on the U-values

To further investigate the effect of emissivity on the U-values, the simulations were conducted by changing the emissivity of surface 2 in the range of 0.03-0.8. As shown in the Figure 4-11, the supply-air double window with a lower surface emissivity has a lower  $U_{loss}$  value. This implies that decreasing the surface emissivity is beneficial to reduce the long-wave radiation and thus reduce the heat loss from the indoor environment. For the  $U_{use}$  value, as the surface emissivity decreases, it increases with a rise on the outlet air temperature (as shown

in Figure 4-11(c)). Attributed to a decrease in the heat loss from the interior window and a rise in the heat recovered by the airflow, the heat escaped from the exterior is lower for the window with a lower emissivity, and correspondingly the  $U_{eq}$  value is lower. Another finding is that decreasing surface emissivity could reduce the deviation between the U-values of two configurations. For example, the deviation is  $0.7 \text{ W}/(\text{m}^2 \text{ K})$  between two configurations when the surface emissivity is 0.8 and it is reduced to  $0.3 \text{ W}/(\text{m}^2 \text{ K})$  when surface emissivity is reduced to 0.03. This observation is coherent with the finding that the effect of glazing emissivity on the  $U_{eq}$  of configuration I is more significant than the configuration II. In particular, the  $U_{eq}$  values of configuration I and II increase by 43.4% and 39.3%, respectively, with the emissivity increasing from 0.03 to 0.8.

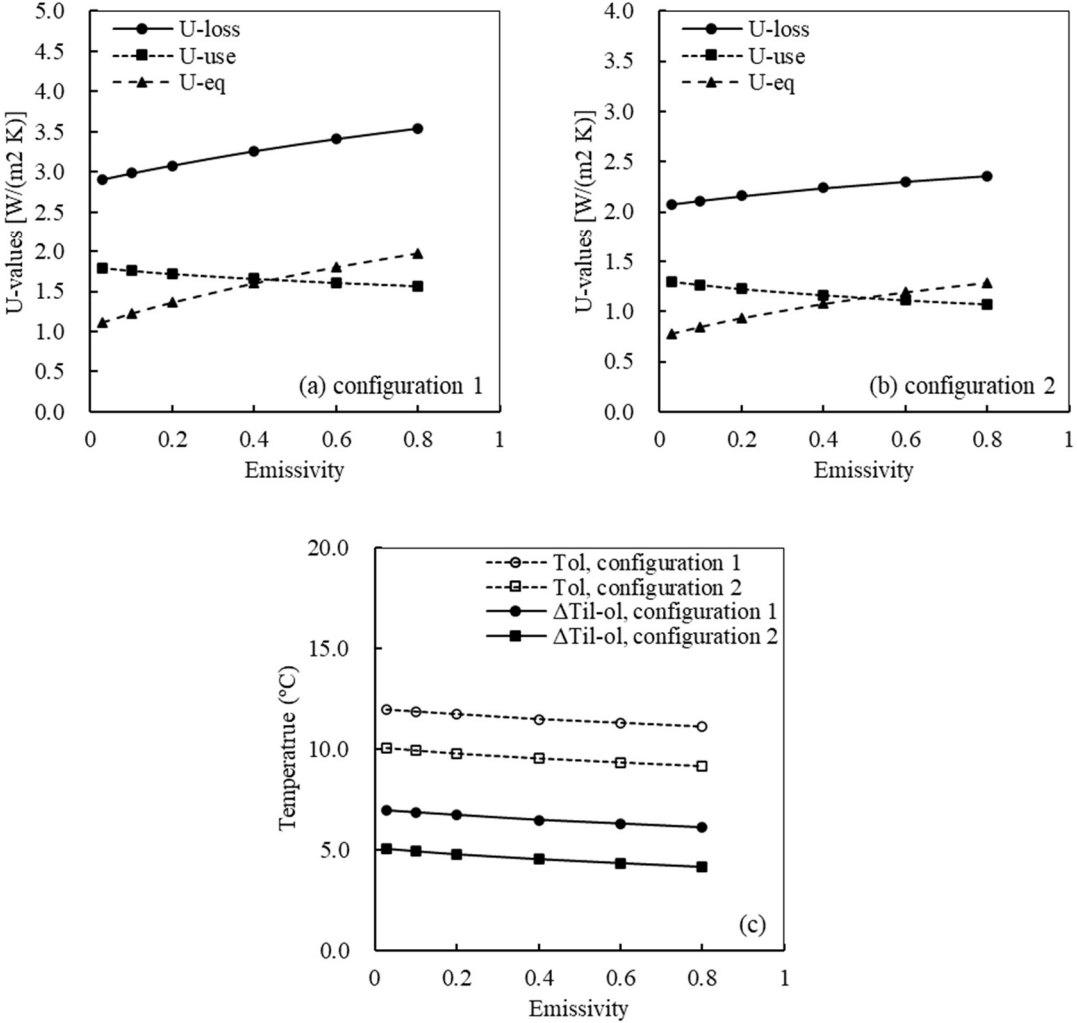


Figure 4-11 Correlations between the glazing surface emissivity and U-values



### 4.3.2 Effects of boundary conditions

#### (1) Convective heat transfer coefficient

For the convective heat transfer between environments and windows, it is highly related with the wind speed and wind direction. Due to the difficulty in defining an exact mathematical analysis between wind speed/wind direction and convective heat transfer, it is not possible at this time to identify the correlation between wind speed/wind direction and the U-values. Thus, the correlations between convective heat transfer coefficient and U-values are investigated in this section.

Figure 4-12(a)-(c) shows the variations of U-values along with an increase in the inside convective heat transfer coefficient, and an increase can be observed in the  $U_{loss}$  value. This is an expected result as the heat transfer between the interior window and indoor air is enhanced. In particular, the  $U_{loss}$  value is increased by 35.8% for the VW1, 22.5% for the VW2 and 18.3% for the VW3 when the inside convective heat coefficient increases from 1 to 10 W/(m<sup>2</sup> K). A similar trend can be observed in the  $U_{use}$  value and  $U_{eq}$  value. Associated with the  $U_{use}$  value, an ascent in the outlet air temperature and air temperature rise can be observed in Figure 4-12(d)).

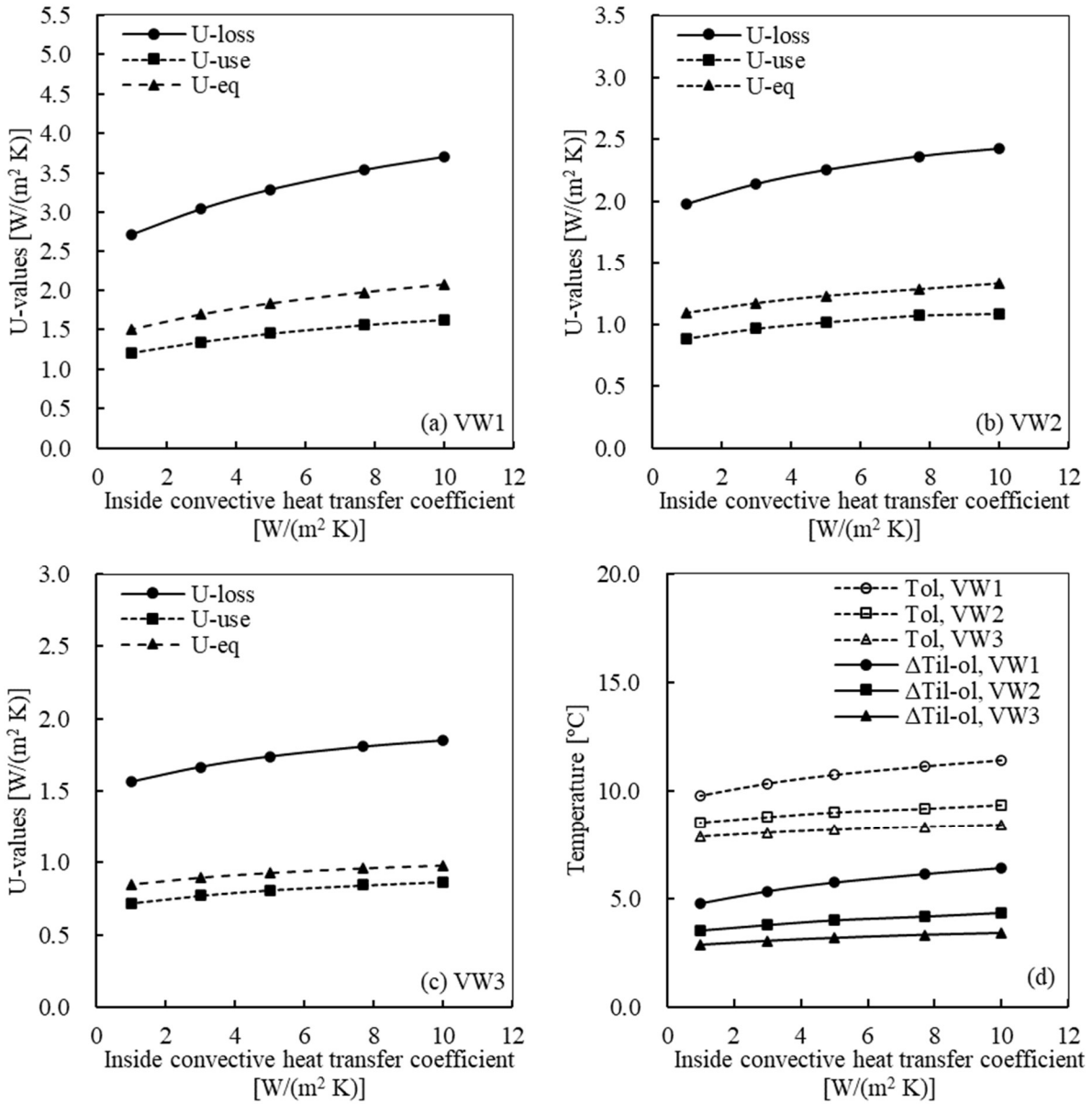


Figure 4-12 Correlations between the inside convective heat transfer coefficient and U-values

The correlation between the outside convection heat transfer coefficient and U-values are displayed in Figure 4-13(a)-(c). As shown in in this figure, when the studied coefficient increases from 5 W/(m<sup>2</sup> K) to 25 W/(m<sup>2</sup> K), the  $U_{eq}$  value increases by 23.0% for VW1, 20.5% for VW2 and 18.7% for VW3. This is because the convection heat transfer between the exterior window and outside environment is enhanced. Similar to the trend of  $U_{eq}$  value, the  $U_{loss}$  value also increases as the outside convection heat transfer increases. While for the  $U_{use}$  value, it decreases along with the increase of outside convective heat transfer coefficient.



Figure 4-13 Correlation between the outside convective heat transfer coefficient and U-values

## (2) Indoor/outdoor air temperatures

Despite from the above factors, the effect of air temperature difference between indoor and outdoor sides on the U-values is analyzed. In this section, two cases are included to achieve different temperature differences: 1. the indoor air temperature was fixed at 20 °C, and the outdoor air temperature was changed from 0 to 15 °C; 2. The outdoor air temperature was fixed at 5 °C, and the indoor temperature was changed from 10 to 25 °C. The simulated results of case #1 and case #2 are presented in Figure 4-14 and Figure 4-15, respectively.

As shown in the Figure 4-14(a)-(c), the effect of the temperature difference on the  $U_{loss}$  value is neglectable when the outdoor air temperature varies in the range of 0-15 °C. For the  $U_{use}$  value, it increases with an increase in the temperature difference between indoor and outdoor air temperatures. Associated with the  $U_{use}$  value, a larger air temperature rise which indicates the window has a better performance to recover heat loss can be observed for a larger temperature difference (as shown in Figure 4-14(d)). For the  $U_{eq}$  value, it decreases by 5.3%, 11.5% and 13.3% for VW1, VW2 and VW3 as the temperature difference increases from 5 °C to 20 °C. This result agrees with the finding discovered in [15].

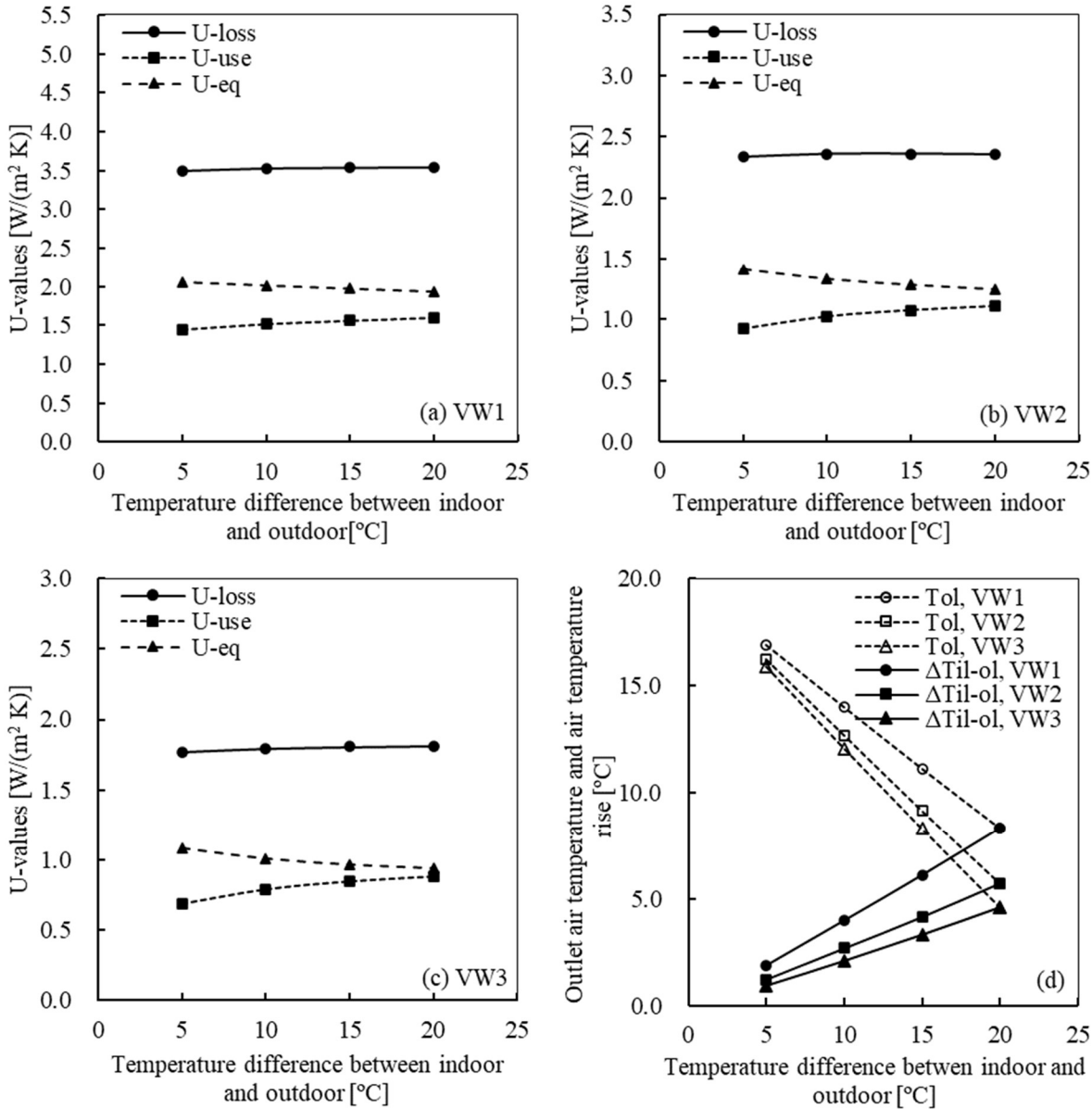


Figure 4-14 Correlations between the air temperature difference and U-values in Case #1

The results of case #2 are shown in Figure 4-15. It can be seen that there is a rise in the  $U_{loss}$  value and  $U_{use}$  value by increasing the temperature difference between indoor and outdoor air temperatures from 5 to 20 °C. An interesting observation in Figure 4-15 is that the trends of the  $U_{eq}$  values are not the same for different window configurations. In particular, for the VW1, the  $U_{eq}$  value slightly increases from 1.90 to 2.01 W/(m<sup>2</sup> K) when the temperature difference is raised from 10 to 25 °C. For the VW2, the  $U_{eq}$  value slightly decreases from 1.30 to 1.28 W/(m<sup>2</sup> K) when the temperature difference increases from 10 to 15 °C and then it slightly increases from 1.28 to 1.31 W/(m<sup>2</sup> K) as the temperature difference further increases from 15 to 25 °C. A similar trend could be observed in the VW3.

According to the above results, it can be concluded that excepted from the temperature difference between inside and outside environments, the indoor and outdoor air temperatures also need to be considered in the correlations of U-values.

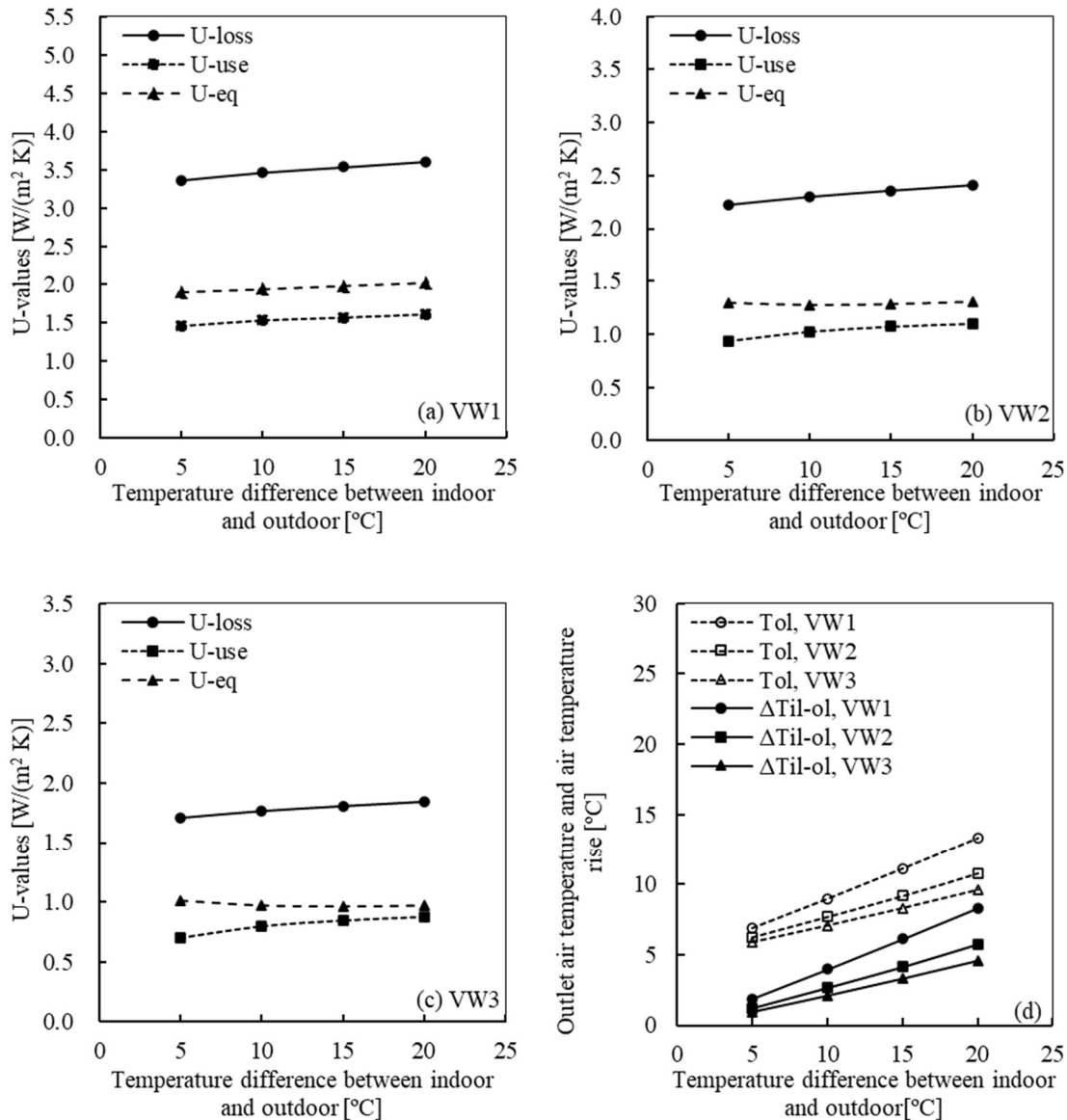


Figure 4-15 Correlations between the air temperature difference and U-values in Case #2

#### 4.3.3 Sensitivity analysis

To further compare the effects of different parameters on the U-values, the sensitivity analysis is performed based on the dimensionless sensitivity coefficients. The value of dimensionless sensitivity coefficient for each parameter indicates the relative contribution to the change in U-values. The dimensionless sensitivity coefficients are calculated based on the numerical partial derivative of the U-value with respect to the studied parameter, divided by the ratio of the U-value and the studied parameter [113]:

$$S_{i,j} = \frac{\left(\frac{\Delta C_i}{\Delta \alpha_j}\right)}{\left(\frac{C_i}{\alpha_j}\right)} \quad (4-1)$$

Where,  $S_{i,j}$  is the sensitivity coefficients;  $\Delta \alpha_j$  is the absolute change in the studied parameter;  $\alpha_j$  is the value of studied parameter;  $C_i$  is the U-value.

The calculated dimensionless sensitivity coefficients for the VW1, VW2 and VW3 are listed in Table 4-5, Table 4-6 and Table 4-7. As shown in Table 4-5, Table 4-6 and Table 4-7, the most sensitive window configuration parameters and the most sensitive boundary conditional parameters are different for different window configurations and for different U-values.

*Table 4-5 Sensitivity analysis results of the VW1*

	$U_{loss}$ [W/(m <sup>2</sup> K)]	$U_{use}$ [W/(m <sup>2</sup> K)]	$U_{eq}$ [W/(m <sup>2</sup> K)]
Air flow rate, kg/s	0.319	0.804	0.239
Thermal conductivity of internal window frame, W/(m K)	0.076	0.083	0.066
Thermal conductivity of external window frame, W/(m K)	0.013	0.044	0.081
Outside convective heat transfer coefficient, W/(m <sup>2</sup> K)	0.080	0.104	0.234
Inside convective heat transfer coefficient, W/(m <sup>2</sup> K)	0.293	0.283	0.301
Outdoor temperature, °C	0.018	0.131	0.071
Indoor temperature, °C	0.118	0.149	0.093
Window area, m <sup>2</sup>	0.246	0.732	0.294

*Table 4-6 Sensitivity analysis results of the VW2*

	$U_{loss}$ [W/(m <sup>2</sup> K)]	$U_{use}$ [W/(m <sup>2</sup> K)]	$U_{eq}$ [W/(m <sup>2</sup> K)]
Air flow rate, kg/s	0.205	0.714	0.281
Thermal conductivity of internal window frame, W/(m K)	0.140	0.161	0.115
Thermal conductivity of external window frame, W/(m K)	0.011	0.054	0.080

Outside convective heat transfer coefficient, W/(m <sup>2</sup> K)	0.052	0.126	0.212
Inside convective heat transfer coefficient, W/(m <sup>2</sup> K)	0.204	0.208	0.201
Outdoor temperature, °C	0.008	0.214	0.153
Indoor temperature, °C	0.124	0.257	0.012
Window area, m <sup>2</sup>	0.191	0.640	0.257

*Table 4-7 Sensitivity analysis results of the VW3*

	$U_{loss}$ [W/(m <sup>2</sup> K)]	$U_{use}$ [W/(m <sup>2</sup> K)]	$U_{eq}$ [W/(m <sup>2</sup> K)]
Air flow rate, kg/s	0.146	0.615	0.274
Thermal conductivity of internal window frame, W/(m K)	0.201	0.235	0.162
Thermal conductivity of external window frame, W/(m K)	0.010	0.065	0.085
Outside convective heat transfer coefficient, W/(m <sup>2</sup> K)	0.040	0.125	0.197
Inside convective heat transfer coefficient, W/(m <sup>2</sup> K)	0.172	0.189	0.157
Outdoor temperature, °C	0.032	0.284	0.177
Indoor temperature, °C	0.118	0.321	0.063
Window area, m <sup>2</sup>	0.221	0.604	0.166
Emissivity	0.124	0.179	0.408



## 4.4 Conclusions

In this chapter, a comprehensive parametric study is performed to help understand variations in the U-values of supply-air double windows with different window configuration parameters and under different boundary conditional parameters and identify the most important parameters that contribute to the variations in the U-values. The studied parameters include the window size, thermal conductivity of internal/external window frame, air flow rate, position of Low-E coating, glazing surface emissivity, inside/outside convective heat transfer coefficient and indoor/outdoor air temperatures. To conduct the parametric study, a three-dimensional CFD model was established and evaluated by experiments data. In total, 145 scenarios were simulated. The main results are summarized as followings:

(1) For a larger window size, the  $U_{loss}$  and  $U_{use}$  values are lower while the  $U_{eq}$  value is higher.

(2) For the thermal conductivity of internal window frame and inside convective heat transfer coefficient, their effects on the  $U_{loss}$  value,  $U_{use}$  value and  $U_{eq}$  value are similar. In particular, as the value of the studied parameter increases, the  $U_{loss}$  value,  $U_{use}$  value and  $U_{eq}$  value are all increased.

(3) For the parameters of thermal conductivity of external window frame and outside convective heat transfer coefficient, as the value of the studied parameter increases, the  $U_{loss}$  and  $U_{eq}$  value increase while the  $U_{use}$  value decreases.

(4) As the air flow rate increases, both the  $U_{loss}$  value and  $U_{use}$  value increase while the  $U_{eq}$  value decreases.

(5) The  $U_{eq}$  value can achieve the lowest value by putting the Low-E coating on the surface of external window (surface 2) that facing the airflow channel. Moreover, a decrease in the emissivity of surface 2 can help reduce the  $U_{eq}$  value of the studied supply-air windows.

(6) Excepted from the temperature difference between inside and outside environments, the indoor and outdoor air temperatures also need to be considered in the correlations of U-values.

(7) In terms of the  $U_{eq}$  value, the most influential boundary conditional parameter is the interior convective heat transfer coefficient for the VW1 and VW2, and it is the exterior convective heat transfer coefficient for the VW3. Moreover, the most influential configuration parameters are the window size, air flow rate and emissivity for the VW1, VW2 and VW3, respectively.

## **5 Determination, Analysis and Assessment of a New Dynamic U-value Calculation Applied to Supply-air Double Windows**

## 5.1 Introduction

As analyzed above, the U-values of supply-air windows are changed with boundary conditions. In this view, a calculation of dynamic U-values is required to facilitate the use of U-value under different boundary conditions. Although CFD simulations can provide accurate U-values, they cannot provide fast feedback in the early design stage due to high computational costs. As a surrogate model, the regression model with high computational efficiency is widely used in engineering fields to find the correlation between model inputs and outputs [114]. The most popular regression method is the multiple linear regression (MLR) model due to its simplicity. It has a good performance to assess a linear correlation. But if the correlation is more complex and not strictly linear, using such a model might lead to a large deviation between the real value and calculated value. Considering the limitation of the MLR model, different regression models are applied and analyzed in this chapter, including the K-nearest neighbor regression (KNNR), support vector regression (SVR), random forest regression (RFR), extra tree regression (ETR), gradient boosting regression (GBR) and extreme gradient boosting regression (XGBR). The following objectives are pursued in this chapter:

- (1) Establish regression models to calculate dynamic U-values under different boundary conditions.
- (2) Compare different regression models and provide suggestions for model selection.
- (3) Investigate the impact of dataset sizes on the model performance.

This chapter includes five sections. Section 5.1 is the introduction. Section 5.2 introduces the regression models and model performance evaluation indicators. Sections 5.3 determines the train/test splitting ratio for each model and optimizes models by tuning model hyper-parameters. In section 5.4, different regression models are compared and also the effect of dataset sizes on model performance is investigated. Section 5.5 concludes this chapter.

## 5.2 Methodology

### 5.2.1 Framework

The framework of establishing a regression model is shown in Figure 5-1. It consists of five steps, including the data collection, data pre-processing, dataset preparation, model training and optimization, and model validation.

Step 1: Data collection. A three-dimensional CFD model was established and evaluated in Chapter V. Based on the evaluated CFD model, U-values of a supply-air double window under different boundary conditions were simulated and collected. The detailed information of simulations is described as follows. (1) window configuration: a supply-air double window composed of two clear single-glazed windows with a size of 0.888 m×0.888 m; (2) Inside convective heat transfer coefficient ( $h_{int}$ ): 1, 3, 5, 7.7, 10 W/(m<sup>2</sup> K); Outside convective heat transfer coefficient ( $h_{ext}$ ): 5, 10, 15, 20, 25 W/(m<sup>2</sup> K); (3) Indoor air temperature: 20 °C; Outdoor air temperature: 0, 5 and 10 °C; (4) Air mass flow rate: 0.001, 0.003 and 0.006 kg/s. In total, 225 scenarios were simulated. The dataset that collects the  $U_{loss}$  value,  $U_{eq}$  value and  $U_{use}$  value is denoted as D1, D2 and D3, respectively.

Step 2: Data pre-processing. The min-max normalization is employed to transform values of variable  $x_i$  into the range of 0-1 [115].

$$x_i = (x_i - x_{min}) / (x_{max} - x_{min}) \quad (5-1)$$

Step 3: Dataset preparation. The dataset after pre-processing is split into a training dataset and a testing dataset. The training dataset is utilized to train and optimize models, and the testing dataset is utilized to validate the optimized models.

Step 4: Model training and optimization. In this step, the hyper-parameters are tuned based on k-fold cross validation.

Step 5: Model validation. The calculated U-values and the collected U-values are compared.

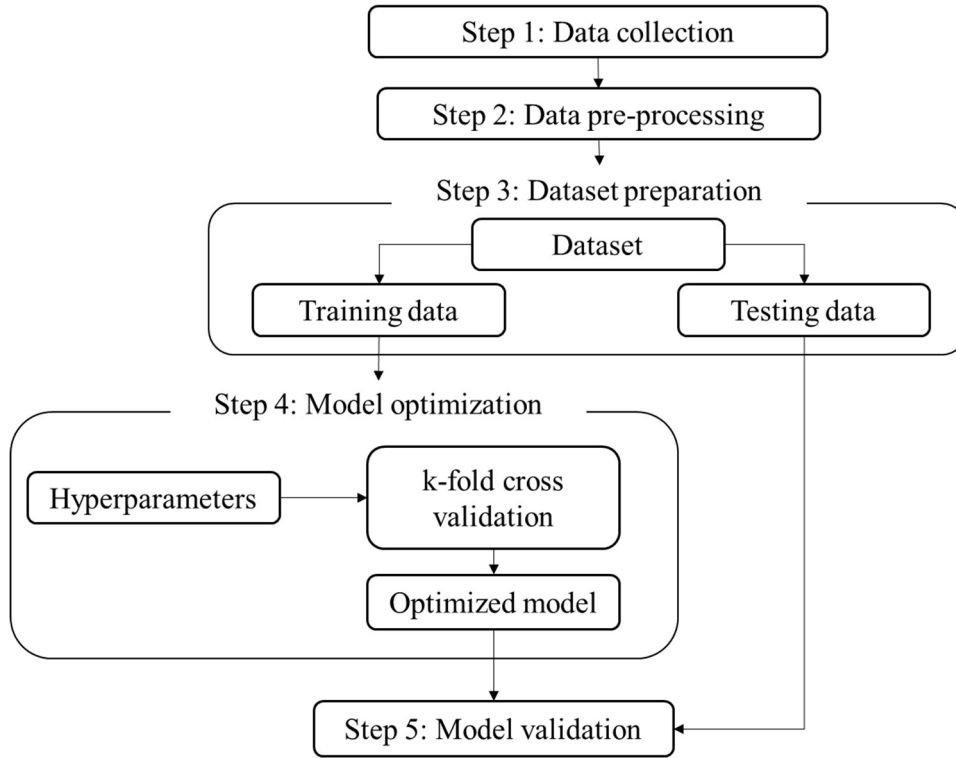


Figure 5-1 Schematic of framework

### 5.2.2 Regression models

In this section, seven regression models are introduced, including the MLR, KNNR, SVR, RFR, ETR, GBR and XGBR models.

#### (1) Multiple linear regression (MLR)

The MLR model is the most often used regression model due to its simplicity. Given a dataset  $D = \{(x_1, y_1), (x_2, y_2), \dots, (x_m, y_m)\}$ , the multiple linear regression could be defined as [11]:

$$f(x) = \beta_0 + \beta_1 x_1 + \beta_2 x_2 + \dots + \beta_m x_m + \varepsilon \quad (5-2)$$

Where,  $f(x)$  is the calculated value;  $\beta_0$  is the y-intercept;  $\beta_i$  is the regression coefficients;  $\varepsilon$  represents the random error.

Parameter estimation (i.e., estimate the regression coefficients) is an important step in establishing the MLR model. Its objective is to find an optimized line that can minimize the Euclidean distance between the true value and the line, which can be expressed as:

$$\min \sum_{i=1}^m (f(x) - y_i)^2 \quad (5-3)$$

## (2) K-nearest neighbor regression (KNNR)

The principle of the KNNR model is to find  $K$  nearest data points. The process of KNNR model includes the following three steps [115]:

(a) Calculate the Euclidean distance ( $D$ ) between the calculated data point ( $x$ ) and given data points ( $x_i$ ). The Euclidean distance is expressed as Eq. (5-4).

$$D = \sqrt{\sum_{i=1}^m (x_i - x)^2} \quad (5-4)$$

(b) Select the nearest  $K$  data points based on the calculated Euclidean distance.

(c) The average value of the selected  $K$  data points (expressed as Eq. (5-5)) is calculated as the model output result.

$$y = \frac{1}{K} \sum_{y_i \in C} y_i \quad (5-5)$$

## (3) Support vector regression (SVR)

The SVR model mainly includes two parts. The first part is to map the inputs from low dimensional spaces into higher dimensional spaces by using kernel functions. The popular kernel functions include the linear kernel, polynomial kernel and radial basis function (RBF) kernel which are expressed as the following equations [114,115]:

(a) Linear kernel:

$$K(x_i, x_j) = x_i \cdot x_j \quad (5-6)$$

(b) Polynomial kernel:

$$K(x_i, x_j) = (x_i \cdot x_j + 1)^d \quad (5-7)$$

(c) Radial basis function (RBF) kernel:

$$K(x_i, x_j) = \exp(-\gamma \|x_i - x_j\|^2), \gamma > 0 \quad (5-8)$$

The second part is to find an optimized hyperplane to map non-linear functions. The hyperplane could be described as the Eq. (5-9):

$$f(x) = W^T \varphi(x) + b \quad (5-9)$$

Where,  $W$  is the normal vector which determines the direction of the hyperplane;  $b$  is the distance between the hyperplane and coordinate system origin;  $\varphi(x)$  is the map function to map  $x_i$  from low dimensional spaces into higher dimensional spaces.

The residual error between the calculated result  $f(x)$  and the true value  $y$  is expressed as Eq. (5-10).

$$R(x, y) = y - f(x) \quad (5-10)$$

When the residual error is within a range of  $\varepsilon$  ( $-\varepsilon \leq R(x, y) \leq \varepsilon$ ), its value is set as 0. When the residual error exceeds the range of  $(-\varepsilon, \varepsilon)$ , it is denoted as  $\xi_j$  if the model calculated value is smaller than the real value, and it is denoted as  $\xi_i$  if the model calculated value is larger than the real value. A schematic of  $\xi_i$  and  $\xi_j$  is shown in Figure 5-2.



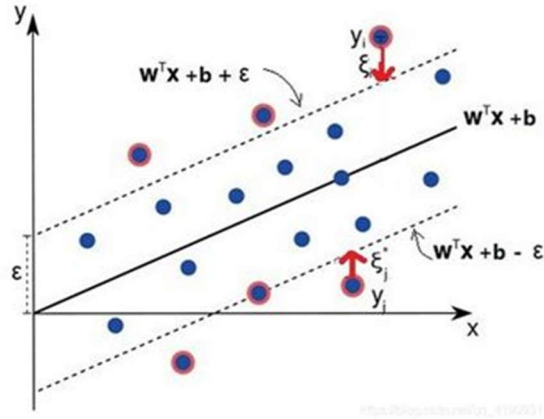


Figure 5-2 Schematic of the support vector regression

$\xi_i$  and  $\xi_j$  are defined as Eq. (5-11) and Eq. (5-12), respectively.

$$\xi_j = \begin{cases} 0, & R(x_i, y_i) - \epsilon \leq 0 \\ R(x_i, y_i) - \epsilon, & \text{others} \end{cases} \quad (5-11)$$

$$\xi_i = \begin{cases} 0, & \epsilon - R(x_i, y_i) \leq 0 \\ \epsilon - R(x_i, y_i), & \text{others} \end{cases} \quad (5-12)$$

The target of SVR is minimizing the  $\epsilon$  insensitive loss function and the residual errors.

Therefore, the objective function is written as Eq. (5-13):

$$\min F(W, b, \xi_i, \xi_i^*) = \frac{1}{2} \|W\|^2 + C \sum_{i=1}^N (\xi_i + \xi_i^*) \quad (5-13)$$

With the constraints:

$$y_i - W^T \varphi(x_i) - b \leq \epsilon + \xi_i, \quad i = 1, 2, \dots, N$$

$$W^T \varphi(x_i) - b - y_i \leq \epsilon + \xi_i^*, \quad i = 1, 2, \dots, N$$

$$\xi_i \geq 0, \xi_i^* \geq 0, \quad i = 1, 2, \dots, N$$

#### (4) Random forest regression (RFR)

The RFR model is an ensemble technique that constructs multiple regression trees and combines calculated results from multiple regression trees [116]. The structure of a random forest is shown in Figure 5-3.

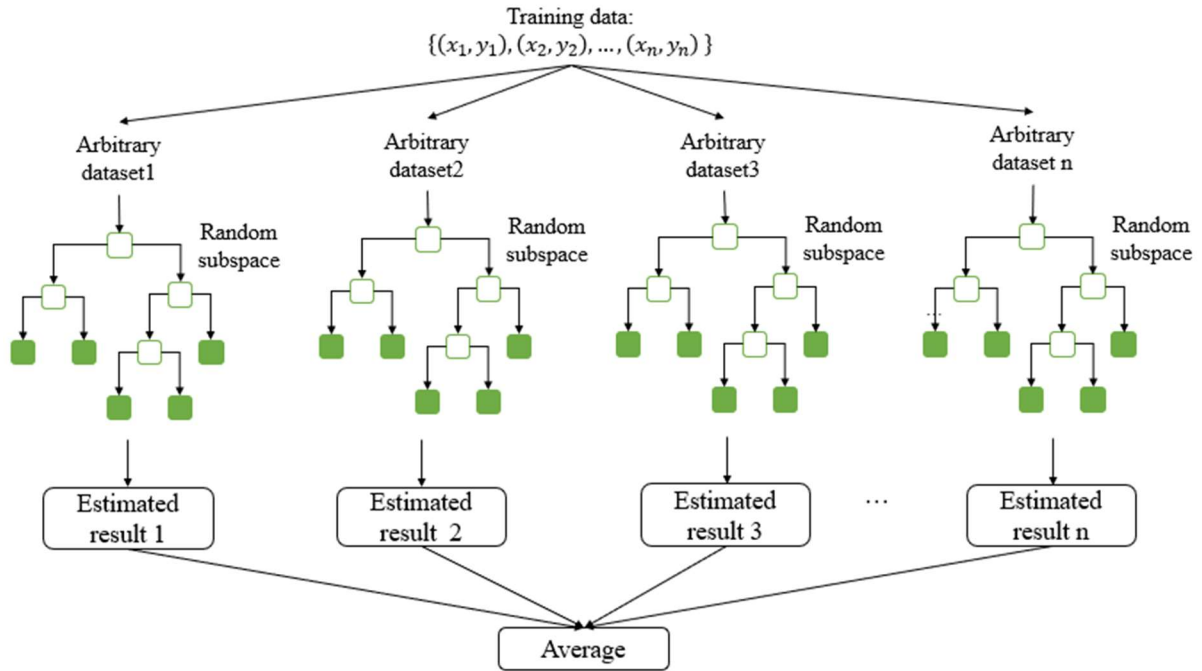


Figure 5-3 Schematic of the random forest regression

As shown in Figure 5-3, a regression tree includes a root node which includes all of the training data, several internal nodes and several leaf nodes which indicate the calculated results. The process of building a regression tree is summarized as following two steps:

(a1) Select a segmentation variable and a segmentation point to split a node into two new nodes. The selection is based on calculating the purity of nodes after segmentation. A higher purity indicates a better segmentation. The purity of a node can be calculated by Eq. (5-14):

$$H = \frac{1}{n} \sum_{i \in n} (y_n - \widehat{y}_n)^2 \quad (5-14)$$

Where,  $n$  is the number of data points in the node.

The purity of two nodes after segmentation can be calculated by Eq. (5-15):

$$H_{1+2} = \frac{n_1}{n_1 + n_2} H_1 + \frac{n_2}{n_1 + n_2} H_2 \quad (5-15)$$

(b1) Repeat step (a1) and create new nodes until all of the nodes contain less than the minimum number of samples.

In the random forest regression, each regression tree is independent of the other, and its building progress is summarized as the following:

(a) Create a subset by randomly select  $k$  points from the original dataset;

(b) Construct a regression tree for the subset;

(c) Decide the number of trees and repeat the step (a) and step (b);

(d) The final calculated value is the average value of calculation results from all regression trees.

#### (5) Extra tree regression (ETR)

The ETR model is the extension of the RFR model [116]. There are two differences between these two models: (a) The RFR model randomly selects several data points from original data points as training dataset for each regression tree. But for the ETR model, it used the original data points as the training dataset for each regression tree. (b) The RFR model select split variables and points based on the impurity calculation while the ETR model randomly chooses the variables and points for splitting the node.

#### (6) Gradient boosting regression (GBR)

Similar to the RFR model and ETR model, the GBR model is also an ensemble technique [116]. The largest difference between the GBR model and the RFR and ETR models is that the GBR model builds regression tree sequentially. The result of the GBR is the sum of the results generated by each trained regression tree. The structure of the GBR model is shown in Figure 5-4.

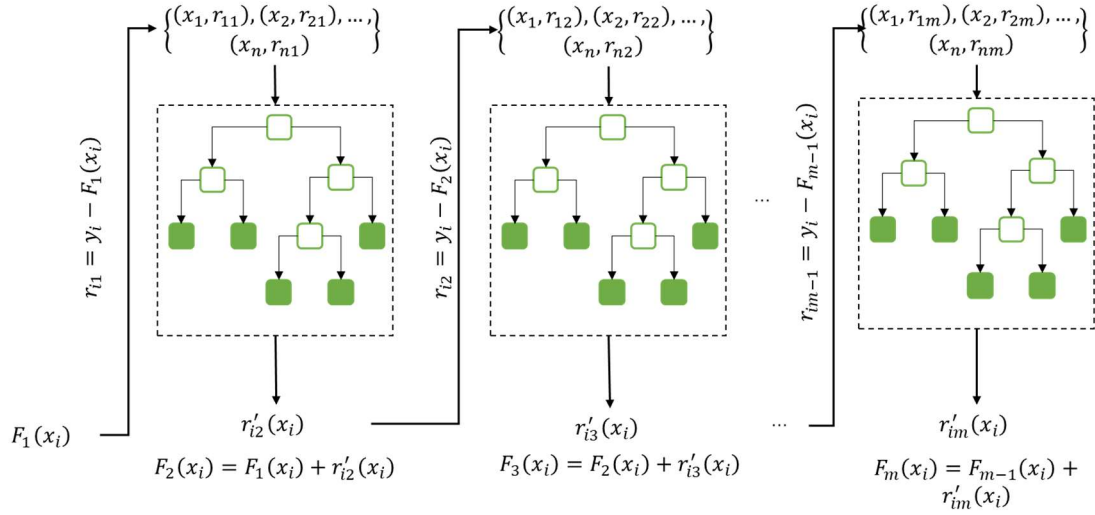


Figure 5-4 Schematic of the GBR model

The process of GBR could be summarized as:

- (a) Initialize model with a constant value.

$$F_1(x_i) = \operatorname{argmin}_{\gamma} \sum_{i=1}^n L(y_i, \gamma) \quad (5-16)$$

- (b) Calculate negative gradient of loss functions ( $L(y, F(x))$ ) as an approximation of the residual errors:

$$L(y_i, F_m(x_i)) = (y_i - F_m(x_i))^2 \quad (5-17)$$

$$r_{mi} = - \left[ \frac{\partial L(y_i, F_m(x_i))}{\partial F(x_i)} \right]_{F(x)=F_{m-1}(x)} \quad (5-18)$$

- (c) Train a new model  $h_m(x_i)$  by using the dataset  $\{(x_i, r_{mi})\}_{i=1}^n$  as a training dataset.

- (d) Compute multiplier  $\gamma_m$  by solving Eq. (5-19):

$$\gamma_m = \operatorname{argmin}_{\gamma} \sum_{i=1}^n L(y_i, F_{m-1}(x_i) + \gamma h_m(x_i)) \quad (5-19)$$

$$F_m(x) = F_{m-1}(x) + \gamma_m h_m(x) \quad (5-20)$$

(e) Repeat steps (b) to (d) until it starts overfitting or the sum of residuals become constant.

#### (7) Extreme Gradient Boosting regressor (XGBR)

The XGBR model is an extension of the GBR model [116]. In the GBR model, the loss function  $L(y, F(x))$  is solved by the first-order derivative while in the XGBR model it is solved by the Tylor expansion. In addition, a regularization function is added in the XGBR model to avoid overfitting problem.

#### 5.2.3 Model performance evaluation indicators

Five indicators are used to evaluate the model performance, including the coefficient of determination ( $R^2$ ), mean absolute error (MAE), normalized mean absolute error (NMAE), root mean square error (RMSE) and normalized root mean square error (NRMSE). These indicators are expressed below [116]:

$$R^2 = 1 - \frac{\sum_{i=1}^n (y_i - \hat{y}_i)^2}{\sum_{i=1}^n (y_i - \bar{y}_i)^2} \quad (5-21)$$

$$MAE = \frac{\sum_{i=1}^n |y_i - \hat{y}_i|}{n} \quad (5-22)$$

$$NMAE = \frac{\sum_{i=1}^n (y_i - \hat{y}_i)}{y_{max} - y_{min}} \quad (5-23)$$

$$RMSE = \sqrt{\frac{\sum_{i=1}^n (y_i - \hat{y}_i)^2}{n}} \quad (5-24)$$

$$NRMSE = \frac{\sqrt{\frac{\sum_{i=1}^n (y_i - \hat{y}_i)^2}{n}}}{y_{max} - y_{min}} \quad (5-25)$$

Where,  $y_i$  is the collected values;  $\hat{y}_i$  is the calculated values;  $n$  is the number of validation data.  $R^2$  is measure of the ability of the model to explain the outputs. Its value is in the range

of 0-1, and higher value indicates a higher explanatory ability. For the *MAE*, *NMAE*, *RMSE* and *NRMSE*, a smaller value indicates a higher accuracy.

### 5.3 Model training and optimization

In this subsection, the impact of train/test splitting ratios on the model performance is evaluated and the best train/test splitting ratio is determined for each regression model. Moreover, the hyper-parameters of the KNNR, SVR, RFR, ETR, GBR and XGBR models are tuned to optimize models. The MAE value is used as a model performance indicator in this sector.

#### 5.3.1 Sensitivity analysis on the train/test splitting ratio

Prior to training models, the datasets (D1, D2 and D3) need to be split into training datasets and testing datasets. However, there is no appropriate train/test splitting ratio given in literatures. Considering this research gap, different splitting ratios (i.e., 0.1, 0.2, 0.3, 0.4, 0.5, 0.6, 0.7, 0.8 and 0.9) are compared in this section. The split strategy is to randomly choose a fraction of dataset, and this is then repeated 100 times for each splitting ratio. The average MAE value over 100 times for each splitting ratio is calculated and its variation along with the train/test splitting ratio is shown in Figure 5-5. As shown in this figure, the impact of train/test splitting ratio is more significant on the KNNR model than on the other six models. This is because results of the KNNR model are dependent on the data points that near to the calculated data, and a larger ratio of training data indicates that it is more possible to find a data point close to the calculated data. With an increase in the train/test splitting ratio, the model accuracy increases as the average MAE value decreases. A similar trend can be found in the SVR, RFR, ETR, GBR and XGBR models. Thus, for the KNNR, SVR, RFR, ETR, GBR and XGBR models, the train/test splitting ratio of 0.9 is selected for further hyper-parameter optimization. But for the MLR model, as shown in Figure 5-5, the splitting ratio has an insignificant impact on the average MAE value.

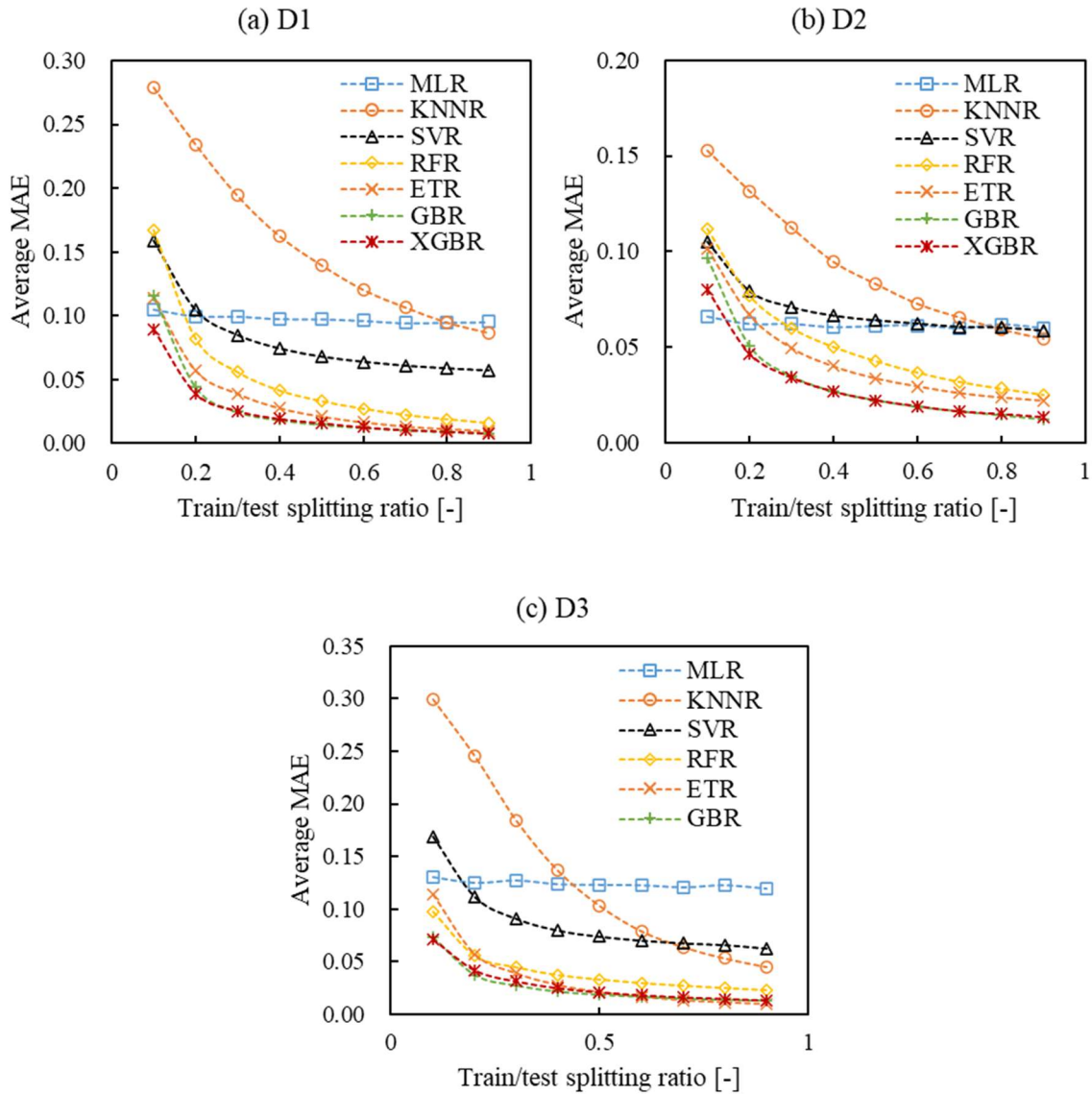


Figure 5-5 Correlation between the train/test splitting ratio and average MAE value for the dataset D1, D2 and D3

To further determine the train/test splitting ratio for the MLR model, the boxplots of MAE values for 100 times are shown in Figure 5-6. It can be seen that the peak MAE value is always lowest when the splitting ratio is 0.7 for three datasets. Thus, the splitting ratio of 0.7 is used for the MLR model in further analysis.



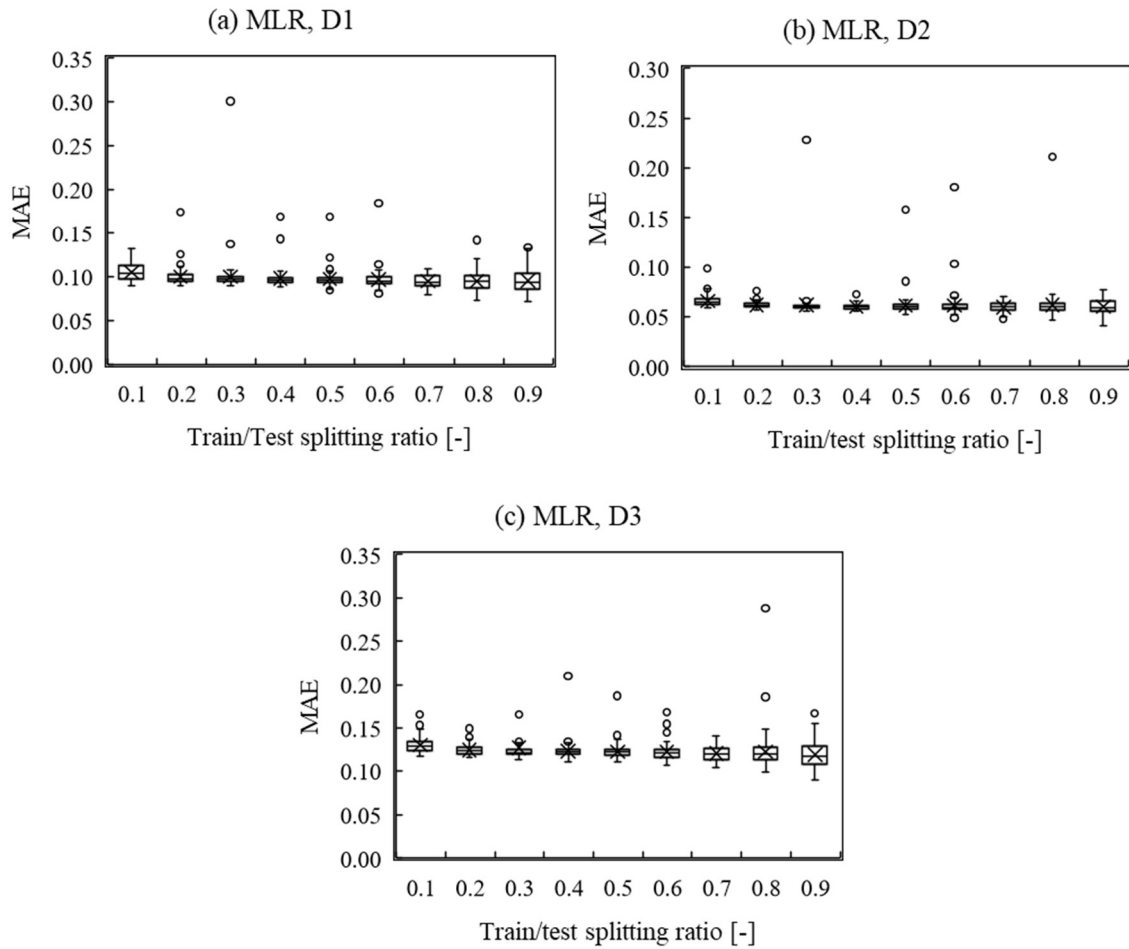


Figure 5-6 Boxplots of MAE values for different train/test splitting ratios

### 5.3.2 Hyper-parameter optimization

For the KNNR, SVR, RFR, ETR, GBR and XGBR models, the accuracy and robustness of models are highly related with hyper-parameters. To optimize these models, it is necessary to tune their hyper-parameters. The model optimization is typically performed based on the  $k$ -fold cross-validation ( $k=5$  in this study) of training data [115]. The schematic of  $k$ -fold cross-validation is shown in Figure 5-7. The training dataset is split into  $k$  groups. For each group, it is treated as a testing dataset used to validate the model which is trained by the remained  $k-1$  groups. There is no optimal value of hyper-parameter that can suit all kinds of data. Therefore, the hyper-parameter optimization needs to be taken for datasets D1, D2 and D3 separately.

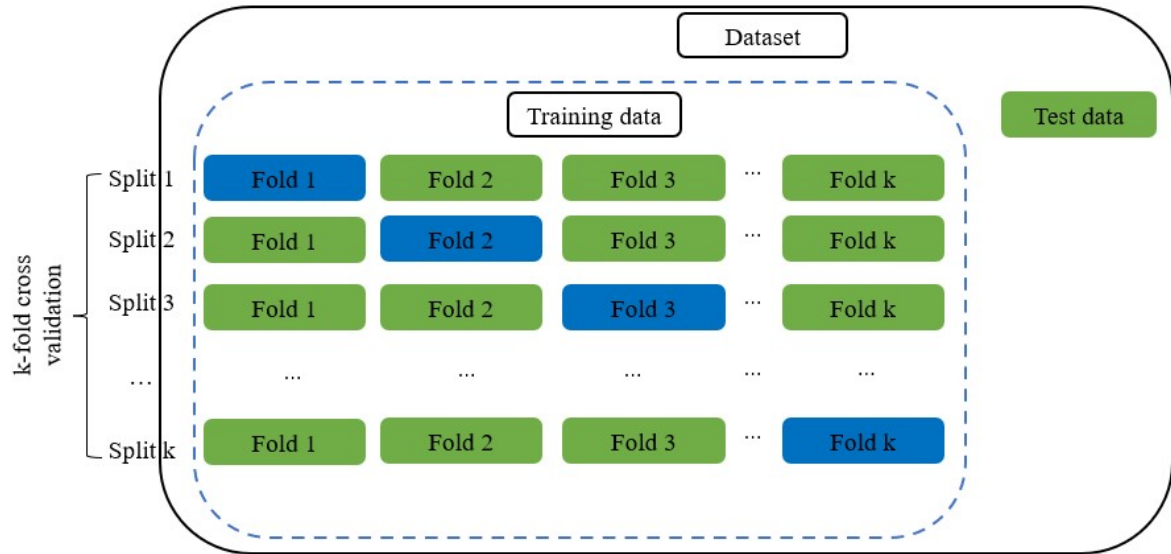


Figure 5-7 Schematic of  $k$ -fold cross validation

(1) Hyper-parameter optimization of KNNR model

For the KNNR model, the hyper-parameter is the number of neighbors. A small number of neighbors indicates that the results will have low bias but high variance, and a large number of neighbors indicates that the results will have low variance but high bias. The correlation between number of neighbors and MAE values are shown in Figure 5-8. In our case, the lowest MAE value always occurs when the number of neighbors is 2.

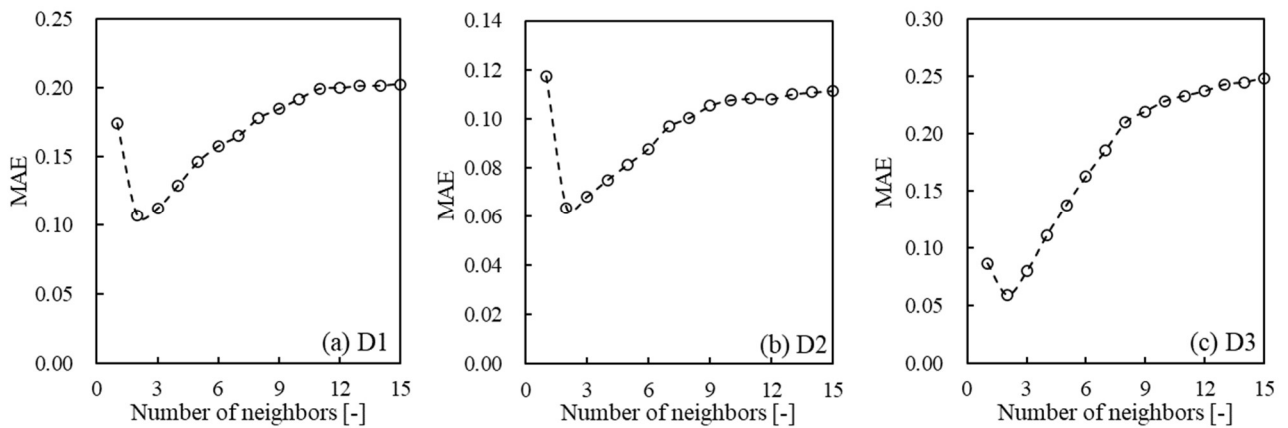


Figure 5-8 MAE values with different number of neighbors

(2) Hyper-parameter optimization of SVR model

For the SVR model with RBF kernel, the hyper-parameters include the regularization parameter  $C$  and the kernel parameter  $gamma$ . The default value of  $C$  is 1. A higher value of  $C$  indicates lower tolerance of residual error but it is prone to an overfitting phenomenon, and a higher value of  $C$  indicates a less risk of overfitting but higher tolerance of residual error. The  $gamma$  decides how much curvature in a decision boundary. A higher  $gamma$  means more curvatures, and a lower  $gamma$  indicates a flatter decision boundary. To show the relationship between hyper-parameters and model performance,  $C$  and  $gamma$  were adjusted from 0.0001 to 10000, respectively. The MAE values calculated for the datasets D1, D2 and D3 are listed in Table 5-1, Table 5-2 and Table 5-3, respectively. As shown in Table 5-1, for the dataset D1, the minimum MAE value is obtained when  $gamma$  equals to 0.1 and  $C$  is equal to or larger than 100. To avoid overfitting, a lower  $C$  value (i.e.,  $C = 100$ ) is selected. Similarly, the hyper-parameters are selected as  $gamma = 0.01$  and  $C=1000$  for the dataset D2, as  $gamma = 0.01$  and  $C = 10000$  for the dataset D3.

Table 5-1 MAE of the dataset D1

$gamma \backslash C$	0.0001	0.001	0.01	0.1	1	10	100	1000	10000
0.0001	0.448	0.448	0.448	0.448	0.445	0.419	0.205	0.093	0.092
0.001	0.448	0.448	0.448	0.445	0.419	0.206	0.093	0.091	0.074
0.01	0.448	0.448	0.445	0.419	0.207	0.090	0.073	0.059	0.057
0.1	0.448	0.446	0.423	0.228	0.078	0.059	<b>0.057</b>	0.057	0.057
1	0.447	0.440	0.371	0.111	0.059	0.059	0.059	0.059	0.059
10	0.448	0.447	0.434	0.320	0.173	0.173	0.173	0.173	0.173
100	0.448	0.448	0.449	0.450	0.456	0.456	0.456	0.456	0.456
1000	0.448	0.448	0.449	0.450	0.458	0.458	0.458	0.458	0.458
10000	0.448	0.448	0.449	0.450	0.458	0.458	0.458	0.458	0.458

Table 5-2 MAE of the dataset D2

$gamma \backslash C$	0.0001	0.001	0.01	0.1	1	10	100	1000	10000
0.0001	0.237	0.237	0.237	0.237	0.234	0.211	0.095	0.061	0.059
0.001	0.237	0.237	0.237	0.235	0.212	0.095	0.061	0.058	0.054
0.01	0.237	0.237	0.235	0.212	0.095	0.059	0.054	<b>0.050</b>	0.050
0.1	0.237	0.235	0.215	0.104	0.057	0.051	0.051	0.051	0.051

<b>1</b>	0.236	0.230	0.170	0.069	0.060	0.060	0.060	0.060	0.060
<b>10</b>	0.237	0.236	0.225	0.147	0.110	0.110	0.110	0.110	0.110
<b>100</b>	0.237	0.237	0.237	0.237	0.236	0.236	0.236	0.236	0.236
<b>1000</b>	0.237	0.237	0.237	0.237	0.237	0.237	0.237	0.237	0.237
<b>10000</b>	0.237	0.237	0.237	0.237	0.237	0.237	0.237	0.237	0.237

Table 5-3 MAE of the dataset D3

<b>gamma \ C</b>	<b>0.0001</b>	<b>0.001</b>	<b>0.01</b>	<b>0.1</b>	<b>1</b>	<b>10</b>	<b>100</b>	<b>1000</b>	<b>10000</b>
<b>0.0001</b>	0.521	0.521	0.521	0.520	0.517	0.484	0.236	0.121	0.117
<b>0.001</b>	0.521	0.521	0.520	0.517	0.484	0.237	0.121	0.113	0.085
<b>0.01</b>	0.521	0.520	0.517	0.484	0.239	0.118	0.087	0.066	<b>0.064</b>
<b>0.1</b>	0.520	0.517	0.489	0.263	0.100	0.070	0.065	0.065	0.065
<b>1</b>	0.520	0.510	0.425	0.120	0.066	0.066	0.066	0.066	0.066
<b>10</b>	0.520	0.519	0.504	0.382	0.182	0.182	0.182	0.182	0.182
<b>100</b>	0.521	0.521	0.521	0.521	0.521	0.521	0.521	0.521	0.521
<b>1000</b>	0.521	0.521	0.521	0.521	0.524	0.524	0.524	0.524	0.524
<b>10000</b>	0.521	0.521	0.521	0.521	0.524	0.524	0.524	0.524	0.524

### (3) Hyper-parameter optimization of RFR, ETR, GBR and XGBR models

The optimizations of the RFR, ETR, GBR and XGBR models are discussed together. For these four models, the number of estimators and the maximum depth of estimators are two main hyper-parameters. In this subsection, both the individual and combined effects of these two hyper-parameters on model accuracy are investigated.

To study the individual effect of number of estimators, the number of estimators is varying from 1 to 200 and for each estimator the nodes are split until all leaves are pure or until the number of samples in all leaves are less than 1. Figure 5-9 illustrates the correlation between the number of estimators and MAE values. As shown in this figure, the number of estimators has a neglectable effect on the RFR and ETR models, while it has a significant effect on the GBR and XGBR models. In particular, the MAE value of GBR model decreases rapidly from 0.38 to 0.013 as the number of estimators increases from 2 to 50, and then it is almost not changed as the number of estimators further increases from 50 to 200. Similar to the GBR model, for the XGBR model, a rapid descent (from 1.33 to 0.009) can be observed in the MAE value as the number of estimators increases from 2 to 20.

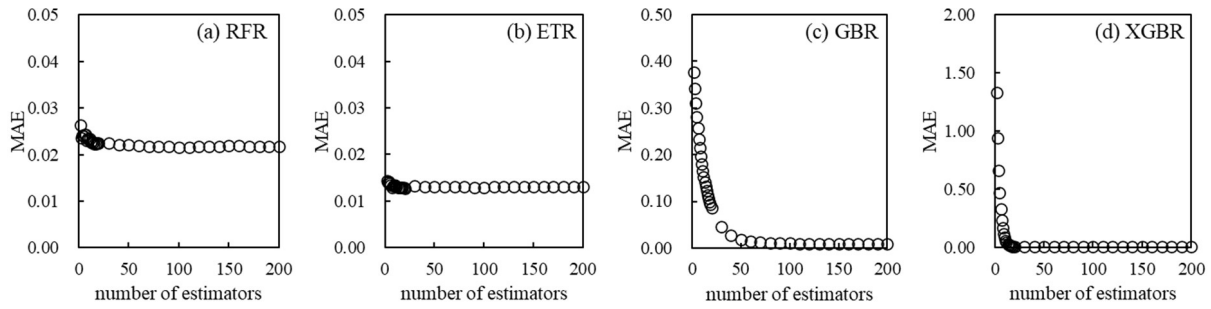


Figure 5-9 Correlations between the number of estimators and MAE values

To study the individual effect of the maximum depth of estimators, the maximum depth of estimators is increased from 2 to 15 and the number of estimators is set as 100. Figure 5-10 illustrates the correlation between the maximum depth of estimators and MAE values. As shown in this figure, the maximum depth has no obvious effect on the GBR and XGBR models but it has a large impact on both the RFR and ETR models. In particular, the MAE value of RFR model decreases from 0.17 to 0.02 when the maximum depth of estimators increases from 2 to 6, and then it is not changed as the maximum depth further increases from 6 to 15. A similar trend can be observed in the ETR model.

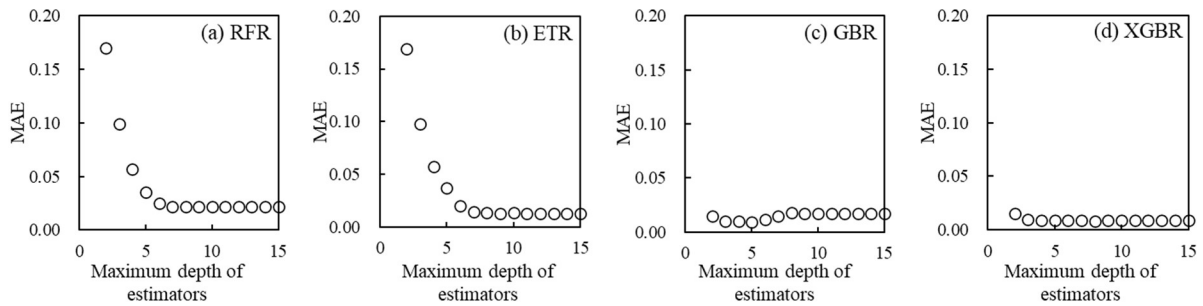


Figure 5-10 Correlations between the maximum depth of estimators and MAE values

To further determine the optimal hyper-parameters of the RFR, ETR, GBR and XGBR models, 33,600 simulations were taken by considering the combined effects of number of estimators and maximum depth of estimators. The optimized values of hyper-parameters are listed in Table 5-4. These parameters are used for further model comparison under different dataset sizes.

Table 5-4 Optimized hyper-parameters of the RFR, ETR, GBR and XGBR models

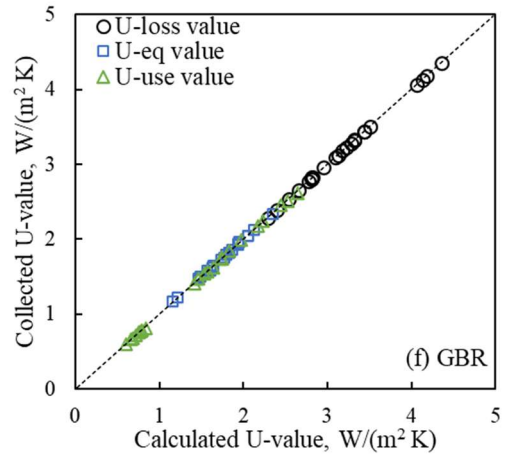
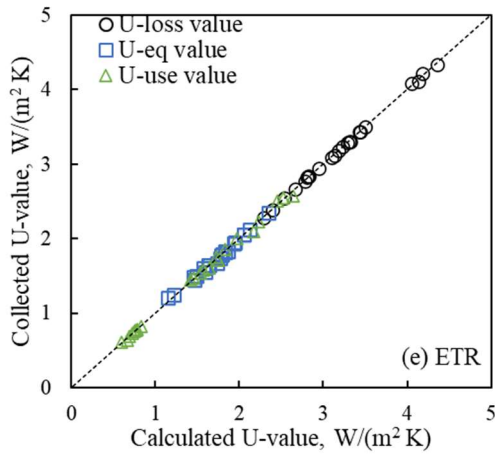
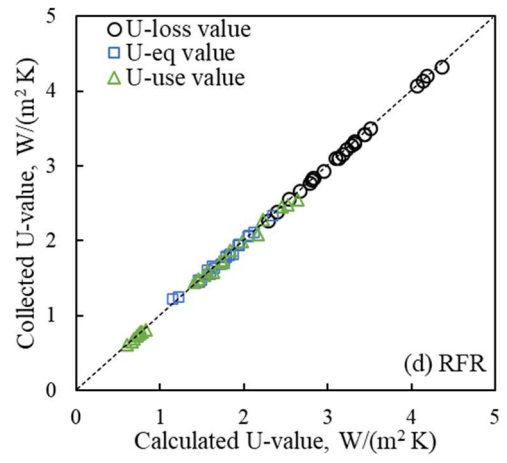
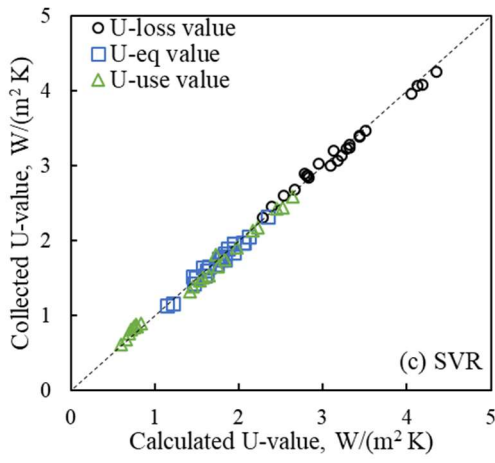
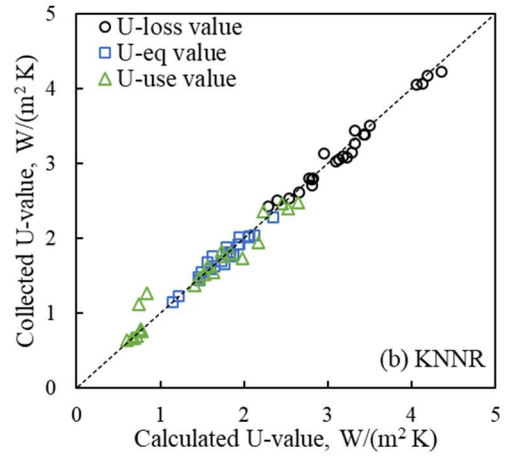
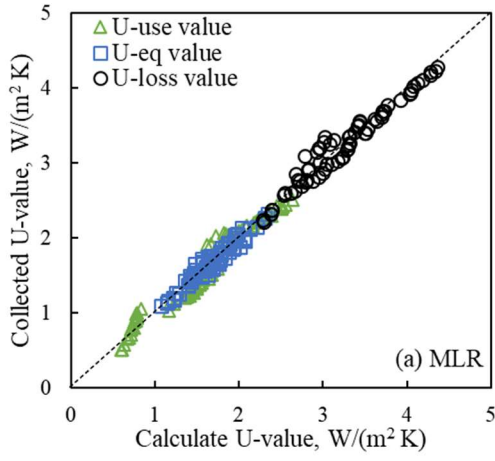
Hyper-parameter	Range	Optimized values of hyper-parameters
-----------------	-------	--------------------------------------

			<b>Dataset D1</b>	<b>Dataset D2</b>	<b>Dataset D3</b>
RFR	Number of estimators	(1, 200)	113	118	190
	Maximum depth of estimators	(2, 15)	8	9	9
ETR	Number of estimators	(1, 200)	21	46	121
	Maximum depth of estimators	(2, 15)	15	11	11
GBR	Number of estimators	(1, 200)	200	200	154
	Maximum depth of estimators	(2, 15)	5	4	4
XGBR	Number of estimators	(1, 200)	200	140	140
	Max depth of estimators	(2, 15)	8	2	3

## 5.4 Results

### 5.4.1 Comparison of different regression models

In this section, the performances of different regression models are compared. Figure 5-11 shows the scatter plots of the U-values calculated by the MLR, KNNR, SVR, RFR, ETR, GBR and XGBR models. If scatter points appear closer to the dash line, this indicates that the model has a better performance. Based on the comparison, it can be found that the points generated by the SVR model distribute more concentrated around the dash line than the MLR and KNNR models. This can be explained by the fact that the MLR model has a limitation in characterizing nonlinear relationships and the KNNR model cannot work well with high dimensionality. For four ensembled methods (i.e., the RFR, ETR, GBR and XGBR models), it is obvious that they give better results than other three models (i.e., the MLR, SVR, KNNR model). Moreover, it can be observed that the GBR and XGBR models perform slightly better than the RFR and ETR models as almost all of their generated points are on the diagonal.





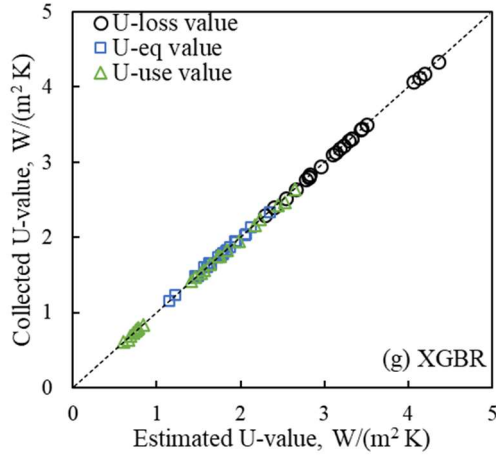
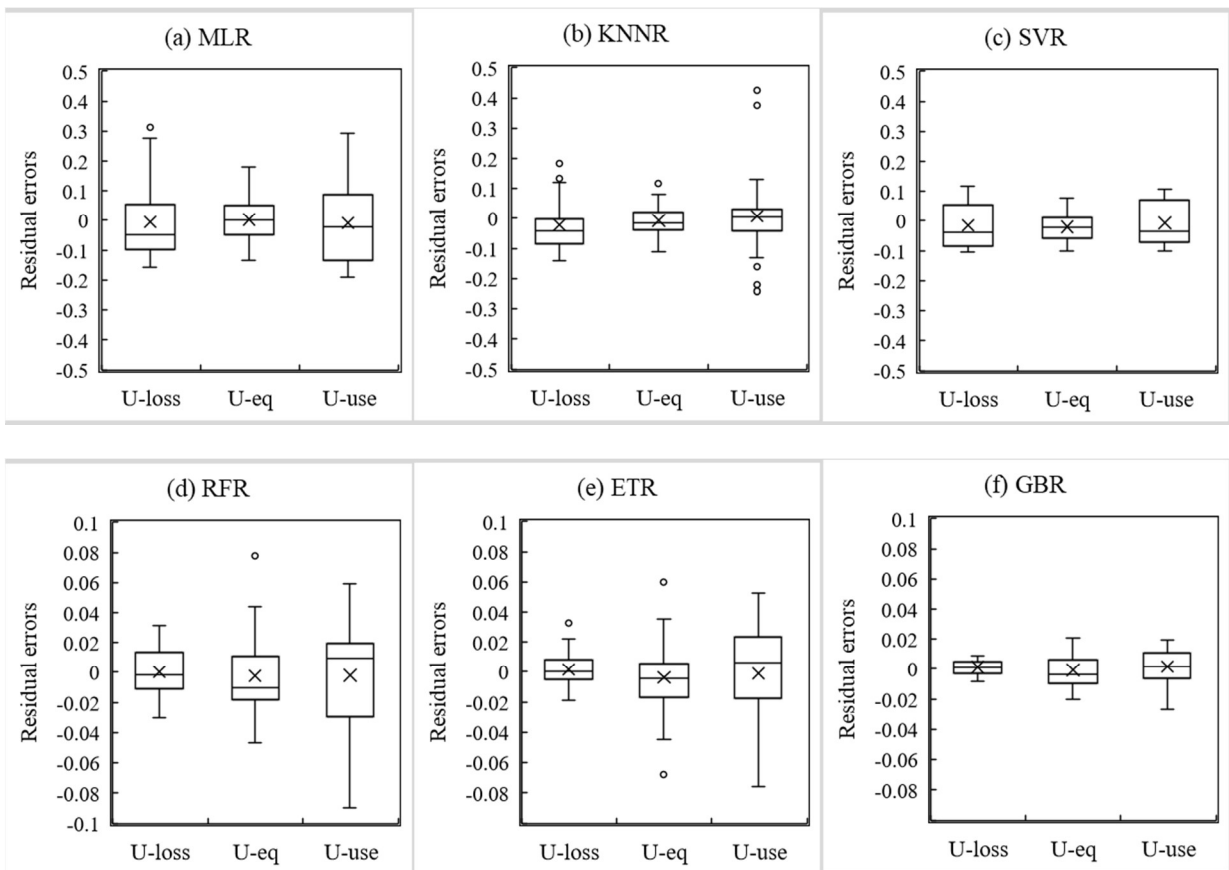


Figure 5-11 Scatter plots of the calculated U-values

Figure 5-12 gives the boxplots of residual errors produced by each model. As shown in this figure, the residual errors produced by the GBR model are most concentrated around zero, followed by the XGBR model, the ETR model, the RFR model and the SVR model. In particular, the maximum error is only 0.027 for the GBR model, and it reaches 0.33 for the MLR model.



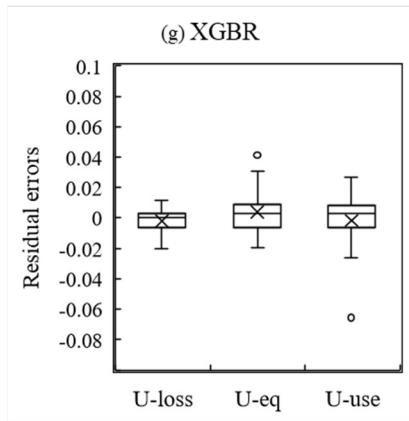


Figure 5-12 Boxplots of error residuals produced by different models

Table 5-5 shows the performance of the MLR, KNNR, SVR, RFR, ETR, GBR and XGBR models in terms of different evaluation indicators including MAE, RMSE, NMAE, NRMSE and  $R^2$ . The results are consistent with the observations in Figure 5-11 and Figure 5-12. The GBR model has lower values of MAE, RMSE, NAME, NRMSE and a higher value of  $R^2$  compared to the other six models, which indicates the GBR model has the best performance.

Table 5-5 Model performance in terms of MAE, RMSE, NMAE, NRMSE and  $R^2$

Models	U-values	MAE	RMSE	NMAE	NRMSE	$R^2$
MLR	$U_{loss}$	0.097	0.119	4.7%	5.8%	95.1%
	$U_{eq}$	0.055	0.068	4.3%	5.4%	94.0%
	$U_{use}$	0.118	0.138	5.8%	6.7%	94.9%
KNNR	$U_{loss}$	0.072	0.088	3.5%	4.2%	97.5%
	$U_{eq}$	0.048	0.062	4.0%	5.2%	95.1%
	$U_{use}$	0.094	0.150	4.6%	7.3%	94.9%
SVR	$U_{loss}$	0.064	0.138	5.8%	6.7%	94.9%
	$U_{eq}$	0.042	0.070	3.1%	3.4%	98.4%
	$U_{use}$	0.070	0.051	3.5%	4.3%	96.6%
RFR	$U_{loss}$	0.014	0.016	0.7%	0.8%	99.9%
	$U_{eq}$	0.023	0.029	1.9%	2.4%	98.9%
	$U_{use}$	0.028	0.037	1.4%	1.8%	99.7%
ETR	$U_{loss}$	0.009	0.012	0.4%	0.6%	100.0%
	$U_{eq}$	0.020	0.027	1.6%	2.3%	99.1%
	$U_{use}$	0.023	0.031	1.1%	1.5%	99.8%
GBR	$U_{loss}$	0.004	0.005	0.2%	0.2%	100.0%
	$U_{eq}$	0.009	0.010	0.7%	0.9%	99.9%
	$U_{use}$	0.010	0.012	0.5%	0.6%	100.0%
XGBR	$U_{loss}$	0.006	0.008	0.3%	0.4%	100.0%

$U_{eq}$	0.011	0.015	0.9%	1.2%	99.7%
$U_{use}$	0.012	0.018	0.6%	0.9%	99.9%

#### 5.4.2 Effect of dataset size

Due to the high cost of collecting data, the size of dataset is limited in the application. In this study, nine datasets were prepared by randomly selecting a fraction of samples from the dataset D1: D1-1 (90% of D1,  $n = 22$ ), D1-2 (80% of D1,  $n = 45$ ), D1-3 (70% of D1,  $n = 67$ ), D1-4 (60% of D1,  $n = 90$ ), D1-5 (50% of D1,  $n = 112$ ), D1-6 (40% of D1,  $n = 135$ ), D1-7 (30% of D1,  $n = 157$ ), D1-8 (20% of D1,  $n = 180$ ), D1-9 (10% of D1,  $n = 202$ ). Each dataset is then split into 10% for training and 90% for validation. For each dataset size, data samples were randomly selected for 100 times. The average MAE value over 100 times for each dataset size is calculated and presented in Figure 5-13. As shown in Figure 5-13, for the MLR model, the dataset size has a small effect on the average MAE value. For the KNNR, SVR, RFR, ETR, GBR and XGBR models, an obvious decrease can be observed in the average MAE value along with the increase of dataset size. In particular, as the dataset size increases from 22 to 202, the decreasing rate is largest for the GBR model (95.7%), followed by the XGBR model (91.9%), the ETR model (91.3%), the RFR model (89.5%), the KNNR model (66.1%) and the SVR model (44.8%).

Furthermore, it can be concluded that it is difficult to select a single model that performs well under different dataset size. Specifically, when the dataset sizes are 22, 45, 67, 90, 112, 135, 157, 180 and 202, the models that obtain the smallest average MAE value are the SVR model, the XGBR model, the XGBR model, the XGBR model, the XGBR model, the XGBR model, the XGBR model, the GBR model and the GBR model, respectively. Therefore, it is necessary to take the dataset size into consideration of selecting an appropriate model.

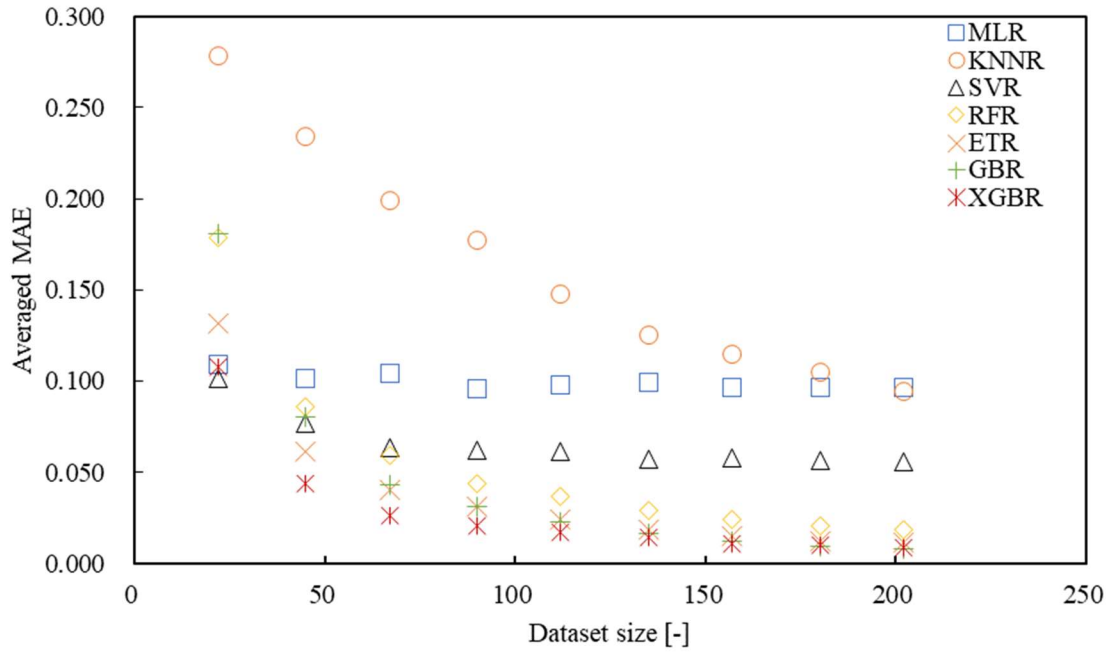


Figure 5-13 Effect of dataset sizes on model performance

## 5.5 Conclusions

The U-values of supply-air double windows are related with boundary conditions (i.e., the inside and outside convective heat transfer coefficients, indoor and outdoor air temperatures). It is therefore necessary to calculate dynamic U-values. Although the CFD simulation can provide accurate U-value, it requires engineering knowledge and expensive computational resources. Therefore, it is still difficult for users to make a fast decision in the early design stage. To solve this challenge, seven regression models (i.e., MLR, KNNR, SVR, RFR, ETR, GBR and XGBR) with high computational efficiency are utilized to calculate the U-values, and their performance are compared in terms of different evaluation indicators. Also, the effects of dataset sizes on the model performance are analyzed and discussed.

The main results are summarized as follows:

- (1) The train/test splitting ratio has significant effects on the KNNR, SVR, RFR, ETR, GBR and XGBR models, while it has an insignificant effect on the MLR model.
- (2) The optimization of the SVR, KNN, RFR, ETR, GBR and XGBR models by tuning hyper-parameters are necessary to improve the model accuracy.
- (3) The RFR, ETR, GBR and XGR models performs better than the MLR model with lower MASE, RMSE, NMAE, NRMSE and higher  $R^2$ . This shows their application potential in calculating dynamic U-values as an easy-to-use tool. In addition, the GBR model performs slightly better than the RFR, ETR and GBR models.
- (4) The dataset size has a great impact on the performance of the SVR, KNN, RFR, ETR, GBR and XGBR models. This indicates that it is necessary to consider the dataset size in the selection of an appropriate regression model.

# **6 Inverse Identification Framework for Renovated Supply-air Double Windows — A Case Study**

## 6.1 Introduction

To achieve energy goals, the performance requirements (i.e., requirement of minimum U-value) for building elements such as windows have been set for different countries and regions according to local climate conditions. For example, in France the requirement of window minimum U-value is  $1.9 \text{ W}/(\text{m}^2 \text{ K})$  [11].

The window performance requirement can help users to fast choose a new window since the U-value of a new constructed window is often given by manufactures. While for a renovated supply-air double window, its U-value is not given and its performance is highly related with boundary conditional parameters and window renovation design parameters. Compared to giving a performance requirement for renovated windows, providing requirements for renovation design parameters is more straightforward which can help users to quickly determine possible renovation solutions. The renovation design parameters can be the thermal/optical properties of the secondary window or the supplied air flow rate. To determine requirements for renovation design parameters, an inverse identification framework for renovated supply-air double windows is proposed in this chapter. More specifically, the purpose of the proposed framework is to find the upper or lower boundary constraints of window renovation design parameters. The search of upper or lower boundary constraints can be treated as an optimization problem. Various optimization algorithms have been proposed to solve engineering problems [117–119]. In this study, the particle swarm optimization (PSO) algorithm is applied due to its simplicity.

This chapter includes four sections. Section 6.1 introduces the purpose of proposing an inverse identification framework. Section 6.2 presents the procedure of the inverse identification framework and the PSO algorithm. Sections 6.3 gives a case study and discusses results. Section 6.4 concludes this chapter.

## 6.2 Inverse identification framework

The basic idea of inverse identification framework is to inversely determine the unknown constraints of renovation design parameters by continuously reducing the difference between the calculated U-value of renovated supply-air double window and the standard of the window minimum U-value. The process of inverse identification is shown in Figure 6-1. It starts with an initial design parameter. With the given parameter, the U-value can be calculated by running the established numerical model or the trained regression model. Then the calculated U-value is used to check whether the objective function (Eq. (6-1)) satisfy the convergence criteria. If yes, the inverse identification process is ended. Otherwise, the optimization algorithm (i.e., PSO algorithm in this study) updates the design variable and the inverse identification process continues until the objective function reaches the convergence criteria.

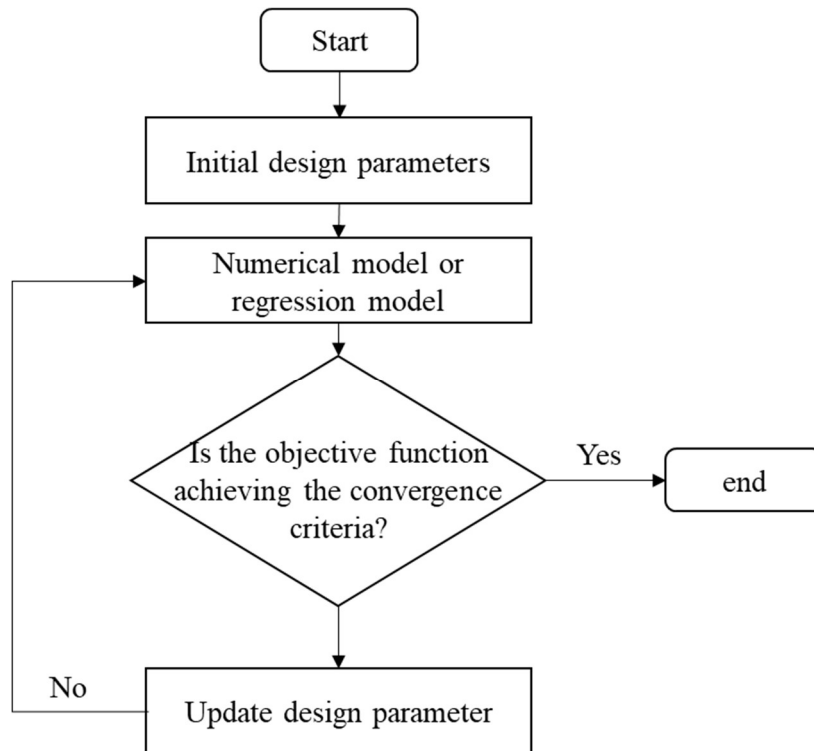


Figure 6-1 Flowchart of the inverse identification process

The objective function is a function of window design parameters, as expressed as Eq. (6-1):

$$f(\delta) = \min_{\theta} (F(\delta) - R)^2 \quad (6-1)$$



Where,  $\delta$  is design variable;  $\theta$  represents the design domain which is preset by users;  $F$  is the established numerical model or trained regression model;  $R$  is the standard of minimum U-value, W/(m<sup>2</sup> K).

Except from design parameters, the U-value of a given supply-air double window is also affected by boundary conditional parameters. To account for the uncertainties of boundary conditional parameters, the Monte Carlo sampling [120] is utilized in this study to generate thousands of scenarios composed of uncertainties. The aim of inverse identification is then set to get the constraints of design parameters that allow the renovated window satisfy the requirement under all of the generated scenarios. The process of the inverse identification with considering uncertainties is shown in Figure 6-2.

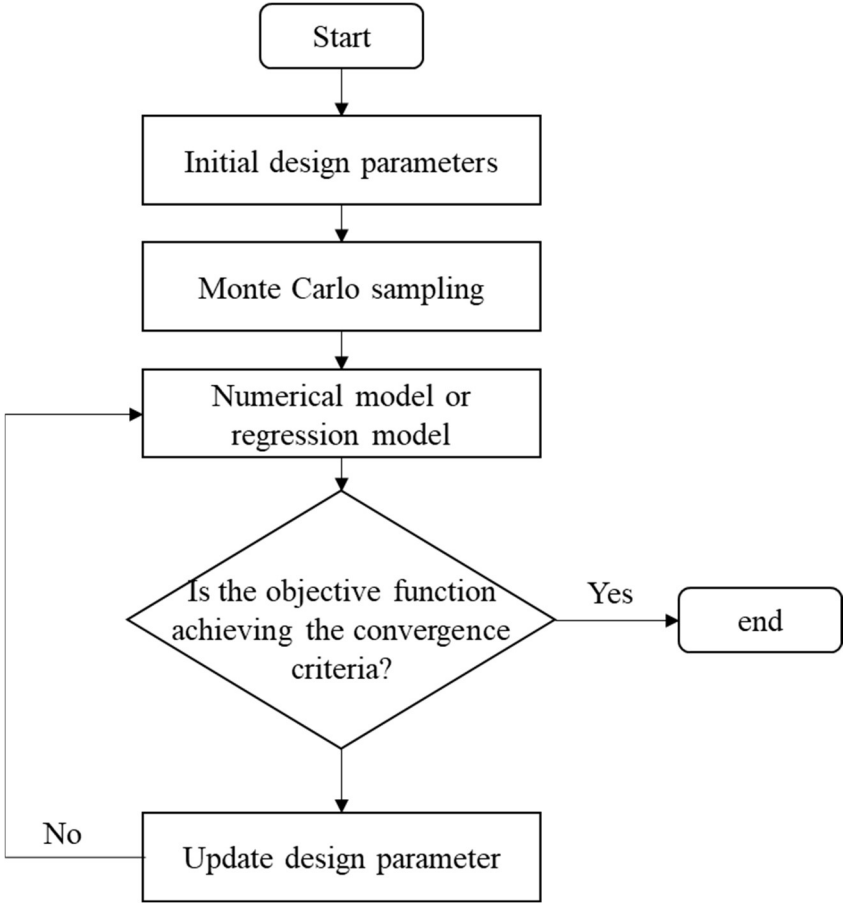


Figure 6-2 Flowchart of the inverse identification process with considering uncertainties

The objective function can be expressed as:

$$f_{uncertainty}(\delta) = \min_{\theta} \left[ (n_{F(\delta, \xi_i) < R} - n)^2 + \sum_{i=1}^n (F(\delta, \xi_i) - R)^2 \right] \quad (6-2)$$

Where,  $n$  is the number of uncertain scenarios and  $\xi_i$  is the  $i$ th uncertain scenario.

In order to reduce the computational cost for calculating U-values under thousands of scenarios, a model with high computational efficiency is required as a surrogate model to replace the forward numerical model.

### 6.2.1 PSO algorithm

The PSO algorithm exploits the idea of cooperative behaviors of birds for searching food [119]. During the searching process, each bird shares its position and changes its location according to its own best position (the closed position to the food) and the best position shared with the entire swarm.

The fundamental steps of the PSO method are depicted in Figure 6-3:

(a) Preset the number of particles and maximum number of iterations, and initialize positions and velocities of particles randomly.

(b) Evaluate each particle's fitness by calculating the fitness value of objective function.

(c) Update the local best ( $pbest_k^i$ ) value by comparing the previous best value of each particle to its current fitness value, and update the global best ( $gbest_k^i$ ) value by comparing the previous best value of swarm to its current fitness value.

(d) Update particle's position and velocity according to the Eq. (6-3) and Eq. (6-4), respectively.

$$v_{k+1}^i = \omega v_k^i + c_1 \text{rand}_1 (pbest_k^i - x_k^i) + c_2 \text{rand}_2 (gbest_k - x_k^i) \quad (6-3)$$

$$x_{k+1}^i = x_k^i + v_{k+1}^i \quad (6-4)$$

Where,  $v_k^i$  and  $x_k^i$  are the velocity and position of the  $i$ th particle in  $k$ th iteration, respectively;  $c_1$  and  $c_2$  are learning factors;  $\omega$  is an inertia factor;  $\text{rand}_1$  and  $\text{rand}_2$  are two random numbers in the range of 0-1.

(e) The process (b)-(d) are repeated until the fitness value meet the termination criteria or the number of iterations reaches the preset maximum number.

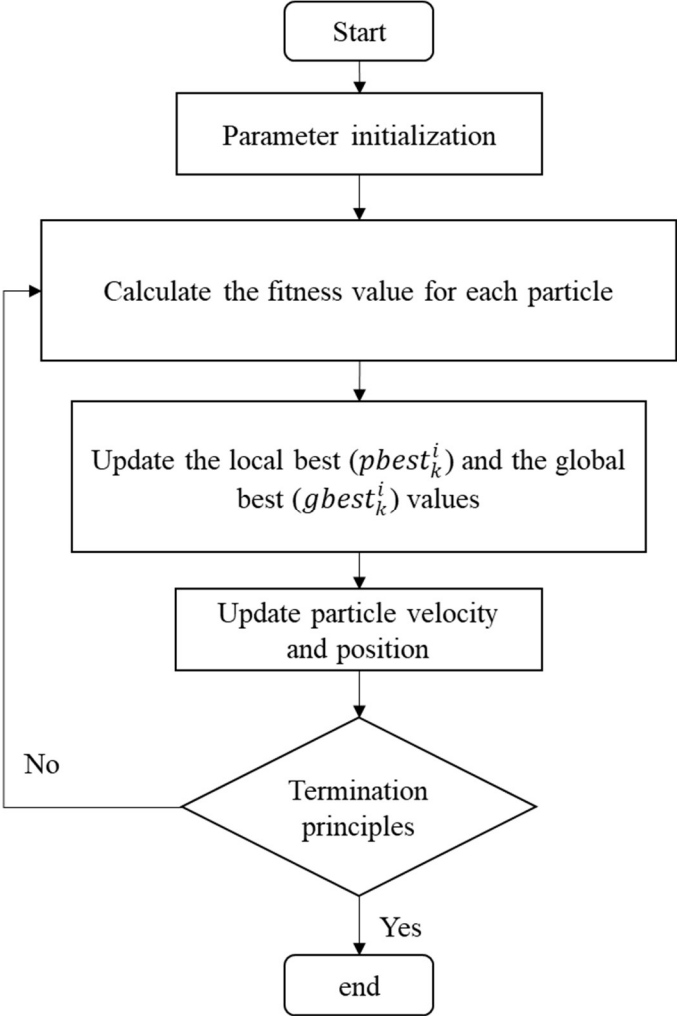


Figure 6-3 Flowchart of PSO algorithm

## 6.3 Case study

In this chapter, a case study about how to renovate a single-glazed window into a supply-air double window is taken to demonstrate the proposed inverse identification framework. The airflow of supply-air window is driven by forced mechanics. The objective of this case study is to get the constraint of air flow rate that allows the renovated supply-air double window to meet the window performance requirement. The minimum requirement of window U-value in France is  $1.9 \text{ W}/(\text{m}^2 \text{ K})$ . Note that all of the simulations were taken based on the platform Python 3.7.

### 6.3.1 Description of the case study

#### (1) Window description

The renovated supply-air window is composed of two single-glazed windows with a size of  $0.888 \text{ m} * 0.888 \text{ m}$ . The thermal and optical properties of the single-glazed window are shown in Table 4-1.

#### (2) Regression model

The GBR model trained in Chapter V is selected due to its high accuracy and high computational efficiency. The optimization and validation of GBR model have been presented in Chapter V.

#### (3) Scenario setting and uncertainty description

According to the weather data collected by the weather station located in ENTPE, Vaulx-en-Velin, France (Latitude:  $45^{\circ}46'43'' \text{ N}$ , Longitude:  $4^{\circ}55'21'' \text{ E}$ ), the average air temperature in winter (from November to March) is around  $5^{\circ}\text{C}$ . The outdoor air temperature is then set as  $5^{\circ}\text{C}$ . The indoor air temperature is set as  $20^{\circ}\text{C}$ . Referred to standards, the inside air convective heat transfer coefficient is assumed as  $3.6 \text{ W}/(\text{m}^2 \text{ K})$ , and the outside convective heat transfer coefficient is assumed as  $20 \text{ W}/(\text{m}^2 \text{ K})$ . The uncertainty of parameters (i.e., outdoor air temperature, indoor air temperature, interior convective heat transfer coefficient and exterior convective heat transfer coefficient) is expressed as a normal distribution  $N(\mu, \sigma^2)$ .

### 6.3.2 Results and discussions

### (1) Impacts of sampling size on the inverse identification result

Under scenarios with uncertainties, the Monte Carlo sampling size is a critical parameter that influences the computational time. A larger sampling size leads to a longer computational time. It is therefore necessary to find a minimum sampling size. In this study, different sampling sizes ( $n = 100, 500, 1000, 1500, 2000$ ) are utilized. As shown in Figure 6-4, the lower boundary constraint of air flow rate increases from 2.3 g/s to 3.0 g/s as the sampling size increases from 100 to 1000, and then it is not changed as the sampling size further increases from 1000 to 2000. This result indicates that the sampling size should be equal to or larger than 1000 to achieve the stability of the results.

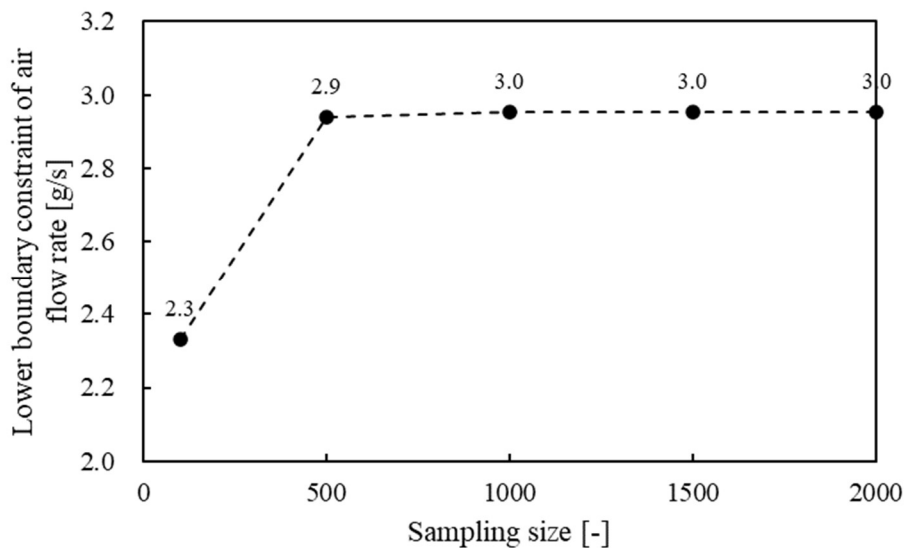


Figure 6-4 Correlation between the sampling size and inverse identification result

### (2) Inverse identification results with and without considering uncertainties

In this subsection, the constraints of air flow rate with and without considering uncertainties are compared. As shown in Table 6-1, the lower boundary constraint of air flow rate in the deterministic scenario is 1.4 g/s. Compared to the deterministic scenario, the value of lower boundary constraint is increased to 3.0 g/s in the uncertain scenarios. This indicates that considering uncertainties in the inverse identification framework can improve the robustness of renovated supply-air double window in response to changes in environmental conditions. It should be mentioned that if the lower boundary constraint of air flow rate is larger

than the fresh air requirement, a further attention should be put on other design parameters such as the U-value of secondary window to find proper renovation solutions.

*Table 6-1 Constraints of air flow rate*

Scenario	Constraint of air flow rate, g/s
Deterministic scenario	>1.4
Uncertainty scenarios	>3.0

(3) Inverse identification results with different uncertainty magnitudes

In this subsection, the impacts of uncertainty magnitudes on the inverse identification results are analyzed. Specifically, the standard deviation of uncertainty distribution is changed from 0 to 1 (0 means the parameter is with no uncertainty). The identified lower boundary constraints of air flow rate are presented in Figure 6-5. As shown in this figure, the value of lower boundary constraint increases as the standard deviation of uncertainty distributions increases.

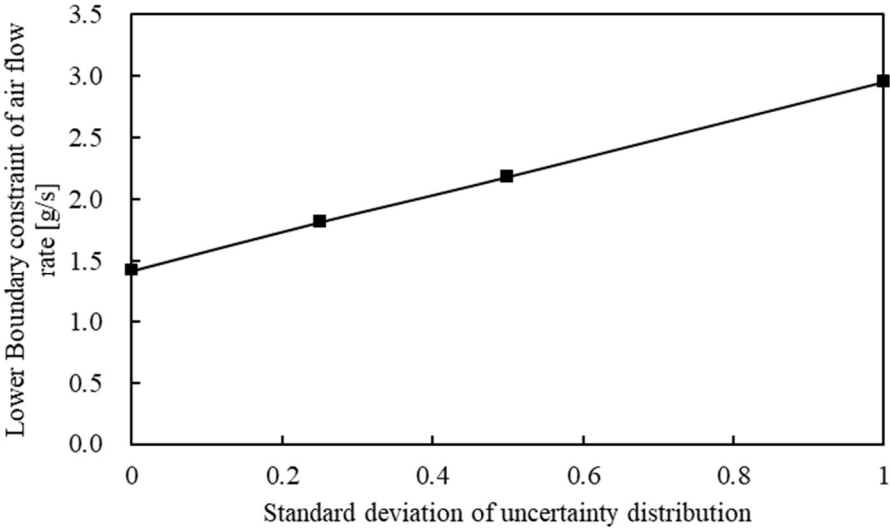


*Figure 6-5 Impact of the uncertainty magnitude on the inverse identification result*

## 6.4 Conclusions

In order to achieve building energy efficiency goals, specific requirements for window performance have been set in different countries. To satisfy the window performance requirement, there should be upper boundary or lower boundary constraints of window renovation design parameters (e.g., U-value of secondary window and supplied air flow rate). Identification of such constraints can help users to quickly determine possible solutions in the renovation work and facilitate the renovation work. To do this, this chapter propose an inverse identification framework for renovated supply-air double windows.

To demonstrate the proposed inverse identification framework, a case study of renovating a single-glazed window into a supply-air double window was conducted. From the results, it was found that the lower boundary constraint of air flow rate in the uncertain scenarios was higher than that in the deterministic scenario. This means that the inverse identification framework composed of uncertainties can help enhance the robustness of renovated supply-air double windows in response to changes in boundary conditions. Also, the influence of uncertainty magnitude on the inverse identification result was investigated, and a larger value of lower boundary constraints was found for a greater uncertainty magnitude.

It should be mentioned that, the proposed framework is a methodology demonstration. The uncertainty of boundary conditions needs to be further experimentally determined. Also, this study only considers the minimum requirement of U-value. Another important window performance indicator is solar heat gain coefficient (SHGC). In future studies, both the requirements of U-value and SHGC-value are needed to be considered. Furthermore, more uncertainty sources (e.g., uncertainties of models) can be considered in future study.

## **7 General Conclusions**



## 7.1 Conclusions

This dissertation represents the research works of U-values of supply-air double windows from different aspects. The aims of research works include proposing an adjusted GHB method, conducting a comprehensive parametric study, determining a new dynamic U-value calculation and proposing an inverse regulation framework.

For supply-air double windows, there is no standardized GHB method. In particular, the exist of air flow channel adds difficulties in accurately testing U-values of supply-air double window. To address this research gap, we proposed an adjusted GHB method by improving the GHB set up and the calibration/testing process. Based on the conventional GHB method and adjusted GHB method, the U-values of nine window configurations are tested and compared. The experimental results show that compared to the U-value of the single-glazed window, the U-values of closed-air double windows (i.e., DW1, DW2 and DW3) are reduced by 56.7%-75.2%, and the U-values of supply-air double windows (i.e., VW1, VW2 and VW3) are reduced by 64.6%-85.2%. Also, the center-of-glass U-value which is widely used in current building code is compared with the total window U-value. The results show that the deviations are in the range of 19.0%-45.5% for different window configurations.

Based on the experimental data, a three-dimensional CFD model is validated to perform simulations. Then a comprehensive parametric study is performed to study impacts of virous parameters on U-values of three supply-air double windows (i.e., VW1, VW2 and VW3). The studied parameters include the window area, thermal conductivity of internal/external window frame, air flow rate, inside/outside convective heat transfer coefficient, and indoor/outdoor air temperatures. Furthermore, the impacts of different parameters on U-values are compared based on the sensitivity analysis. The results of parametric study and sensitivity analysis are summarized in Table 7-1. In the table, the color is used to distinguish the positive correlation, negative correlation and non-monotonic correlation between parameters and U-value (i.e., “green”: positive correlation; “white”: negative correlation; “gray”: non-monotonic), and the number of “+” indicate the level of sensitivity.

Table 7-1 Correlations between the studied parameters and U-values

	VW1			VW2			VW3		
	$U_{loss}$	$U_{use}$	$U_{eq}$	$U_{loss}$	$U_{use}$	$U_{eq}$	$U_{loss}$	$U_{use}$	$U_{eq}$
Air flow rate, kg/s	+++++	+++++	+++++	+++++	+++++	+++++	+++++	+++++	+++++
Thermal conductivity of internal window frame, W/(m K)	+++	++	+	++++	+++	++	+++++	++++	++++
Thermal conductivity of external window frame, W/(m K)	+	+	+++	++	+	+	+	+	++
Outside convective heat transfer coefficient, W/(m <sup>2</sup> K)	++++	+++	++++	+++	++	++++	+++	++	++++
Inside convective heat transfer coefficient, W/(m <sup>2</sup> K)	+++++	+++++	+++++	+++++	++++	++++	+++++	++++	+++
Outdoor temperature, °C	++	+++	++	+	++++	+++	++	++++	++++
Indoor temperature, °C	++++	++++	+++	++++	++++	+++	++++	++++	+
Window size, m <sup>2</sup>	+++++	+++++	+++++	+++++	+++++	+++++	+++++	+++++	++++
Emissivity	\	\	\	\	\	\	+++	+++	+++++

Considering that the CFD model requires engineering knowledge and expensive computational cost, a new calculation method is needed for users to quickly determine dynamic U-values under different boundary conditions. In this dissertation, different regression models (i.e., MLR, SVR, KNN, RFR, ETR, GBR and XGBR models) are analyzed and compared. Also, the effect of dataset sizes on the model performances are investigated. The results show that among the analyzed regression models, the GBR model has the best performance in our cases. In particular, the MAE values of GBR model are lower than 0.01 for determining the  $U_{loss}$  value,  $U_{use}$  value and  $U_{eq}$  value.

The performance requirements of renovated windows have been set in different countries. To facilitate the renovation work for users who want to renovate a window to a supply-air double window, a straightforward requirement for renovation design parameters such as the minimum airflow rate is required. To obtain such a requirement, we proposed an inverse identification framework with/without considering uncertainties of environmental conditions. The results show that the lower boundary constraint of air flow rate is higher when the

uncertainties of boundary conditions are considered. This implies the consideration of uncertainties in the inverse identification framework can improve the robustness of renovated window performance.

## 7.2 Outlook and perspective

The supply-air double window attracts our attention due to the fact that it has a large potential to improve building energy performance and also it is easy to be renovated from an old window without damaging the building exterior appearance. Throughout this dissertation, investigations of U-values of supply-air double window were carried out from different aspects. Based on this study, here are some suggestions for future explorations.

(1) Except from the U-value, the solar heat gain coefficient (SHGC) is also an important indicator to reflect the window performance. A comprehensive measurement is expected for testing the SHGC value of supply-air double windows and comparing supply-air double windows with conventional windows. Also, the impact of window configurations and boundary conditions on the SHGC value of supply-air double windows need a further experimental/numerical study.

(2) For the proposed inverse identification framework, an experimental calibration of the uncertainty magnitude of the boundary conditions is required in future studies. Also, more uncertainty sources (such as the uncertainty of models) should be taken into consideration. Furthermore, more window performance requirements such as requirement of SHGC value should be considered simultaneously to identify the requirements for window renovation design parameters. Moreover, other optimization methods can be applied and compared to improve the computational efficiency of inverse identification process.

## Reference

- [1] Intergovernmental Panel on Climate Change, Global warming of 1.5°C, 2019.
- [2] P. Agreement, Paris agreement, in: Report of the Conference of the Parties to the United Nations Framework Convention on Climate Change (21st Session, 2015: Paris). Retrived December, HeinOnline, 2015: p. 2017.
- [3] LTECV, Loi n° 2015-992 du 17 août 2015 relative à la Transition Énergétique pour la Croissance Verte, <https://www.legifrance.gouv.fr/>. (2015).
- [4] PACTE, Programme d'Action pour la qualité de la Construction et la Transition Énergétique, Analyse Détaillée Du Parc Résidentiel Existant, <https://www.programmepacte.fr/>. (2017).
- [5] Plan de rénovation énergétique des bâtiments, (2018) 1–5.
- [6] A. Gustavsen, B.P. Jelle, D. Arasteh, C. Kohler, State-of-the-art highly insulating window frames—Research and market review, Norges byggforskingsinstitutt, 2007.
- [7] M. Aburas, V. Soebarto, T. Williamson, R. Liang, H. Ebendorff-Heidepriem, Y. Wu, Thermochromic smart window technologies for building application: A review, *Appl Energy*. 255 (2019) 113522. <https://doi.org/10.1016/j.apenergy.2019.113522>.
- [8] M. el Mankibi, R. Cantin, A. Zoubir, Contribution to the thermal renovation of old buildings: Numerical and Experimental approach for characterizing a double window., *Energy Procedia*. 78 (2015) 2470–2475. <https://doi.org/10.1016/j.egypro.2015.11.231>.
- [9] J.L. Wright, Effective U-values and shading coefficients of preheat/supply air glazing systems, *Solar Energy Society of Canada*. (1986) 219–224.
- [10] International Standard, ISO 15099: Thermal performance of windows, doors and shading devices – Detailed calculations, (2003).
- [11] M. Coillot, Caractérisations numérique et expérimentale du comportement thermo-aéraulique d'une double-fenêtre active, Doctoral Dissertation, Université de Lyon. (2019).
- [12] F. Khalvati, A. Omidvar, Summer study on thermal performance of an exhausting airflow window in evaporatively-cooled buildings, *Appl Therm Eng*. 153 (2019) 147–158. <https://doi.org/10.1016/j.applthermaleng.2019.02.135>.
- [13] R. Greffet, Études expérimentale et numérique des performances énergétiques d'une fenêtre pariétodynamique, (2019).
- [14] I. Pérez-Grande, J. Meseguer, G. Alonso, Influence of glass properties on the performance of double-glazed facades, *Appl Therm Eng*. 25 (2005) 3163–3175. <https://doi.org/10.1016/j.applthermaleng.2005.04.004>.
- [15] J.S. Carlos, H. Corvacho, Evaluation of the performance indices of a ventilated double window through experimental and analytical procedures: Uw-values, *Energy Build*. 86 (2014) 886–897. <https://doi.org/10.1016/j.enbuild.2014.11.002>.
- [16] Y. Sun, Y. Wu, R. Wilson, A review of thermal and optical characterisation of complex window systems and their building performance prediction, *Appl Energy*. 222 (2018) 729–747. <https://doi.org/10.1016/j.apenergy.2018.03.144>.

- [17] International Standard, ISO 8990: Thermal insulation - determination of steady-state thermal transmission properties - calibrated and guarded hot box, (1994).
- [18] International Standard, ISO 8302: Thermal insulation - Determination of steady-state thermal resistance and related properties - Guarded hot plate apparatus, (1991).
- [19] International Standard, ISO 8301: Thermal insulation - Determination of steady-state thermal resistance and related properties - Heat flow meter apparatus, (1991).
- [20] International Organization for Standard, ISO 10291: Glass in building - Determination of steady-state U values (thermal transmittance) of multiple glazing - Guarded hot plate method, (1994).
- [21] International Organization for Standard, ISO 10293: Glass in building - Determination of steady-state U values (thermal transmittance) of multiple glazing - Heat flow meter method, (1997).
- [22] International Organization for Standard, ISO 12567-1: Thermal performance of windows and doors -Determination of thermal transmittance by the hot-box method - Part 1: Complete windows and doors, (2010).
- [23] N. Soares, C. Martins, M. Gonçalves, P. Santos, L.S. da Silva, J.J. Costa, Laboratory and in-situ non-destructive methods to evaluate the thermal transmittance and behavior of walls, windows, and construction elements with innovative materials: A review, *Energy Build.* 182 (2019) 88–110. <https://doi.org/10.1016/j.enbuild.2018.10.021>.
- [24] J.R. Gosselin, Q. Chen, A computational method for calculating heat transfer and airflow through a dual-airflow window, *Energy Build.* 40 (2008) 452–458. <https://doi.org/10.1016/j.enbuild.2007.03.010>.
- [25] M. Bhamjee, A. Nurick, D.M. Madyira, An experimentally validated mathematical and CFD model of a supply air window: Forced and natural flow, *Energy Build.* 57 (2013) 289–301. <https://doi.org/10.1016/j.enbuild.2012.10.043>.
- [26] L.M. Raffinsoe, Thermal Performance of Air Flow Windows — Master Thesis, Technical University of Denmark, Denmark. (2007) 157–198. <http://www.mst.dk/NR/rdonlyres/8E3E9611-803B-472B-B02A-DA523A9E0174/0/LauMasterThesis.pdf>.
- [27] R.G. Southall, M. Mcevoy, Investigations into the functioning of a supply air window in relation to solar energy as determined by experiment and simulation, *Solar Energy.* 80 (2006) 512–523. <https://doi.org/10.1016/j.solener.2005.04.016>.
- [28] F. Gloriant, P. Tittlein, A. Joulin, S. Lassue, Modeling a triple-glazed supply-air window, *Build Environ.* 84 (2015) 1–9. <https://doi.org/10.1016/j.buildenv.2014.10.017>.
- [29] W. Tao, *Numerical Heat Transfer*, 2001.
- [30] E. González-Julián, J. Xamán, N.O. Moraga, Y. Chávez, I. Zavala-Guillén, E. Simá, Annual thermal evaluation of a double pane window using glazing available in the Mexican market, *Appl Therm Eng.* 143 (2018) 100–111. <https://doi.org/10.1016/j.applthermaleng.2018.07.053>.
- [31] S. Somasundaram, A. Chong, Z. Wei, S.R. Thangavelu, Energy saving potential of low-e coating based retrofit double glazing for tropical climate, *Energy Build.* 206 (2020) 109570. <https://doi.org/10.1016/j.enbuild.2019.109570>.

- [32] O. Aydin, Determination of optimum air-layer thickness in double-pane windows, *Energy Build.* 32 (2000) 303–308. [https://doi.org/10.1016/S0378-7788\(00\)00057-8](https://doi.org/10.1016/S0378-7788(00)00057-8).
- [33] G. Michaux, R. Greffet, P. Salagnac, J. Ridoret, Modelling of an airflow window and numerical investigation of its thermal performances by comparison to conventional double and triple-glazed windows, *Appl Energy.* 242 (2019) 27–45. <https://doi.org/10.1016/j.apenergy.2019.03.029>.
- [34] T. Chow, C. Li, J.A. Clarke, Numerical prediction of water-flow glazing performance with reflective coating, *Proceedings of Building Simulation 2011: 12th Conference of International Building Performance Simulation Association.* (2011) 1127–1133.
- [35] Y. Lyu, T. Chow, J. Wang, Numerical prediction of thermal performance of liquid-flow window in different climates with anti-freeze, *Energy.* 157 (2018) 412–423. <https://doi.org/10.1016/j.energy.2018.05.140>.
- [36] D. Gstoehl, J. Stopper, S. Bertsch, D. Schwarz, Fluidised glass façade elements for an active energy transmission control, *World Engineers' Convention.* (2011).
- [37] L. Baumgärtner, R.A. Krasovsky, J. Stopper, J. von Grabe, Evaluation of a solar thermal glass façade with adjustable transparency in cold and hot climates, *Energy Procedia.* 122 (2017) 211–216. <https://doi.org/10.1016/j.egypro.2017.07.347>.
- [38] M. Gutai, A.G. Kheybari, Energy consumption of hybrid smart water-filled glass (SWFG) building envelope, *Energy Build.* 230 (2021) 110508. <https://doi.org/10.1016/j.enbuild.2020.110508>.
- [39] T. Chow, W. Liu, Warm climate performance of water-filled double-glazing with submerged heat exchanger, *Sustain Cities Soc.* 58 (2020) 102135. <https://doi.org/10.1016/j.scs.2020.102135>.
- [40] P. Sierra, J.A. Hernández, Solar heat gain coefficient of water flow glazings, *Energy Build.* 139 (2017) 133–145. <https://doi.org/10.1016/j.enbuild.2017.01.032>.
- [41] B.M. Santamaria, F. del A. Gonzalo, B.L. Aguirregabiria, J.A. Hernandez Ramos, Experimental validation of water flow glazing: Transient response in real test rooms, *Sustainability (Switzerland).* 12 (2020) 1–23. <https://doi.org/10.3390/su12145734>.
- [42] Y. Lyu, W. Liu, H. Su, X. Wu, Numerical analysis on the advantages of evacuated gap insulation of vacuum-water flow window in building energy saving under various climates, *Energy.* 175 (2019) 353–364. <https://doi.org/10.1016/j.energy.2019.03.101>.
- [43] T. Gil-Lopez, C. Gimenez-Molina, Influence of double glazing with a circulating water chamber on the thermal energy savings in buildings, *Energy Build.* 56 (2013) 56–65. <https://doi.org/10.1016/j.enbuild.2012.10.008>.
- [44] T. Gil-Lopez, C. Gimenez-Molina, Environmental, economic and energy analysis of double glazing with a circulating water chamber in residential buildings, *Appl Energy.* 101 (2013) 572–581. <https://doi.org/10.1016/j.apenergy.2012.06.055>.
- [45] M. Gutai, A.G. Kheybari, Energy consumption of water-filled glass (WFG) hybrid building envelope, *Energy Build.* 218 (2020) 110050. <https://doi.org/10.1016/j.enbuild.2020.110050>.
- [46] C. Li, Y. Lyu, C. Li, Z. Qiu, Energy performance of water flow window as solar collector and cooling terminal under adaptive control, *Sustain Cities Soc.* 59 (2020) 102152. <https://doi.org/10.1016/j.scs.2020.102152>.

- [47] C. Li, H. Tang, Evaluation on year-round performance of double-circulation water-flow window, *Renew Energy*. 150 (2020) 176–190. <https://doi.org/10.1016/j.renene.2019.12.153>.
- [48] C. Li, C. Li, Y. Lyu, Z. Qiu, Performance of double-circulation water-flow window system as solar collector and indoor heating terminal, *Build Simul*. 13 (2020) 575–584. <https://doi.org/10.1007/s12273-019-0600-y>.
- [49] C. Buratti, E. Belloni, F. Merli, M. Zinzi, Aerogel glazing systems for building applications: A review, *Energy Build*. 231 (2021) 110587. <https://doi.org/10.1016/j.enbuild.2020.110587>.
- [50] T. Gao, B.P. Jelle, T. Ihara, A. Gustavsen, Insulating glazing units with silica aerogel granules: The impact of particle size, *Appl Energy*. 128 (2014) 27–34. <https://doi.org/10.1016/j.apenergy.2014.04.037>.
- [51] F. Cotana, A.L. Pisello, E. Moretti, C. Buratti, Multipurpose characterization of glazing systems with silica aerogel: In-field experimental analysis of thermal-energy, lighting and acoustic performance, *Build Environ*. 81 (2014) 92–102. <https://doi.org/10.1016/j.buildenv.2014.06.014>.
- [52] R. Zeinelabdein, S. Omer, G. Gan, Critical review of latent heat storage systems for free cooling in buildings, *Renewable and Sustainable Energy Reviews*. 82 (2018) 2843–2868. <https://doi.org/10.1016/j.rser.2017.10.046>.
- [53] H. Akeiber, P. Nejat, M.Z.A. Majid, M.A. Wahid, F. Jomehzadeh, I. Zeynali Famileh, J.K. Calautit, B.R. Hughes, S.A. Zaki, A review on phase change material (PCM) for sustainable passive cooling in building envelopes, *Renewable and Sustainable Energy Reviews*. 60 (2016) 1470–1497. <https://doi.org/10.1016/j.rser.2016.03.036>.
- [54] D. Li, Y. Wu, B. Wang, C. Liu, M. Arıcı, Optical and thermal performance of glazing units containing PCM in buildings: A review, *Constr Build Mater*. 233 (2020) 117327. <https://doi.org/10.1016/j.conbuildmat.2019.117327>.
- [55] Z. Liu, Z. (Jerry) Yu, T. Yang, D. Qin, S. Li, G. Zhang, F. Haghghat, M.M. Joybari, A review on macro-encapsulated phase change material for building envelope applications, *Build Environ*. 144 (2018) 281–294. <https://doi.org/10.1016/j.buildenv.2018.08.030>.
- [56] L. Yang, J. nan Huang, F. Zhou, Thermophysical properties and applications of nano-enhanced PCMs: An update review, *Energy Convers Manag*. 214 (2020) 112876. <https://doi.org/10.1016/j.enconman.2020.112876>.
- [57] P. Sivasamy, S. Harikrishnan, S.I. Hussain, S. Kalaiselvam, L.G. Babu, Improved thermal characteristics of Ag nanoparticles dispersed myristic acid as composite for low temperature thermal energy storage, *Mater Res Express*. 6 (2019). <https://doi.org/10.1088/2053-1591/ab20ba>.
- [58] S. Harikrishnan, A. Devaraju, P. Sivasamy, S. Kalaiselvam, Experimental investigation of improved thermal Characteristics of SiO<sub>2</sub> /myristic acid nanofluid as phase change material (PCM), *Mater Today Proc*. 9 (2019) 397–409. <https://doi.org/10.1016/j.matpr.2019.02.169>.
- [59] L.M. Torres-martinez, *Handbook of Nanomaterials and Nanocomposites for Energy and Environmental Applications*, 2020. <https://doi.org/10.1007/978-3-030-11155-7>.



- [60] S. Li, G. Sun, K. Zou, X. Zhang, Experimental research on the dynamic thermal performance of a novel triple-pane building window filled with PCM, *Sustain Cities Soc.* 27 (2016) 15–22. <https://doi.org/10.1016/j.scs.2016.08.014>.
- [61] A. Wieprzkowicz, D. Heim, Thermal performance of PCM-glazing unit under moderate climatic conditions, 7th International Buildings Physics Conference, IBPC2018. (2018) 6.
- [62] D. Li, C. Zhang, Q. Li, C. Liu, M. Arıcı, Y. Wu, Thermal performance evaluation of glass window combining silica aerogels and phase change materials for cold climate of China, *Appl Therm Eng.* 165 (2020) 114547. <https://doi.org/10.1016/j.applthermaleng.2019.114547>.
- [63] J.S. Carlos, H. Corvacho, P.D. Silva, J.P. Castro-Gomes, Heat recovery versus solar collection in a ventilated double window, *Appl Therm Eng.* 37 (2012) 258–266. <https://doi.org/10.1016/j.applthermaleng.2011.11.027>.
- [64] J.S. Carlos, H. Corvacho, Ventilated Double Window for the Preheating of the Ventilation Air Comparison of Its Performance in a Northern and a Southern European Climate, *Journal of Renewable Energy.* 2013 (2013) 1–11. <https://doi.org/10.1155/2013/290865>.
- [65] J.S. Carlos, H. Corvacho, P.D. Silva, J.P. Castro-Gomes, Modelling and simulation of a ventilated double window, *Appl Therm Eng.* 31 (2011) 93–102. <https://doi.org/10.1016/j.applthermaleng.2010.08.021>.
- [66] S.A. Barakat, Thermal performance of a supply-air window, NRC Publications Archive Archives Des Publications Du CNRC. (1987).
- [67] M.C. Skaff, L. Gosselin, Summer performance of ventilated windows with absorbing or smart glazings, *Solar Energy.* 105 (2014) 2–13. <https://doi.org/10.1016/j.solener.2013.08.025>.
- [68] H. Choi, Y. An, K. Kang, S. Yoon, T. Kim, Cooling energy performance and thermal characteristics of a naturally ventilated slim double-skin window, *Appl Therm Eng.* 160 (2019) 114113. <https://doi.org/10.1016/j.applthermaleng.2019.114113>.
- [69] J. Wei, J. Zhao, Q. Chen, Energy performance of a dual airflow window under different climates, *Energy Build.* 42 (2010) 111–122. <https://doi.org/10.1016/j.enbuild.2009.07.018>.
- [70] J. Wei, J. Zhao, Q. Chen, Optimal design for a dual-airflow window for different climate regions in China, *Energy Build.* 42 (2010) 2200–2205. <https://doi.org/10.1016/j.enbuild.2010.07.016>.
- [71] V. Leal, E. Maldonado, The role of the PASLINK test cell in the modelling and integrated simulation of an innovative window, *Build Environ.* 43 (2008) 217–227. <https://doi.org/10.1016/j.buildenv.2006.10.025>.
- [72] T. Chow, Z. Lin, W. He, A.L.S. Chan, K.F. Fong, Use of ventilated solar screen window in warm climate, *Appl Therm Eng.* 26 (2006) 1910–1918. <https://doi.org/10.1016/j.applthermaleng.2006.01.026>.
- [73] T. Chow, Z. Lin, K. fai Fong, L. Chan, M. miao He, Thermal performance of natural airflow window in subtropical and temperate climate zones - A comparative study,

- Energy Convers Manag. 50 (2009) 1884–1890. <https://doi.org/10.1016/j.enconman.2009.04.028>.
- [74] T. Chow, Z. Qiu, C. Li, Potential application of “see-through” solar cells in ventilated glazing in Hong Kong, *Solar Energy Materials and Solar Cells*. 93 (2009) 230–238. <https://doi.org/10.1016/j.solmat.2008.10.002>.
- [75] W. Guo, L. Kong, T. Chow, C. Li, Q. Zhu, Z. Qiu, L. Li, Y. Wang, S.B. Riffat, Energy performance of photovoltaic (PV) windows under typical climates of China in terms of transmittance and orientation, *Energy*. 213 (2020) 118794. <https://doi.org/10.1016/j.energy.2020.118794>.
- [76] T. Chow, C. Li, Liquid-filled solar glazing design for buoyant water-flow, *Build Environ*. 60 (2013) 45–55. <https://doi.org/10.1016/j.buildenv.2012.11.010>.
- [77] T. Chow, C. Li, Z. Lin, Innovative solar windows for cooling-demand climate, *Solar Energy Materials and Solar Cells*. 94 (2010) 212–220. <https://doi.org/10.1016/j.solmat.2009.09.004>.
- [78] T. Chow, C. Li, Z. Lin, The function of solar absorbing window as water-heating device, *Build Environ*. 46 (2011) 955–960. <https://doi.org/10.1016/j.buildenv.2010.10.027>.
- [79] C. Li, T. Chow, Water-filled double reflective window and its year-round performance, *Procedia Environ Sci*. 11 (2011) 1039–1047. <https://doi.org/10.1016/j.proenv.2011.12.158>.
- [80] T. Chow, Y. Lyu, Effect of design configurations on water flow window performance, *Solar Energy*. 155 (2017) 354–362. <https://doi.org/10.1016/j.solener.2017.06.050>.
- [81] Y. Lyu, X. Wu, C. Li, H. Su, L. He, Numerical analysis on the effectiveness of warm water supply in water flow window for room heating, *Solar Energy*. 177 (2019) 347–354. <https://doi.org/10.1016/j.solener.2018.11.033>.
- [82] Y. Lyu, T. Chow, Evaluation of influence of header design on water flow characteristics in window cavity with CFD, *Energy Procedia*. 78 (2015) 97–102. <https://doi.org/10.1016/j.egypro.2015.11.121>.
- [83] C. Liu, Y. Lyu, C. Li, J. Li, K. Zhuo, H. Su, Thermal performance testing of triple-glazing water flow window in cooling operation, *Solar Energy*. 218 (2021) 108–116. <https://doi.org/10.1016/j.solener.2021.02.048>.
- [84] J. Stopper, M. Arch, F. Boeing, D. Gstoehl, Fluid Glass Façade Elements: Energy Balance of an Office Space with a Fluid Glass Façade, *Proceedings of the Conference Sb13 Munich-Implementing Sustainability-Barriers and Chances*. Munich. (2013). <https://mediatum.ub.tum.de/doc/1251323/file.pdf>.
- [85] J.M. Schultz, K.I. Jensen, F.H. Kristiansen, Super insulating aerogel glazing, *Solar Energy Materials and Solar Cells*. 89 (2005) 275–285. <https://doi.org/10.1016/j.solmat.2005.01.016>.
- [86] J.M. Schultz, K.I. Jensen, Evacuated aerogel glazings, *Vacuum*. 82 (2008) 723–729. <https://doi.org/10.1016/j.vacuum.2007.10.019>.
- [87] U. Berardi, The development of a monolithic aerogel glazed window for an energy retrofitting project, *Appl Energy*. 154 (2015) 603–615. <https://doi.org/10.1016/j.apenergy.2015.05.059>.

- [88] C. Buratti, E. Moretti, E. Belloni, M. Zinzi, Experimental and numerical energy assessment of a monolithic aerogel glazing unit for building applications, *Applied Sciences (Switzerland)*. 9 (2019). <https://doi.org/10.3390/app9245473>.
- [89] H. Wang, H. Wu, Y. Ding, J. Feng, S. Wang, Feasibility and optimization of aerogel glazing system for building energy efficiency in different climates, *International Journal of Low-Carbon Technologies*. 10 (2015) 412–419. <https://doi.org/10.1093/ijlct/ctu010>.
- [90] Y. Huang, J. lei Niu, Application of super-insulating translucent silica aerogel glazing system on commercial building envelope of humid subtropical climates - Impact on space cooling load, *Energy*. 83 (2015) 316–325. <https://doi.org/10.1016/j.energy.2015.02.027>.
- [91] C.K. Leung, L. Lu, Y. Liu, H.S. Cheng, J.H. Tse, Optical and thermal performance analysis of aerogel glazing technology in a commercial building of Hong Kong, *Energy and Built Environment*. 1 (2020) 215–223. <https://doi.org/10.1016/j.enbenv.2020.02.001>.
- [92] T. Gao, T. Ihara, S. Grynning, B.P. Jelle, A.G. Lien, Perspective of aerogel glazings in energy efficient buildings, *Build Environ*. 95 (2016) 405–413. <https://doi.org/10.1016/j.buildenv.2015.10.001>.
- [93] C. Buratti, E. Moretti, M. Zinzi, High energy-efficient windows with silica aerogel for building refurbishment: Experimental characterization and preliminary simulations in different climate conditions, *Buildings*. 7 (2017). <https://doi.org/10.3390/buildings7010008>.
- [94] Y. Chen, Y. Xiao, S. Zheng, Y. Liu, Y. Li, Dynamic heat transfer model and applicability evaluation of aerogel glazing system in various climates of China, *Energy*. 163 (2018) 1115–1124. <https://doi.org/10.1016/j.energy.2018.08.158>.
- [95] E. Belloni, C. Buratti, F. Merli, E. Moretti, T. Ihara, Energy & Buildings Thermal-energy and lighting performance of aerogel glazings with hollow silica : Field experimental study and dynamic simulations, *Energy Build*. 243 (2021) 110999. <https://doi.org/10.1016/j.enbuild.2021.110999>.
- [96] S. Li, K. Zhong, Y. Zhou, X. Zhang, Comparative study on the dynamic heat transfer characteristics of PCM-filled glass window and hollow glass window, *Energy Build*. 85 (2014) 483–492. <https://doi.org/10.1016/j.enbuild.2014.09.054>.
- [97] F. Goia, M. Perino, V. Serra, Experimental analysis of the energy performance of a full-scale PCM glazing prototype, *Solar Energy*. 100 (2014) 217–233. <https://doi.org/10.1016/j.solener.2013.12.002>.
- [98] F. Goia, M. Perino, V. Serra, Improving thermal comfort conditions by means of PCM glazing systems, *Energy Build*. 60 (2013) 442–452. <https://doi.org/10.1016/j.enbuild.2013.01.029>.
- [99] K. Zhong, S. Li, G. Sun, S. Li, X. Zhang, Simulation study on dynamic heat transfer performance of PCM-filled glass window with different thermophysical parameters of phase change material, *Energy Build*. 106 (2015) 87–95. <https://doi.org/10.1016/j.enbuild.2015.05.014>.
- [100] D. Li, Z. Li, Y. Zheng, C. Liu, A.K. Hussein, X. Liu, Thermal performance of a PCM-filled double-glazing unit with different thermophysical parameters of PCM, *Solar Energy*. 133 (2016) 207–220. <https://doi.org/10.1016/j.solener.2016.03.039>.

- [101] D. Li, T. Ma, C. Liu, Y. Zheng, Z. Wang, X. Liu, Thermal performance of a PCM-filled double glazing unit with different optical properties of phase change material, *Energy Build.* 119 (2016) 143–152. <https://doi.org/10.1016/j.enbuild.2016.03.036>.
- [102] C. Liu, Y. Wu, D. Li, Y. Zhou, Z. Wang, X. Liu, Effect of PCM thickness and melting temperature on thermal performance of double glazing units, *Journal of Building Engineering.* 11 (2017) 87–95. <https://doi.org/10.1016/j.jobbe.2017.04.005>.
- [103] H. Hua, X. Wang, Y. Liu, Y. Ma, G. Li, L. Bi, Comparative study on dynamic heat transfer characteristics of  $\text{CaCl}_2 \cdot 6\text{H}_2\text{O}$  and  $\text{Na}_2\text{SO}_4 \cdot 10\text{H}_2\text{O}$  used in PCM-filled glass window, *Sci Technol Built Environ.* 25 (2019) 905–913. <https://doi.org/10.1080/23744731.2019.1565552>.
- [104] A.M. Bolteya, M.A. Elsayad, A.M. Belal, Thermal efficiency of PCM filled double glazing units in Egypt, *Ain Shams Engineering Journal.* (2021). <https://doi.org/10.1016/j.asej.2020.12.004>.
- [105] D. Li, Y. Wu, C. Liu, G. Zhang, M. Arıcı, Energy investigation of glazed windows containing Nano-PCM in different seasons, *Energy Convers Manag.* 172 (2018) 119–128. <https://doi.org/10.1016/j.enconman.2018.07.015>.
- [106] D. Li, Y. Wu, C. Liu, G. Zhang, M. Arıcı, Numerical investigation of thermal and optical performance of window units filled with nanoparticle enhanced PCM, *Int J Heat Mass Transf.* 125 (2018) 1321–1332. <https://doi.org/10.1016/j.ijheatmasstransfer.2018.04.152>.
- [107] A. Wieprzkowicz, D. Heim, Modelling of thermal processes in a glazing structure with temperature dependent optical properties - An example of PCM-window, *Renew Energy.* 160 (2020) 653–662. <https://doi.org/10.1016/j.renene.2020.06.146>.
- [108] S. Zhang, W. Hu, D. Li, C. Zhang, M. Arıcı, Ç. Yıldız, X. Zhang, Y. Ma, Energy efficiency optimization of PCM and aerogel-filled multiple glazing windows, *Energy.* 222 (2021). <https://doi.org/10.1016/j.energy.2021.119916>.
- [109] Y. Huang, J.L. Niu, Energy and visual performance of the silica aerogel glazing system in commercial buildings of Hong Kong, *Constr Build Mater.* 94 (2015) 57–72. <https://doi.org/10.1016/j.conbuildmat.2015.06.053>.
- [110] M. Mcevoy, R.G. Southall, P.H. Baker, Test cell evaluation of supply air windows to characterise their optimum performance and its verification by the use of modelling techniques, *Energy Build.* 35 (2003) 1009–1020. [https://doi.org/10.1016/S0378-7788\(03\)00042-2](https://doi.org/10.1016/S0378-7788(03)00042-2).
- [111] D. Appelfeld, S. Svendsen, Experimental analysis of energy performance of a ventilated window for heat recovery under controlled conditions, *Energy Build.* 43 (2011) 3200–3207. <https://doi.org/10.1016/j.enbuild.2011.08.018>.
- [112] BSI, BS EN ISO 8990: 1996, Thermal Insulation–Determination of Steady-state Thermal Transmission Properties–Calibrated and Guarded Hot Box., (1996).
- [113] H.C. Frey, S.R. Patil, Identification and review of sensitivity analysis methods, *Risk Analysis.* 22 (2002) 553–578. <https://doi.org/10.1111/0272-4332.00039>.
- [114] P. Westermann, R. Evins, Surrogate modelling for sustainable building design—a review, *Energy Build.* 198 (2019) 170–186.
- [115] W.T. Ho, F.W. Yu, Chiller system optimization using k nearest neighbour regression, *J Clean Prod.* 303 (2021). <https://doi.org/10.1016/j.jclepro.2021.127050>.

- [116] D.K. Bhamare, P. Saikia, M.K. Rathod, D. Rakshit, J. Banerjee, A machine learning and deep learning based approach to predict the thermal performance of phase change material integrated building envelope, *Build Environ.* 199 (2021) 107927. <https://doi.org/10.1016/j.buildenv.2021.107927>.
- [117] H.P. Gavin, The Levenberg-Marquardt algorithm for nonlinear least squares curve-fitting problems, Department of Civil and Environmental Engineering, Duke University. 19 (2019).
- [118] S. Mirjalili, Genetic algorithm, in: *Evolutionary Algorithms and Neural Networks*, Springer, 2019: pp. 43–55.
- [119] R. Poli, J. Kennedy, T. Blackwell, Particle swarm optimization, *Swarm Intelligence.* 1 (2007) 33–57.
- [120] A. Shapiro, Monte Carlo sampling methods, *Handbooks in Operations Research and Management Science.* 10 (2003) 353–425.